Open Inverted Filters

Impact of fines content, coefficient of uniformity, and effective stress on inverted geometrically open granular filters in terms of parallel and perpendicular gradients

R.M. Besseling

Delft University of Technology

TU Delft

Open Inverted Filters

Impact of fines content, coefficient of uniformity, and effective stress on inverted geometrically open granular filters in terms of parallel and perpendicular gradients

by

R.M. Besseling

Delft University of Technology
Faculty of Civil Engineering and Geosciences

Student number: 4692551
Project duration: February 13, 2023 - December 8, 2023

Thesis committee:

Dr. ir. B. Hofland	TU Delft
Dr. ir. A. Antonini	TU Delft
Ir. D.C.P. van Kester	Van Oord, TU Delft
Ir. H.G. Lavies	Van Oord

Cover: Construction of a new container terminal in Moín, Costa Rica by Van Oord

TU Delft Van Oord TKI Deltatechnologie

Preface

Being born and raised in a village below sea level (NAP) aroused my attention for Hydraulic Engineering. I think the ingenious and ancient Dutch mechanisms to reclaim land are truly fascinating. Furthermore, I find artificial island construction very interesting and one day I would love to build an island myself. This is why I am more than happy that I could do my Master thesis on Coastal Engineering. By doing this research I found out a little more about this extensive field. In addition to the interesting subject of the research, I found it very instructive to work in various laboratories of Delft University of Technology.

I am very grateful for the support I received from several people who made it possible for me to complete my Master of Science in Civil Engineering at Delft University of Technology. There are a few people I would like to mention in particular. First of all, I would like to thank my thesis committee. Dr. Ir. Bas Hofland and Dr. Ir. Alessandro Antonini, thank you for your enthusiastic ideas and helpful suggestions. The theoretical discussions and sharp remarks really helped me to clearly present this academic research. Ir. Dennis van Kester and Ir. Hugo Lavies, thank you for your support and great guidance during our weekly meetings. The passionate stories about Coastal Engineering in practice from you and your colleagues at Van Oord made me eager to work in this field.

Furthermore, I am grateful for all the help I received from the employees of the Hydraulic Engineering Laboratory, Construction Laboratory, and Laboratory of Geoscience and Engineering of Delft University of Technology. Finally, I would like to thank my friends and family for their great support during this process.

R.M. Besseling
Delft, December 2023

Summary

This study investigates the capacity of an open inverted filter to stabilize the interface between the base fill and core fill in a rubble mound structure; see Figure 1. Today, a geotextile is used as a filter, meaning difficult and expensive placement and an increased amount of plastic in the environment. No filter at all leads to erosion of the base material, which can cause ground level settle, maintenance works and damaged structures on top of the land reclamation. The forces on the open inverted filter arise from porous flow and its quantification involves both parallel and perpendicular hydraulic gradients. It is of interest at which level and under which conditions the hydraulic gradients are insufficient to cause a significant loss of base fill through the rubble mound.

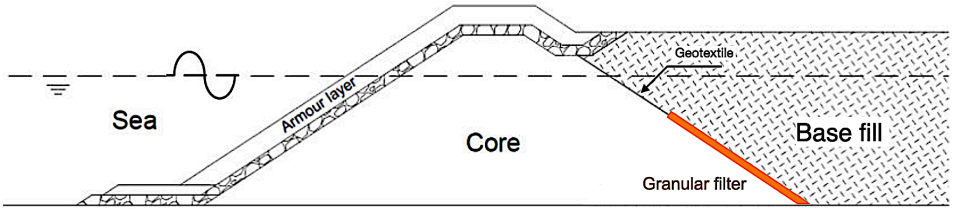

Figure 1: Example of a base fill retaining rubble mound structure including a granular filter.

The research is part of a research line. In the previous four MSc theses it was found that an open inverted filter could be stable. The critical gradients turned out to be inversely proportional to the Stability Ratio, where a Stability Ratio of 8 showed promising results and is therefore applied in the current research. The coefficient of uniformity was always smaller than common for dredged sand (C_u < 2.1), therefore a higher coefficient of uniformity is applied in this research (C_u = 2.9). Another very important characteristic of the base material, which is the fines content, was also not researched before. Furthermore, hydraulic gradients in a base fill-retaining rubble mound structure were estimated by an OpenFOAM model and the measured critical perpendicular gradients clearly showed an unstable system in the previous theses. It turned out that no parallel configuration tests were performed yet without leakage of the physical model, so this is another topic for the current research.

A two-dimensional numerical model of the physical model showed a four times higher perpendicular gradient during the combined flow configuration than measured, and these results had therefore been adjusted. This numerical model had not been verified yet by measurements, hence a grid of pressure sensors over the length of the filter is applied in the current research. Initial sand saturation of the filter layer, as well as more angular base material, were found to lower the critical gradients. Furthermore, a positive relationship between surcharge and the critical perpendicular gradient had already been observed. However, the quantified relationship was also based on lower limits of the critical perpendicular gradients and no relationship between surcharge and critical parallel gradient had been found yet. Hence, more surcharge tests are performed, for all flow configurations, within the current research.

The research question of the current study is: *How do the fines content and coefficient of uniformity of the base material, and effective stress, influence the applicability of an inverted geometrically open granular filter at the interface of a land reclamation and a rubble mound structure in terms of both parallel and perpendicular hydraulic gradients?*

A full-scale physical model, with a 760 mm long open inverted filter, is employed to determine the critical hydraulic gradients required to initiate erosion. The model consists of three compartments, with the central compartment containing the open inverted filter, as illustrated in Figure 2 for the base case situation of combined flow. The two side compartments are filled with water, and one of them features a plunger mechanism to induce flow. When the top of compartment B is sealed watertight, the parallel flow direction is maximized and the perpendicular flow direction is minimized, while closing compartment C from compartment B creates a perpendicular flow configuration.

A one-dimensional and two-dimensional numerical model are developed to gain insights into the flows within the physical model. In the physical model, pressure sensors and water level gauges are used to determine the hydraulic gradients. A pressure sensor grid gives insight into the development of hydraulic gradients within the base filter system. The middle pressure sensors in the base material and the two rightmost pressure sensors in the filter material match best with the hydraulic gradients based on the water level gauges and numerical models. Therefore, these pressure sensors are the normative pressure sensors for, respectively, the perpendicular and parallel hydraulic gradients.

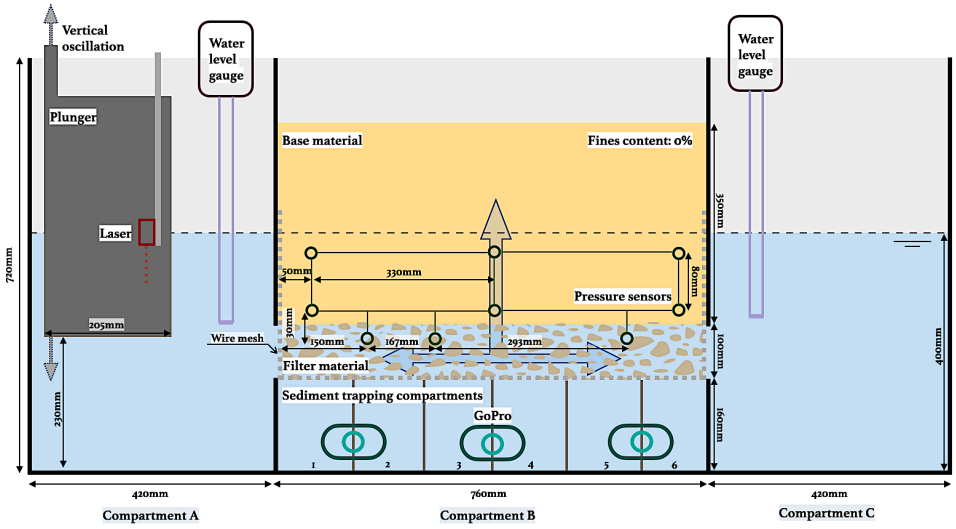

Figure 2: Setup of the physical model in the base case situation of the combined flow configuration.

The critical hydraulic gradient is based on initial erosion, which is defined as: The first moment of a noticeable difference in the time-lapse images of the central sediment trapping compartments. The following results and conclusions can be made based on the current research:

- The critical hydraulic gradient did not necessarily imply erosion at every higher gradient. This indicates that the base-filter interface can **reform to a more stable configuration** that can withstand higher gradients. Therefore, designing only for the single largest hydraulic gradient is not imperative.
- It is of interest which hydraulic gradient (parallel or perpendicular) is leading during **combined flow** in the physical model, due to the different erosion mechanisms. Therefore, the critical hydraulic gradients of the different flow configurations are compared. Parallel gradients up to 0.07 are measured and the parallel flow direction showed to be critical for combined flow for the conditioned tested in this research. A relation between the critical perpendicular gradients during combined flow showed to be less clear for the conditioned tested in this research.
- The **fines content** is one of the most important characteristics of dredged sand. To investigate the impact of fines on the stability of the filter, 5% and 10% fines have been added to the base material. The critical parallel hydraulic gradient increases for a higher fines content, which can be explained by the lower hydraulic conductivity. A lower flow velocity occurs for the same hydraulic gradient in this case. This reduces the drag force on the sand particles and exceeds the threshold shear stress for sediments. The critical perpendicular gradient is increased as well, also due to the difference in hydraulic conductivity and not by an increase in strength of the base material to resist external eroding forces.
- The **coefficient of uniformity** (C_u) is usually greater than 2.0 for land reclamation projects. Therefore, a sand combination with C_u=2.9 was created for the current research, compared to more narrow graded sand (C_u around 1.6) from previous research. The critical parallel hydraulic gradients are comparable, while the perpendicular hydraulic gradients are slightly lower. The greater variation in grain sizes could disturb the formation of arches, and the smaller sand fractions could be less stable and easier migrated.

- The larger the layer of base material above the granular filter in a rubble mound structure, the larger the **effective stresses** at the base-filter interface. Superimposed loads of 100 and 200 kPa have been applied to model this surcharge. Both the critical parallel and critical perpendicular gradients show a positive relationship with the effective stress. An increase of 60% of the critical perpendicular gradient is observed for a superimposed load of 100 kPa. For larger superimposed loads, a smaller increase is expected; 80% increase in critical perpendicular gradient for 200 kPa compared to 0 kPa. The arching mechanism is enhanced by effective stresses which is beneficial against perpendicular and parallel loading.
- A side effect of increased effective stresses is compaction. Compaction can also lead to increased critical hydraulic gradients.
- During this research, based on a Stability Ratio of 8.0, only incidental erosion was observed, so no transport erosion. The maximum parallel hydraulic gradient measured is 0.07 and the maximum perpendicular hydraulic gradient is 0.28.
- The critical hydraulic gradients compared to the results of the OpenFOAM model of a base fill-retaining rubble mound structure showed a stable filter system based on the parallel gradients and an unstable filter system based on the perpendicular gradients.

Table of Contents

List of symbols

Symbol	Definition	Unit
a	Width of the piles in trapdoor system	m
A	Area cylinder permeability test	m^2
A_p	Amplitude plunger numerical model	m
C	Constant Kozeny-Carman formula (for shape and tortuosity)	$-$
C_c	Coefficient of gradation	$-$
C_u	Coefficient of uniformity	$-$
d_{n50}	Median nominal diameter	m
d_x	Grain diameter where x% of the grain mass has a smaller diameter	m
e	Void ratio	$-$
E	Non-Darcy effect	$-$
F_s	Shape factor (nominal) median diameter	$-$
F_0	Forchheimer number	$-$
g	Acceleration of gravity	m/s^2
H	Fill height in trapdoor system	m
H	Total head	m
H_s	Significant wave height	m
I_{cr}	Critical hydraulic gradient in the filter	$-$
$I_{\parallel}$	Parallel hydraulic gradient	$-$
$I_{\perp,A}$	Perpendicular hydraulic gradient between compartments A and B	$-$
$I_{\perp,C}$	Perpendicular hydraulic gradient between compartments B and C	$-$
I	Hydraulic gradient	$-$
k	Wave number	m^{-1}
k	Intrinsic permeability	m^2
k_0	Kozeny-Carman constant	$-$
K	Hydraulic conductivity	m/s
KC	Keulegan-Carpenter number	$-$
K_0	Coefficient of at-rest lateral earth pressure	$-$
L	Length	m
n	Porosity of soil	$-$
p	Pressure	N/m^2
q	Specific discharge	m^2/s
Re	Reynolds number	$-$
$Re_{d_{50}}$	Grain Reynolds number	$-$
s	Spacing between the piles in trapdoor system	m
S	Specific surface of solids in Kozeny-Carman formula	m^{-1}
t	Time	s
t_w	Waiting time plunger numerical model	s
T	Wave period	s
T_p	Peak wave period	s
u	Filter velocity	m/s
u_{*c}	Critical shear velocity (Shields)	m/s
$\hat{U}$	Amplitude of flow velocity oscillation	m/s
V	Volume	m^3
W_{50}	Median weight	N
x_i	Inflection point	m
$z_{p,0}$	Initial height plunger numerical model	m

Symbol	Definition	Unit
β	Non-Darcy or inertial coefficient	$-$
β	Slope angle of base fill surface	$^\circ$
γ_w	Volumetric weight ($\rho_w g$)	N/m^3
Δx	Distance	m
Δz	Vertical distance between tubes permeability test	m
μ	Dynamic viscosity	$kg/m/s$
ν	Kinematic viscosity	m^2/s
ρ_s	Density of sediment	kg/m^3
ρ_w	Density of water	kg/m^3
σ	Effective soil pressure	kPa
ϕ	Effective friction angle soil	$^\circ$
ω	Coefficient quadratic friction term Forchheimer	s^2/m^2

1 Introduction

Half of the world's population, 3.7 billion people, currently resides in cities. This number is expected to double by 2050, creating challenges related to food, water, energy consumption and space. The growing demand for space is combined with mass migration to coastal areas. This is not surprising, because the intersection of land and water has always been an attractive place to live, work, and recreate. It offers a wide range of opportunities for trade routes, industry, and tourism.

15 out of 23 megacities worldwide are located on the coast and recent estimates suggest that in more than half of the world's coastal countries, at least 80% of the national population currently lives within 100 km of the coastline (Blackburn et al., 2019). Within many of these coastal megacities there is a shortage of land area, which explains the need for land reclamations. Ambitious examples of land reclamations are the Palm Jumeirah in Dubai, the construction of a new container terminal in Costa Rica, and the enlargement of islands in the Maldives, see Figure 1.1.

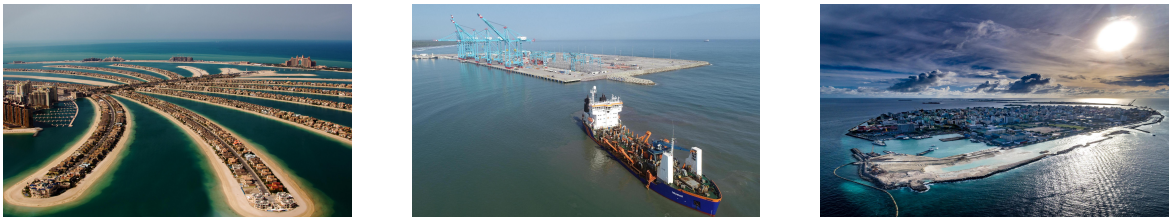

(a) Palm Jumeirah, Dubai **(b)** Container terminal, Costa Rica **(c)** Island enlargements, Maldives

Figure 1.1: Examples of land reclamations by Van Oord.

1.1. Problem description

The design of a land reclamation is extremely important. The structure should be strong enough to withstand the forces exerted by waves, which can erode the base fill. The type of land reclamation on which this research focuses is a base fill protected against the sea by a rubble mound structure; see Figure 1.2.

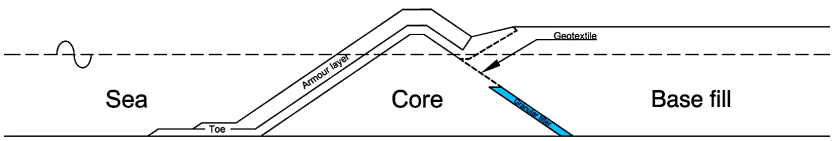

Figure 1.2: Schematic overview of a rubble mound structure with in blue the open granular filter (Boersma, 2020).

The base fill consists of dredged sand, because sand is a widely available material that compacts easily. The core of the rubble mound structure consists of quarry run, which forms an unstable interface with the base fill due to its relative particle sizes (Polidoro et al., 2015). If the base fill erodes, the ground level will settle, which leads to many maintenance works and damaged structures on top of the land reclamation.

That is why the interface between the rubble mound structure and base fill is usually ”lined” by a geotextile. The disadvantages of using geotextile are its difficult and thus expensive placement and the increased amount of plastic in the environment. In this research, the possibilities for using a granular open filter are further investigated. It is of interest at which level and under which conditions the wave-induced hydraulic gradients are insufficient to cause a significant loss of the base fill through the rubble mound structure. These outward gradients could come from the draw-down phase of wave action, tidal driven water levels, or storm-setup drainage (Polidoro et al., 2015).

Open filters have been researched before, but mainly in a situation where a sandy bed layer is protected with larger gravel on top. Previous research focused on steady flow or wave attack on this *standard* open filter system. In the current research line, there are some significant differences to the open filter situation compared to previous research:

- The base fill is on top of the open filter, this results in an open *inverted* filter.
- The open filter is placed between two large soil layers: the base fill and the rubble mound structure core.
- The large base fill on top of the open filter induces a surcharge on the filter.
- The hydrodynamic loads change as a result of this different orientation of the open filter.
- The filter follows the inclination of the rear end of the rubble mound structure.

1.2. Research line

Multiple students have already analyzed the interface between the rubble mound core and the base fill. This section gives a short overview of these previous MSc theses at Delft University of Technology. This research will be continued and expanded, and the latest physical setup will be used in the current research.

Nolthenius (2018) designed a physical model to gain insight into the behavior of sediments at the base-filter interface of a base fill retaining rubble mound structure, both during the placement of the base fill and during hydraulic loading. A scaled representation ($\lambda \approx 15$) of the breakwater of Polidoro et al. (2015) was used. It was concluded that for a slope of approximately 35° between the core of the rubble mound structure and the base fill, the initial interface is stable and the critical hydraulic gradient was 0.04. The results suggest that the critical loading conditions at the interface are comparable to conventional filter criteria and are higher than the measured gradients of Vanneste and Troch (2012) and Polidoro et al. (2015). An overview of their research is given in the literature study, section 2.1. Another conclusion from the research of Nolthenius (2018) is that during wet installation the sediments penetrate further into the core than during dry installation. The removal of the geotextile turned out to lead to an unstable sand-stone interface, but replacement with an open filter system could be possible.

Van de Ven (2019) used a numerical model (OpenFOAM) and a physical model to estimate the pressures around and inside the open filter layer. On the basis of the numerical model, the largest parallel gradients were 0.02 at the top of the filter layer and decreased to zero, while the perpendicular gradients were 0.6 at the top and decreased to 0.2-0.3. The critical gradients have been determined for the parallel and perpendicular flow configuration, for D_{15F}/D_{85B} ratios of 7.5, 8.0, and 9.5. No critical gradient was found for the ratios 16.5 and 4.0 due to limitations of the model setup.

The third research in the research line comes from Boersma (2020) who considered a geometrically open granular filter, with the physical test setup of Van de Ven (2019). Parallel and combined loading conditions were investigated, as well as the influence of the Stability Ratio and the characteristic grain size of the base material. Boersma (2020) also introduced tests with initial sand saturation of the filter layer, which resulted in a reduction of the critical gradient of at least 73%. Further research is advised, because it could also be possible that the sand that was initially present in the filter was just washed out. Furthermore, during this research, a new physical model was designed and constructed.

In the next research, Lengkeek (2022) has used the newly developed experimental setup of Boersma (2020) to test the influence of a surcharge, Stability Ratios and angularity of the base material. Perpendicular, parallel and combined configurations were tested; however, due to leakage of the top seal, the critical parallel gradient could not be determined. According to the numerical model, the perpendicular

gradient during the combined configuration was four times larger near the plunger compared to the center of the filter, but this has not been verified yet. Other findings were a negative correlation between the Stability Ratio and the critical gradients and an effective stress of 150 kPa doubles the critical perpendicular gradient (linear rise). Special attention was given to the angularity of the material, where the more angular material seemed to have a lower critical gradient. Points of discussion were the varying distances between the pressure sensors, the sloshing of the water when testing at high gradients, and problems with airtightness.

1.3. Problem analysis

Even though the research line gave interesting results, there are still many unknown aspects about the open inverted filter. The following aspects can be investigated to reduce the knowledge gap:

- The parallel configuration has not been analyzed yet without leakage of the top seal.
- The influence of a surcharge on the critical parallel gradient is unknown.
- The distribution of the perpendicular hydraulic gradient over the width of the filter within the physical model has not been measured.
- Measurements of critical perpendicular hydraulic gradients of the open filter are lacking when a surcharge of more than 100 kPa is applied.
- There is limited understanding of the influence of the inclination of the open inverted filter on the critical hydraulic gradients.
- More information on critical hydraulic gradients at Stability Ratios smaller than 10.5 is desired.
- A better understanding of the influence of the fines content or the hydraulic conductivity of the base fill on the critical hydraulic gradients is desired.
- Wider graded sediment resembles dredged sand. The influence of a wider graded base material has not yet been investigated.
- The influence of base fill compaction on critical hydraulic gradients when a surcharge is applied is unknown.
- The effect of dry or wet placement of the base fill on critical hydraulic gradients has not been directly compared.
- A better understanding of the stability after initial erosion has occurred is lacking.

1.4. Objective and research questions

This research further investigates the possibilities of applying an inverted geometrically open granular filter in a rubble mound land reclamation. This objective must be achieved using a physical test setup and a numerical model. To answer the research question, various subquestions are formulated. When all the subquestions are answered, the research question can be answered.

Research question

How do the fines content and coefficient of uniformity of the base material, and effective stress, influence the applicability of an inverted geometrically open granular filter at the interface of a land reclamation and a rubble mound structure in terms of both parallel and perpendicular hydraulic gradients?

Sub-questions

- Is the base-filter interface still stable after the critical hydraulic gradient has been reached?
- What is the dominant direction (parallel or perpendicular) of the critical hydraulic gradients within the combined flow configuration?
- What is the influence of the fines content in the base fill on the critical hydraulic gradients?
- What is the influence of the coefficient of uniformity of the base fill on the critical hydraulic gradients?
- What is the influence of effective stress at the base-filter interface on the critical hydraulic gradients?

Methodology
A full-scale physical model is used to determine the critical hydraulic gradients required to initiate erosion. The model consists of three compartments, of which the central compartment contains the open inverted filter. When the top of compartment B is sealed watertight, the parallel flow direction is maximized and the perpendicular flow direction is minimized, while closing compartment C from compartment B creates a perpendicular flow configuration. When these two flow configurations are compared with a combined flow configuration, the dominant direction of the critical hydraulic gradients can be determined for the combined flow.

To complement the previous studies from the research line, smaller Stability Ratios than 10.5 and higher superimposed loads than 100 kPa can be tested with a more powerful plunger-system. To make this research more applicable to reality, a wider graded base material is tested, with fines contents comparable to dredged sediments. Furthermore, it is interesting (and economical) to know if the base fill is still stable after the initial critical hydraulic gradient has been reached. Pressure sensors and water level gauges are used to determine the hydraulic gradients in the physical model. A pressure sensor grid gives insight into the development of hydraulic gradients within the base-filter system. In addition to the physical model, a one-dimensional and two-dimensional numerical model are developed to gain insight into the flow dynamics within the system.

1.5. Hypotheses

- The base-filter interface is predicted to still be stable after initial erosion has occurred due to reformation of the sand arches in the filter material. Base material particles can find a new, more favorable position when moving down the filter, and then stop moving.
- The dominant direction for the critical hydraulic gradient during the combined flow configuration is expected to be the perpendicular hydraulic gradient. This is based on previous results in the research line, where the critical hydraulic gradients seem to be based on the arching mechanism, which is mainly influenced by the perpendicular hydraulic gradients. However, parallel flow configuration results without leakage were not obtained.
- Higher critical hydraulic gradients are expected when fines are added, because the finer sediments can cling together by means of cohesive bonds or due to negative pore pressures, which mitigates erosion. Furthermore, fines can act as a protective layer that protects the larger sand grains, reducing their exposure to erosive forces. A fines content lowers porosity and hydraulic conductivity and could form an impermeable layer, which would increase perpendicular hydraulic gradients.
- Lower critical hydraulic gradients are expected for relatively wider graded sand, because it is possible that finer sand fractions are not internally stable and are lost more easily through the filter material.
- Higher critical perpendicular hydraulic gradients are expected when the effective stress at the base-filter interface is increased, because these effective stresses will enhance the strength of the sand arches. The influence on the critical parallel hydraulic gradient is expected to be minimal, because this gradient depends mainly on the shear stress.

1.6. Outline report

This report is subdivided into 8 different chapters of which this Introduction is the first. Chapter 2, *Literature study on granular filters*, provides background information on hydraulic loads and gradients, granular material and inverted geometrically open granular filters, which correspond to the sub-questions. Chapter 3, *Numerical model*, explains the numerical model that is used to predict the flows and hydraulic gradients in the physical model. The next chapter, *Physical model*, shows the methodology of the physical tests and the adjustments made to the setup compared to previous research. Chapter 5, *Results: Analysis of hydraulic gradients*, shows the results obtained with the various tests that are performed with the physical model compared to the numerical model. Chapter 6, *Results: Critical hydraulic gradients*, show the determination of critical hydraulic gradients, also compared to previous research. The next chapter *Discussion*, provides a discussion on this whole research based on its reliability and shows improvements. The last chapter, *Conclusions and Recommendations*, concludes this research by answering the main question and provides recommendations for further research.

2

Literature study on granular filters

The literature study consists of theoretical background and previously performed studies regarding open granular filters. First, the hydraulic loads that work on a base fill retaining rubble mound structure are explained in section 2.1. In section 2.2 the hydraulic gradients are explained. The different properties of the granular material are clarified in section 2.3. In the next sections, section 2.4 and section 2.5, the filters and especially the inverted geometrically open granular filters are explained. Finally, a summary of the literature study is given in section 2.6.

2.1. Hydraulic loads

A dredged land reclamation is a structure built of sand, gravel, and rock, located in open water. Therefore, this structure will be influenced by hydraulic loads, which can cause erosion when the forces on a grain are off balance (Izbash approach) or when the friction force of the water flow exceeds a critical value (Shields approach) (Schiereck & Verhagen, 2019). Hydraulic loads from wave pressures can cause this erosion as well as from hydraulic head differences, wave- and wind-induced setup, tides, precipitation, or wave-induced pore pressure build-up at the leeside of the rubble mound structure. This implies that hydraulic loads depend on the wave climate at the rubble mound structure.

2.1.1. Rubble mound structure with an open rear side

For the construction of a land reclamation protected by a rubble mound structure, the relationship between the force on the rubble mound structure (H_s and T_p) and the critical gradients of the open filter layer must be determined. Creating a numerical model is very time consuming, but the empirical model of Vanneste and Troch (2012) could be useful. Vanneste and Troch (2012) investigated the case of a rubble mound structure with an open rear side, to determine the spatial variation of pore pressure heights within the rubble mound structure core. This evolution of the pore pressure along a horizontal section is calculated with the gradients at each location. At the interface between the core and filter layer, reference pressures occur from the waves, which is influenced by: wave run-up and the hydraulic resistance of the armor and filter layer. The wave run-up depends on the spatial variation of the pressure height along the armor slope, and the hydraulic resistance causes a difference between pressure heights on the slope. In the research of Vanneste and Troch (2012) it appears impossible to describe the variation of reference pressures due to the influence of hydraulic resistance by means of specific material properties. It is notable that the effect of wave height becomes most pronounced closer to the sea water level (SWL).

The pressure heights in the rubble mound structure according to Vanneste and Troch (2012) are shown in Figure 2.1. Zone 1 identifies the region with a positive rate of gradient change, and zone 2 identifies a negative rate of gradient change. The point where dI/dx = 0 is the inflection point identified by x_i. The slope of the rubble mound structure affects the decay of the pressure height in zone 1, therefore it is not exponential. The hydraulic gradient in zone 1 increases with increasing wave period.

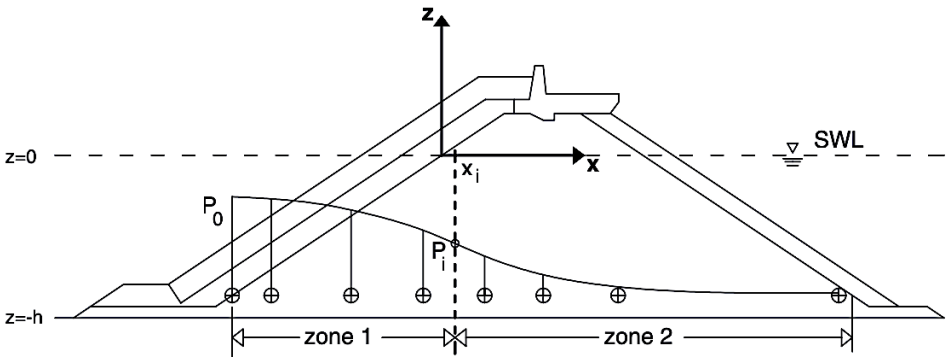

Figure 2.1: Pressure heights rubble mound structure core according to Vanneste and Troch (2012).

In zone 2 the pore pressure height is in good correspondence with the exponential decay. The damping rate of the pressure in zone 2 increases closer to sea water level (SWL), increases with increasing wave length, and increases with increasing wave height. The effect of wave length is much more pronounced than the wave height, and the effect of wave height is more pronounced for regular waves compared to irregular waves. Vanneste and Troch (2012) found that the damping rate of the pressure attenuation is dependent on the vertical position.

The case of a closed rear rubble mound structure has been investigated by Polidoro et al. (2015), as described in subsection 2.1.2. The total pressure amplitude on the rear side for a rubble mound structure with a closed rear side will be the sum of the incoming and reflected wave height. This is comparable to twice the transmitted wave height through a rubble mound structure with an open rear.

Irregular gradients
There are usually wind forces at sea that create an irregular wave climate, so the gradients are also irregular. For a Jonswap spectrum, which is representative for storm waves, the maximum wave height is about twice the significant wave height. Significant wave height is an important measure of absolute erosion length in a sand core rubble mound structure (Ockeloen, 2007). Research of Ockeloen (2007) showed that irregular wave loading produced results similar to regular wave loading for the peak period. However, this irregular wave pattern might decrease the critical gradient compared to a regular wave pattern when the largest gradients cause the arches to break.

Long waves and currents
Longer waves could protrude further into the rubble mound structure and therefore have a greater influence on the gradients. A very long wave can be seen as a current, which can have a negative effect on arching, see subsection 2.4.7. Even though it is highly uncertain, it could decrease stability under a longer duration.

Oblique wave attack creates long shore currents, which have a longer infiltration length through the core of the rubble mound structure than perpendicular and parallel currents. This means that the pressures and so the gradients from obliquely incident waves are lower on the rear side of the rubble mound structure. It will not have an influence on the perpendicular waves, but it will create another parallel gradient in another direction than the experimental setup. The reflection of perpendicular waves is maximal (Dalrymple et al., 1991).

2.1.2. Land reclamation protected by a rubble mound structure

In recent years, many sand-fill islands with a base fill retaining rubble mound structure have been constructed. Most of the time, a geotextile is placed to protect the main base fill from being drained through the rubble mound structure. As has been described in the research line of section 1.2, experiments have been conducted to determine whether this geotextile is actually required to prevent erosion. According to Nolthenius (2018), only removing the geotextile will cause suffusion, but subsequent research showed that an open filter system could work under certain conditions.

Polidoro et al. (2015) has researched base fill retaining rubble mound structures with an abbreviated geotextile at the downward extent. A physical model has been used to measure the pore pressure and,

hence, the local hydraulic gradients in the core, as can be seen in Figure 2.2. It was concluded that the hydraulic gradient did not exceed 0.03 within the core for 98% of the peaks at the downward extend of the geotextile. Since the perpendicular gradient is larger in the base fill, this needs to be measured as well to design an open filter.

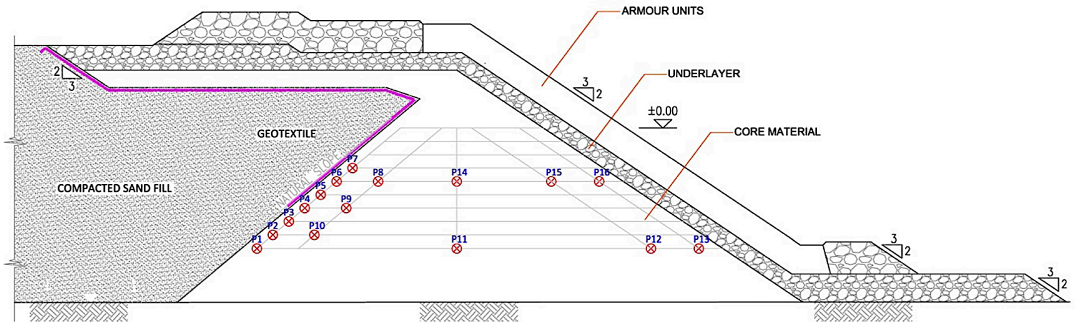

Figure 2.2: Cross-section setup base fill retaining rubble mound structures with an abbreviated geotextile at the downward extent (Polidoro et al., 2015).

In the thesis of Van de Ven (2019) the highest 2% gradients in the base fill have been estimated with a numerical model in OpenFOAM. Cyclic loading was considered and parallel and perpendicular critical gradients were determined. This means that the hydraulic loading on the land reclamation caused by heavy rainfall or storm surge setup is not included. Boersma (2020) executed combined tests for specific Stability Ratios, and both results are shown in Figure 2.3.

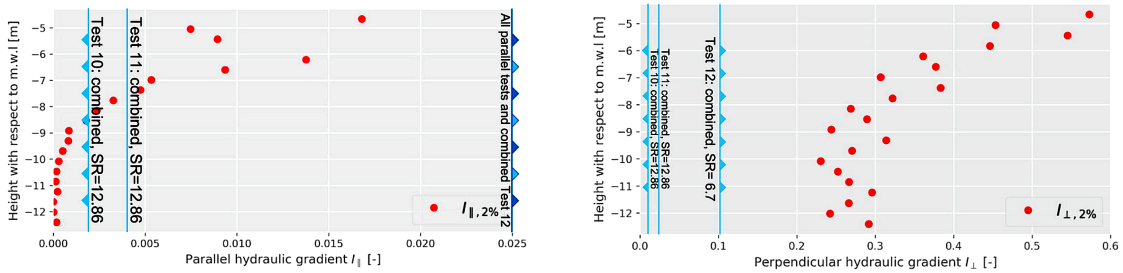

(a) Parallel hydraulic gradient

(b) Perpendicular hydraulic gradient

Figure 2.3: Parallel and perpendicular component of the critical gradient of the combined tests in blue (Boersma, 2020) with the gradients estimated with OpenFOAM in red (Van de Ven, 2019).

2.2. Hydraulic gradients

The hydraulic loads explained in subsection 2.1.2 induce a hydraulic pressure difference (Δp) over a certain distance (Δx), also known as a hydraulic gradient (I). The gradient can also be seen as a relation between load and strength, where the head difference is the load, and the length can be interpreted as the strength.

$$\rho_w g I = \frac{\Delta p}{\Delta x} \quad I = \frac{\Delta H}{L} \tag{2.1}$$

2.2.1. Hydraulic conductivity

The hydraulic conductivity (K (m/s)) of a soil refers to the ability of a porous material, such as sand or gravel, to allow fluids to pass through it. Hydraulic conductivity depends on several factors, including intrinsic permeability (k (m^2)), size, shape and compaction of the grains and the nature of the fluid. A frequently quoted relationship for hydraulic conductivity is the Kozeny-Carman formula (Carman, 1939), see Equation 2.2. The specific surface of solids S requires permeameter tests. In Equation 2.3 a formula with intrinsic permeability as input to hydraulic conductivity is given.

$$K = \frac{1}{k_0} \frac{\rho_w g}{\mu} \frac{e^3}{1+e} \frac{1}{{S_v}^2} \tag{2.2}$$

$$K = \frac{k \gamma_w}{\mu} \tag{2.3}$$

Figure 2.4 shows a sketch of a constant head permeability test (TU Delft, 2020). The hydraulic conductivity can be calculated with Darcy's law, see Equation 2.4.

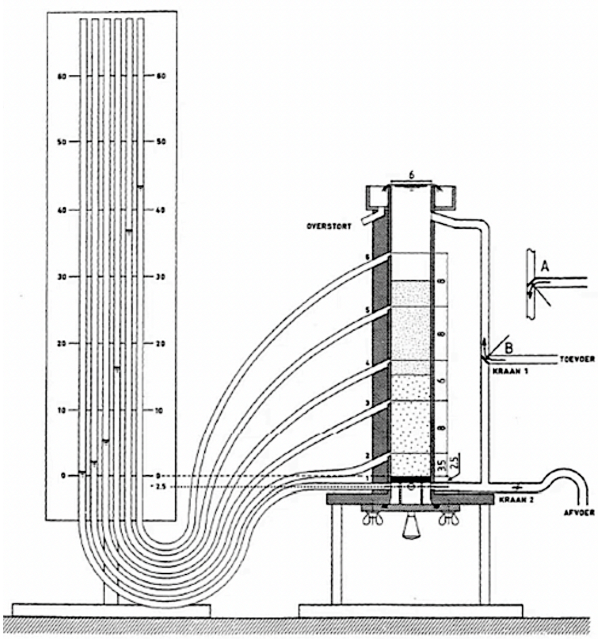

Figure 2.4: Permeability test with constant head (TU Delft, 2020).

$$\frac{Q}{A} = -K * \frac{\Delta H}{\Delta z} \tag{2.4}$$

2.2.2. Intrinsic permeability

The intrinsic permeability (k) depends on the geometry of the grain skeleton, such as porosity, the shape of the particles, and the squared grain size (Verruijt, 2017). According to Chapuis and Aubertin (2003), to precisely determine the intrinsic permeability, an improved permeability test should be used to ensure full saturation with both vacuum and de-aired water. In addition, soil gradation should not be prone to internal erosion.

Much research on this topic has been conducted leading to many empirical formulas for predicting intrinsic permeability. Dolzyk and Chmielewska (2014) used these empirical formulas to predict the coefficient of permeability of non-plastic soils and compared this to laboratory tests for soils with different porosity (n). According to Dolzyk and Chmielewska (2014) the best correlation was obtained using the formula of Shahabi et al. (1984), see Equation 2.5. The empirical formula of Shahabi et al. (1984) is only applicable for sands ($0.15 \leq d_{10} \leq 0.59$ mm) with a coefficient of uniformity ranging from 1.2 to 8. Note that d_{10} is given in mm and K in cm/s.

$$K = 1.2 C_u^{0.735} d_{10}^{0.89} \frac{e^3}{(1-e)^2} \tag{2.5}$$

Another commonly used equation for the permeability of sand has been formulated by Chapuis and Aubertin (2003), see Equation 2.6 (Pap & Mahler, 2021). According to Schulz et al. (2019), several

experimental studies of the impact of grain size on permeability showed that the use of d_{10} is a good choice (compared to, for example, d_{17}, d_{20}, and d_{50}).

$$k = 2.4622[d_{10}^2 \cdot \frac{e^3}{1+e}]^{0.7825} \tag{2.6}$$

The prediction of Slichter (1897) works well for grains with 0.01 < d_{10} < 5 mm and $0.23 < n < 0.5$. The formula of Slichter (1897), Equation 2.7, is in accordance with the Rock Manual (CIRIA; CUR; CETMEF, 2007), see Figure 2.5.

$$K = \frac{\rho g}{\mu} 0.01 n^{3.287} d_{10}^2 \tag{2.7}$$

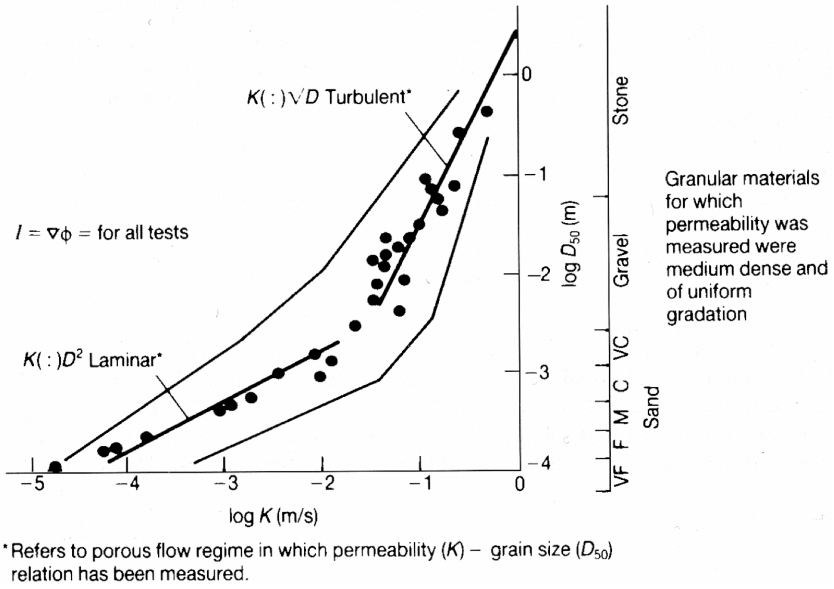

Figure 2.5: Hydraulic conductivity in relation to the nominal diameter of the soil (CIRIA; CUR; CETMEF, 2007).

Carman (1939) clearly established the validity of the equation for materials that are the size of gravel and sand. For clays, the ratio $k\frac{(1-n^2)}{n^3}$ was not constant but rather a decreasing function of porosity.

2.2.3. Forchheimer

According to Gu and Wang (1990), the porous flow through the sand material is dominated by laminar resistance, under coastal wave conditions. For gravel beaches and rubble-mound structures, inertial and turbulence resistance are also important. All three resistance components are of importance in small-scale physical model tests (Gu & Wang, 1990). The inertial resistance term is only relevant for non-stationary flow. In that case, the coefficient b in the second term has to be corrected with a factor that depends on the wave cycle (Van Gent, 1995). Dimensionless coefficients α and β can be experimentally determined (Schiereck & Verhagen, 2019). The extended Forchheimer equation describes the non-stationary porous flow.

$$I = \underbrace{au}_{\text{laminar friction term}} + \overbrace{bu|u|}^{\text{turbulence friction term}} + \underbrace{c\frac{du}{dt}}_{\text{inertial resistance term}} \tag{2.8}$$

$$a = \alpha \frac{(1-n)^2}{n^3} \frac{\nu}{g d_{(n)50}^2} \quad b = \beta \frac{(1-n)}{n^3} \frac{\nu}{g d_{(n)50}} \tag{2.9}$$

Equation 2.10 shows an indicator for non-Darcy flow (Forchheimer number: F_0) and the error of ignoring the non-Darcy effect (E). Equation 2.10 shows that the non-Darcy effect increases with an increase in filter velocity (E. Ghane, 2014). The filter velocity is u, μ is the dynamic viscosity, and ω is the constant in the Forchheimer formula.

$$F_0 = \frac{\omega \kappa \rho g u}{\mu} \quad E = \frac{F_0}{1 + F_0} \tag{2.10}$$

2.2.4. Oscillatory flow

Van Gent (1995) performed oscillatory flow tests for relatively large Reynolds numbers and for low Keulegan-Carpenter numbers. The Reynolds number (Re) is the ratio of inertial forces to viscous forces, whereas the Keulegan-Carpenter number (KC) describes the relative importance of inertia and drag forces.

$$Re = \frac{u \cdot D}{\nu} \qquad KC = \frac{\hat{U}T}{nD_{n50}} \tag{2.11}$$

The research of Van Gent (1995) showed that the term of turbulence friction is larger mainly for oscillatory flow conditions than for stationary flow. A lower Keulegan-Carpenter number means a higher influence of the inertial resistance. This can be explained by the destruction of the boundary layers and possibly small eddies when the flow direction changes.

Sand retention is affected by the hydraulic gradients that can cause the movement of fine materials and by its geometric relationship with coarse material (Polidoro et al., 2015). Only when the hydraulic gradient exceeds a limit, set by the geometric relationship between the fine and coarse material, suffusion occurs. Suffusion means that, in the case of a land reclamation protected by a rubble mound structure, the reclaimed sand is carried by water flow through the voids in the rubble core.

2.3. Granular material

The filter and base materials are made of gravel and sand, which are granular materials. A granular material behaves neither as a viscous fluid nor like a solid (Hattamleh et al., 2010). Granular assemblages have interesting properties, such as arching, instability, dilatancy, and thixotropy (becoming less viscous when stress is applied). The most relevant properties for open inverted filters are discussed below.

2.3.1. Grain size distribution

The most commonly reported sediment property is its grain size distribution. There are two methods to determine the grain size distribution. For small grain sizes such as sand (0.063-2 mm), the soil can be sieved through sieves with different mesh sizes. The sieve curve can be plotted by weighing the soil residue for each sieve. When the grain size is larger, such as for gravel, the sieve openings will be blocked by using this method to determine the grain size distribution. In that case, a more precise method is used, where the weight of all individual stones is measured from a sample of gravel. This forms a weight distribution. Nevertheless, this weight distribution needs to be converted to a grain size distribution. Therefore, the nominal median diameter is determined by the following formula (Schiereck & Verhagen, 2019):

$$d_{n,50} = \sqrt[3]{\frac{W_{50}}{\rho_s}} \tag{2.12}$$

The nominal median diameter ($d_{n,50}$) can be related to the median diameter (d_{50}) by a shape factor (F_s). The shape factor is almost always between 0.7 and 0.9, and the most common value is 0.84 (Schiereck & Verhagen, 2019).

$$d_{n,50} = F_s \cdot d_{50} \tag{2.13}$$

When the grain size distribution is established, it can be determined if the particles have a narrow or wide grading. Narrow graded means that the particle sizes are similar, to be specific: $d_{85}/d_{15} \leq 1.5$. A wide grading means a larger difference between d_{85} and d_{15}. The type of grading is called well-graded when all intermediate particle sizes are represented. If intermediate particle sizes are lacking, the soil is called gap-graded.

2.3.2. Bulk soil parameters

There are several other soil parameters, in addition to the grain size distribution, that are relevant to designing an (inverted) geometrical open granular filter. These are explained in this subsection.

Stability Ratio

The main strength parameter against erosion is the Stability Ratio (SR). The Stability Ratio is defined as the diameter of the sieve for which 15% of the mass of the filter material is smaller, divided by the sieve diameter of which 85% of the mass of the base material is smaller: $\frac{d_{15,f}}{d_{85,b}}$. Within a filter layer with different sizes of grains, the space or escape route between the grains is determined by $d_{15,f}$. For an internally stable base layer, the largest grains of the base layer ($d_{85,b}$) get stuck in the pores of the geometrically closed filter layer and block the passage of other grains. A Stability Ratio of 5 or smaller is called a geometrically closed filter. A larger Stability Ratio can still be stable, but for geometrically open granular filters, the critical hydraulic gradient should be taken into account.

Coefficient of uniformity and of gradation

The coefficient of uniformity (C_u) and the coefficient of gradation (C_c) describe the variability of the particle sizes of the soil within a soil mixture and classify the soil as uniformly, poorly or widely graded. A higher variability in sizes gives a wider pore-size distribution and less total volume of the dominant pore within the soil mixture (Rahardjo et al., 2012).

$$C_u = \frac{d_{60}}{d_{10}} \qquad C_c = \frac{d_{30}^2}{d_{60} \cdot d_{10}} \tag{2.14}$$

According to the Unified Soil Classification System, both the coefficient of uniformity and the coefficient of gradation define if a soil is well-graded or poorly graded (Keaton, 2018, pp. 158–159). Wide-graded gravel is defined as $C_u > 4$ and $1 \leq C_c \leq 3$. Wide-graded sand is defined as: $C_u > 6$ and $1 < C_c < 3$ (Jebur, 2018).

Porosity

The ratio between the volume of pores and the total volume is described by porosity. Porosity depends on the shape of the particles, the grain size distribution, and the placement of the particles.

$$n = \frac{V_{\textbf{Pores}}}{V_{\textbf{Total}}} \tag{2.15}$$

Grain crushing

Inside granular materials multiple stress chains are involved, and these local high-stress concentrations can crush single particles under relatively low stresses. This will significantly change the mechanical and physical properties of the granular matter and could jeopardize the stability of the structure. The crushing resistance depends on the type of grain. For example, freshly quarried materials undergo fragmentation under pressures of around 1 MPa, while calcareous shells begin to crush at 0.05-0.2 MPa (Hattamleh et al., 2010). Calcareous grains are crushed more easily due to their angular shape and weaker mineralogical constitution (Wils et al., 2015).

The grain size distribution becomes less steep under crushing, and consequently the soil becomes more resistant to crushing and less permeable. The void space between the larger particles is filled with crushed material which reduces the hydraulic conductivity. Permeability influences both parallel and perpendicular hydraulic gradients. According to Wils et al. (2015), the behavior of crushable sand (calcareous grains) is significantly affected by water immediately after crushing is initiated. Oedometer tests have been performed and showed that the total settlement and crushability are higher for the wet sand.

2.3.3. Type of sand in land reclamations

The type of sand used for land reclamations depends largely on the material available at the construction site. This can range from silty sand to almost gravel. Silica sands are widely used, whereas for Dubai's land reclamation projects, crushed shell calcareous sand was used. The type of sand affects "sand aging", which refers to the time-dependent strength gain that can occur in recently placed base fills (Gunberg et al., 2007). Calcareous sand is more compressible (creep) than silica and quartz sand, but this becomes significant only at high stresses of around 800 kPa; see Figure 2.6(a). This means that grain crushing will not occur due to the self-weight of the base fill, but only due to cone penetration tests or compaction.

The fines content of the base fill has a large impact on the permeability. Khan et al. (2019) investigated this influence by testing different concentrations of plastic fines (PF) and non-plastic fines (NPF) in sands collected from different localities (CS, LS, RS). This is shown in Figure 2.6(b). It is remarkable that lower fines contents till 30% largely reduce the permeability till 0 cm/sec, after which the permeability can no longer be reduced. Usually for land reclamations, the most important criteria for the base fill are a certain maximum fine content (< 63micron) and a certain maximum particle size, so its grading is of great importance.

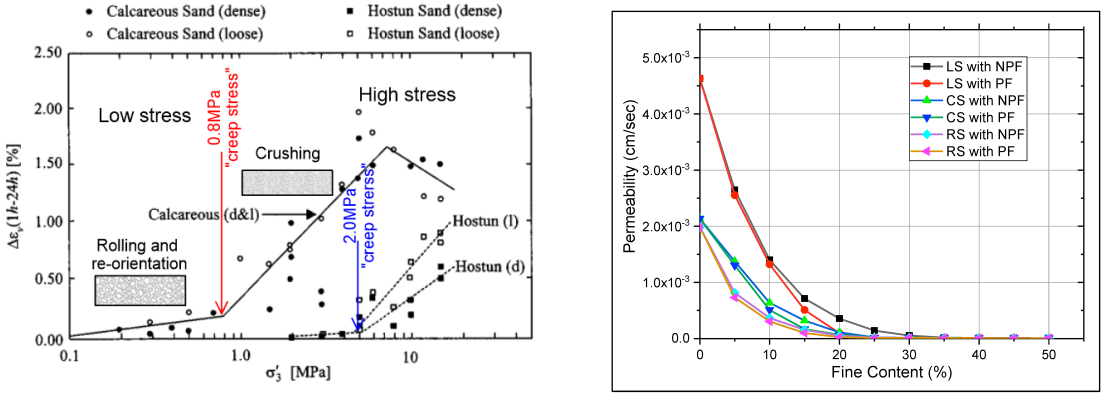

(a) Creep and crushing for different types of sand (Van Oord, 2023)

(b) Variation in permeability with different fines contents (Khan et al., 2019).

Figure 2.6: Sand crushing and the relation between permeability and fines content.

2.4. Filters

To understand how hydraulic loads can cause erosion in the base fill retaining rubble mound structure, the structure should be considered on a small scale. This section describes the flow through the pores of the granular media.

2.4.1. Geotextiles

Geotextiles are foil- and cloth-like synthetic materials that are used as filters in hydraulic engineering. It is a thin, sandtight filter that is used to separate the core of the rubble mound structure from the base fill land reclamation, see subsection 2.1.2. For geotextiles, a retention criterion is used for the accepted loss of material, and this criterion becomes more strict for cyclic loading (Schiereck & Verhagen, 2019, pp. 139–144). On the other hand, there should not be pressure build-up, so the permeability of the geotextile should be more than 10 times that of the subsoil. The geotextile can get blocked by large particles or clogged. Clogging means trapping of fine particles in the openings of the textile and this process can also take place in granular filters. Therefore, the relatively high permeability of the filter is important.

2.4.2. Geometrically closed filters

In geometrically closed filters, the fill material cannot move through the grains according to the classical filter rules. These types of filter can withstand any load because there is no critical gradient at the transition of the two layers. A geometrically closed filter should comply with three relations, see Equation 2.16,

based, respectively, on the stability between the filter layer and the base layer, the permeability, and the internal stability (Schiereck & Verhagen, 2019, pp. 131–132). The permeability rule is mainly important for large perpendicular gradients.

$$\frac{d_{15,f}}{d_{85,b}} < 5 \qquad \frac{d_{60}}{d_{10}} < 10 \qquad \frac{d_{15,f}}{d_{15,b}} > 5 \tag{2.16}$$

2.4.3. Geometrically open filters

Erosion occurs when the loading forces on a grain are larger than the resisting forces. The Forchheimer equation, see Equation 2.8, describes the relationship between the gradient and the velocity in the filter, which is again related to the forces acting on a grain. Within an open granular filter, grains in the base layer can move through the filter layer. This erosion only occurs when the critical filter gradient is exceeded, before that the filter is stable (Schiereck & Verhagen, 2019, pp. 130–133).

These more permeable filters are usually more economical than geometrically closed filters, but detailed information on the loading gradients is required. Schiereck and Verhagen (2019) advises to discern the flow in the two main directions (perpendicular and parallel) to better understand the flow through a granular filter; see Figure 2.7.

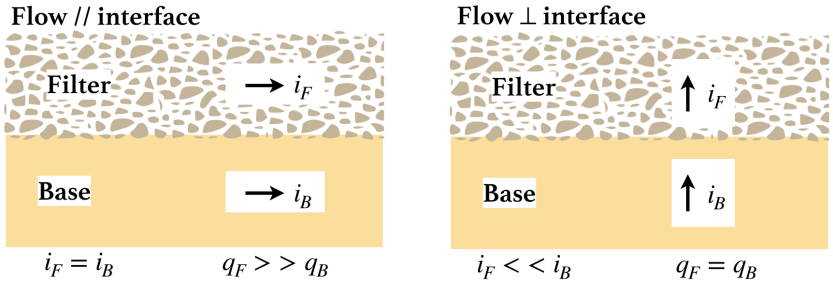

Figure 2.7: Parallel and perpendicular flow in a granular filter (Schiereck & Verhagen, 2019).

According to Graauw et al. (1984), the minimum layer thickness of the filter must be more than several times the diameter of the largest grain size. In that case, the filter structure can cope with any irregularities.

2.4.4. Parallel flow

During parallel flow, the critical gradient is defined in the filter layer and shown in Figure 2.8. Since the permeability of the filter layer is much higher than that of the base layer, the flow velocity is also much higher in the filter layer. This creates a velocity gradient at the interface, which induces a (shear) stress on the upper grains in the base layer (Schiereck & Verhagen, 2019, pp. 133–135). Graauw et al. (1984) established an empirical relation for the critical gradient under steady parallel flow, by linking the Forchheimer equation (Equation 2.8) with the threshold of movement from Shields.

$$I_C = [\frac{0.06}{n_F^3 d_{15F}^{4/3}} + \frac{n_F^{5/3} d_{15F}^{1/3}}{1000 d_{50B}^{5/3}}] u_{*c}^2 \tag{2.17}$$

The two parts of Equation 2.17 come from, respectively, the laminar and turbulent parts of the Forchheimer equation (Equation 2.8). The diameter of the base material is a measure of stability, and the diameter and porosity of the filter material are a measure of the flow through the filter. In addition to steady parallel flow, Graauw et al. (1984) also investigated cyclic parallel flow.

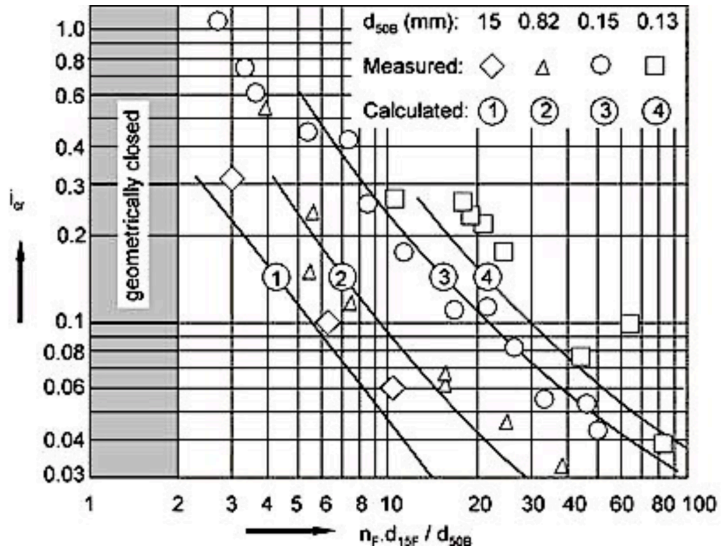

Figure 2.8: Critical parallel gradient for non-inverted geometrically open filter layers (Schiereck & Verhagen, 2019).

Cyclic parallel flow

According to the tests of Graauw et al. (1984), the critical amplitude of the hydraulic gradient initially increases with decreasing period. Cyclic flow causes hydraulic compaction, which increases the critical hydraulic gradient. After compaction, it appeared that the critical hydraulic gradient no longer depends on the period. During parallel flow tests, it was found that for cycle periods of more than 2 seconds, the critical filter velocities and gradients are the same as for stationary flow. During cyclic parallel flow, cyclic gradients perpendicular to the interface may occur, due to amplitude differences between the cyclic pressures in both materials, caused by permeability differences.

2.4.5. Shear stress

Parallel flow causes shear stress on the upper grains of the base material, which can cause erosion. Erosion is the entrainment of particles in which they are sliding, lifting, or rolling. The Shields curve relates the nondimensional shear stress on the bed to the boundary Reynolds number. The sliding of the particles is best correlated with the Shield parameter, so this is the main erosion mechanism, while lifting and rolling are much more mechanisms of individual particles (Miedema, 2010). When continuous movement of grains occurs at all locations, the friction force of the water flow exceeds the so-called critical Shields parameter. Figure 2.9 shows the original Shields curve.

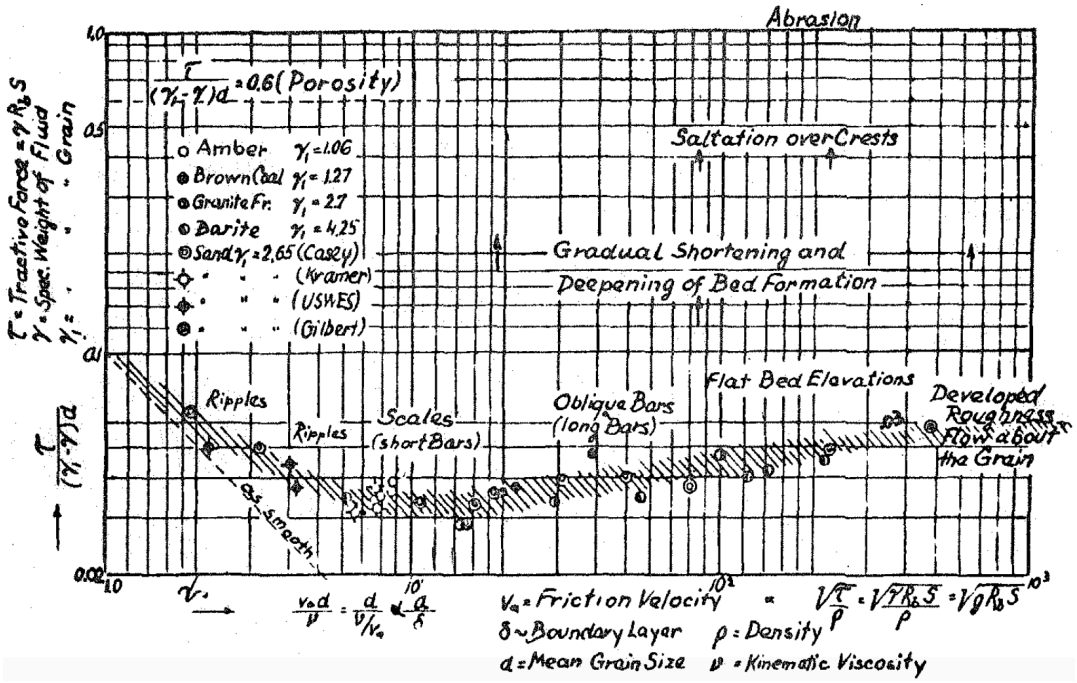

Figure 2.9: Original Shields curve (Shields, 1936).

2.4.6. Perpendicular flow

The critical gradient is defined in the base layer during the perpendicular flow, which is related to a different erosion mechanism than for the parallel flow. The filter layer has a larger permeability, which causes a much larger gradient in the base layer, because the flow in both layers is equal (Schiereck & Verhagen, 2019, pp. 133–135). In the case of a base fill retaining rubble mound structure, the base layer is on top of the filter layer. For downward flow in this situation, a geometrically closed filter is recommended because grains will easily fall through the filter layer (Schiereck & Verhagen, 2019, pp. 133–135). Fluidization occurs when the filter grains are relatively large, which means that the base layer is eroding, and so the base layer determines the stability. Between the closed limit and fluidization (piping), the arching mechanism can block the filter; see Figure 2.10. Details about arching are given in subsection 2.4.7.

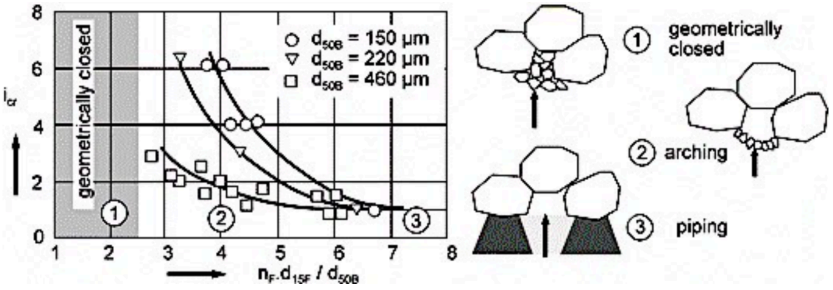

Figure 2.10: Perpendicular flow through non-inverted geometrically open filters (Schiereck & Verhagen, 2019).

Cyclic perpendicular flow

Cyclic perpendicular loading tests of Graauw et al. (1984) produced considerably different results than the stationary tests. Cyclic perpendicular gradients to the interface are caused by amplitude differences between the cyclic pressures caused by differences in permeability. Arches are probably difficult to build up and remain during cyclic loading. This can explain the lower critical gradient for both fine and coarse sand in this situation. Details about arching are given in the subsection below.

2.4.7. Arching

The scientist Robert Hooke (1635 - 1703) describes the arch as follows: 'As hangs the flexible line, so but inverted will stand the rigid arch.' When the slope of the arch at each point exactly matches the combined horizontal forces (transmitted through the arch) and vertical forces (gravity and weight of the arch) at that point, this can be considered the ideal shape of an arch (Osserman, 2010). This famous shape can be linked to a specific distribution of grains in an open filter, known as "arching."

The formation of arches is the main strength mechanism for perpendicular flow in open inverted filters. The strength of the arches depends on the Stability Ratio, the effective stress in the filter, and the angularity of the base fill material. The larger the gaps of the filter compared to the size of the base fill particles (the Stability Ratio), the larger and thus the more fragile the arches become. This decreases the critical perpendicular hydraulic gradient.

Trapdoor systems

To study arching mechanisms, trapdoor systems are often used to investigate deformation patterns and development processes. A trapdoor system, such as the test setup of Rui et al. (2016), consists of a sand chamber and moving components (movable beams, heavy steel plate, lift and indicators). Fill height (H), net spacing ($s-a$), pile width (a) and sand grain size (d) can be varied. Terzaghi (1943) described the development of the arching by the following finding: the inclination of the slip surface decreases from 90˚ to 45˚$+\varphi/2$ with increasing $\frac{H}{(s-a)}$.

The study of Terzaghi (1943) corresponds to the research of both Iglesia et al. (2013) and Chevalier et al. (2012) who described the load transfer processes during the downward movement of the trapdoor in three phases. Chevalier et al. (2012) describes first the maximum transfer phase, then the transition phase with a triangular expansion zone, and then the critical phase with vertical sliding zone boundaries. The displacement data of Iglesia et al. (2013) showed that the physical arch transformed from a curved configuration to a triangular shape and eventually to a prismatic sliding mass with vertical sides; see Figure 2.11.

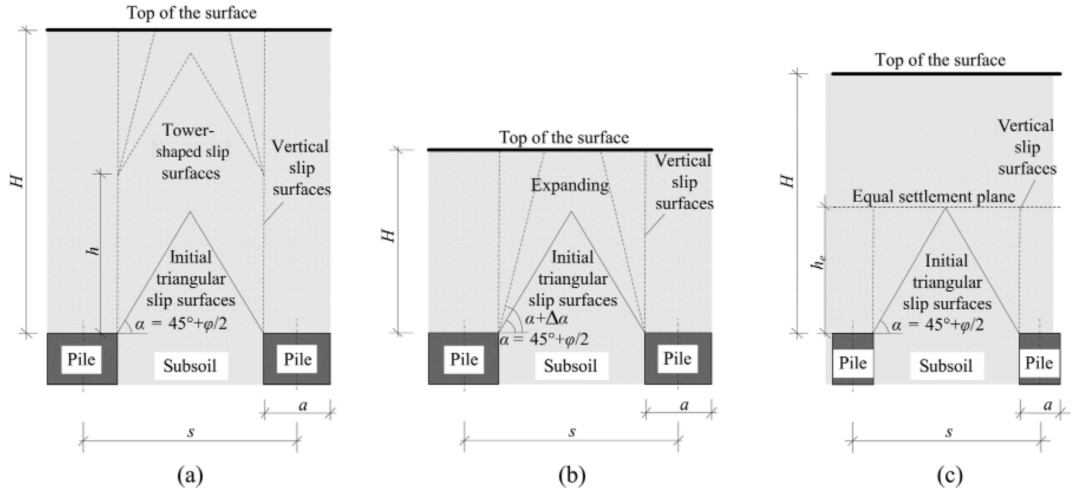

Figure 2.11: Three soil-arching patterns for unreinforced piled embankments: (a) tower-shaped development pattern, (b) triangular expanding pattern, (c) equal settlement (Rui et al., 2016).

Effect of flowing water

Besides waves, there is also the occurrence of currents from tides and precipitation. An inward current might break the arches and thus decrease the critical perpendicular gradient, and vice versa. However, when the current influences the individual grain of sand, the inward current can force the grains into the sand layer, increasing stability (Van de Ven, 2019).

2.5. Stability of open inverted filters

During the research line, as described in section 1.2, parallel, perpendicular, and combined flow configurations have been tested for open inverted filters. It is of interest how the flow is behaving during a combined flow configuration. Other interesting aspects of open inverted filters are explained in this section as well, like the stability after initial erosion, the influence of superimposed load and characteristics of the base material.

According to the research from Boersma (2020), the median grain size of the base material does not significantly influence the critical hydraulic gradient of the inverted filter. It was also found that an initially saturated filter with sand can reduce the arching effect and induce tunneling effects. This will have a negative impact on the critical hydraulic gradients. Lengkeek (2022) found that the more angular the base fill, the more permeable this sediment usually is, and this decreased the critical hydraulic gradient.

2.5.1. Combined flow

It was found that the perpendicular hydraulic gradients in the combined tests were similar to the critical hydraulic gradients in the perpendicular tests of Van de Ven (2019). It was also found that during the combined test, the critical parallel gradient was lower compared to the parallel test. Therefore, it seems like the perpendicular hydraulic gradient is governing over the parallel hydraulic gradient. However, Lengkeek (2022) concluded that the top of the physical model was leaking during parallel configuration tests. This means that the influence of only the parallel hydraulic gradient has not yet been researched. Furthermore, Lengkeek (2022) found that the parallel hydraulic gradient appeared to have no influence on the perpendicular hydraulic gradient. This means that the parallel and perpendicular components of the hydraulic gradient can be analyzed separately to determine which one governs and which one can be ignored.

Graauw et al. (1984) researched a flow oblique to the interface of a non-inverted open filter. This may be interpreted as the combined flow. It was found that the critical hydraulic gradient parallel to the interface hardly varies for critical perpendicular gradients less than 0.5, as can be seen in Figure 2.12. Only when a large perpendicular gradient is applied, the critical parallel hydraulic gradient reduces to 0. In the case of an inverted open filter, this value will be lower because the force of gravity has a negative impact on the critical perpendicular hydraulic gradient.

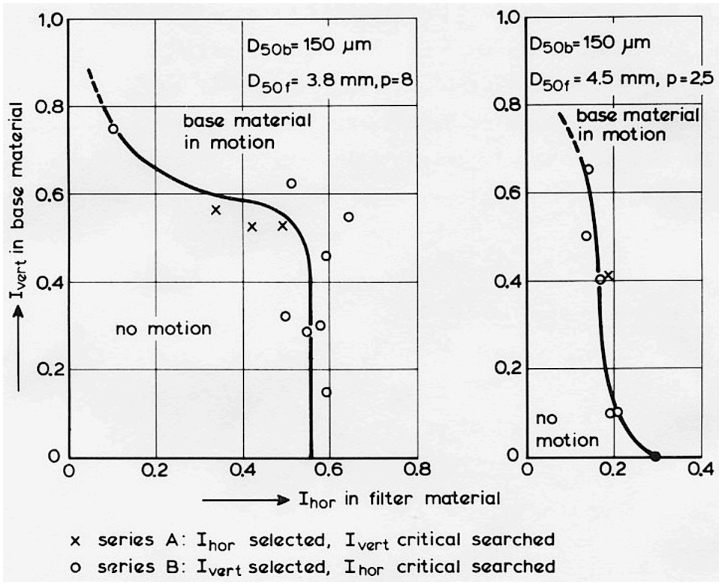

Figure 2.12: Critical hydraulic gradients with steady flow angular to interface (Graauw et al., 1984).

2.5.2. Stability after initial erosion

Bratli and Risnes (1981) performed an arching experiment with a steel cylinder with a central unconsolidated sand within. A piston compressed the sand vertically and a fluid was forced through the sandpack

where the flow rate was increased until some sand left the cylinder at the bottom. It turned out that the flow rate could be further increased until another small amount of sand left the cylinder, and so on, until the total sandpack collapsed. This depends on the strength of the sand. As long as the cohesive strength and failure angle of the sand are large enough compared to the uniaxial tensile strength, the shell collapses occur (Bratli & Risnes, 1981). This means that a base fill with a relatively high cohesive strength and/or failure angle can have erosion from shell collapses from the arches at a certain hydraulic gradient, without reaching the ultimate critical hydraulic gradient. The research of Lengkeek (2022) found indications of an armoring effect where broken arches were reformed to a more stable configuration.

2.5.3. Superimposed load on base-filter interface

The research of Lengkeek (2022) showed that the higher the surcharge applied to the inverted filter, the higher the critical perpendicular hydraulic gradient. This can be explained by the increase in strength of the arches due to superimposed load. According to Graauw et al. (1984), for the higher values of the surcharge (σ), the critical hydraulic gradient (I_{cr}) increases less, see Figure 2.13. When local fluidization occurs (SR > 12.2), the effect of the superimposed load on the critical hydraulic gradient is reduced.

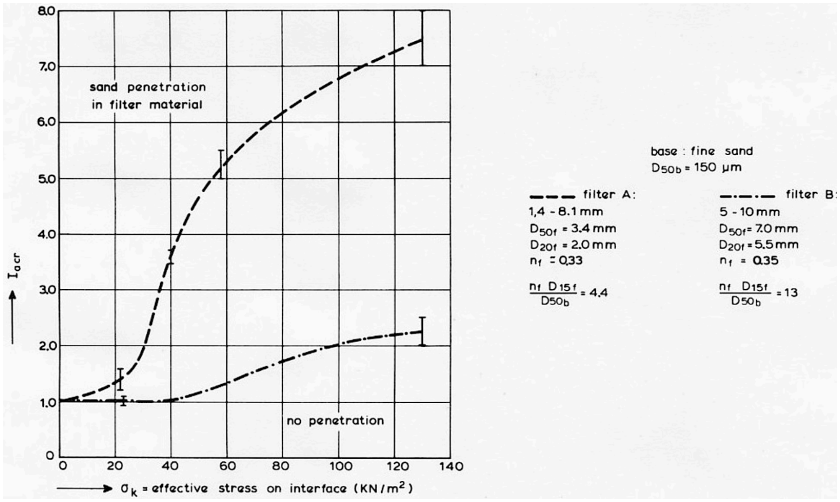

Figure 2.13: Effect of superimposed load with cyclic flow perpendicular to interface (Graauw et al., 1984).

The influence of a surcharge on the critical parallel hydraulic gradient has not been investigated by Graauw et al. (1984). Because the critical parallel hydraulic gradient depends mainly on the shear velocity of the filter layer on the base material, stronger arches will have a less positive impact. However, compaction of the base and filter material also has a positive impact on the critical parallel hydraulic gradient. This enhancement of the filter characteristics is a side effect of the superimposed load.

2.5.4. Fines and graded base material

A base material is internally stable if none of the fractions starts migrating due to the effect of a specific water motion. For a more graded base material, this can be significant when the finer fraction is not internally stable and is lost through the filter material. In the case of graded base material, a higher concentration of migrated material was measured, so a less functioning open filter was measured (Graauw et al., 1984). This reduces the critical hydraulic gradients, because it can easier fluidize the base material and reduce the threshold shear stress.

Most of the research that predicts the threshold of erosion with the Shields curve uses uniformly graded sediment. The parallel steady-flow results of Graauw et al. (1984) show a higher critical gradient in the case of fine base material. Sediment with a significant fine content means that more than 10% of its mass consists of sediment that is finer than 63 μm. These sediments are called ”cohesive” sediments when they consist of clay, because the finer sediments cling together when they are moisty by means of cohesive bonds (Winterwerp & van Kesteren, 2004). However, they can also cling together due to negative pore pressures, because non-clay mineral particles are non-cohesive. This is the case for most fine-content sediments, including marine sediments. The flow is laminar within fine sediments; there-

fore, the Reynolds number of the grain ($Re_{d_{50}}$) is not expected to alter the flow regime within the soil (Mohr et al., 2021).

Mohr et al. (2021) experimentally investigated the erosion threshold of fine-grained sediments with ensured variations in the particle size distribution (fines content), bulk density, and hydraulic permeability. All the investigated samples included silica, carbonate and marine sediments with limited clay minerals. According to Mohr et al. (2021) only permeability appeared to independently correlate with the observed range of threshold measurements. It has been found that the threshold shear stress for sediments with a significant fines content exceeds the prediction of the Shield curve by up to an order of magnitude. The fines content does not appear to independently explain the threshold shear stress across different sediments, but rather the effects of the fines content coupled with density. The threshold shear stress can also be altered by the shape of the particles, the plasticity index and the orientation and fabric of the sediment particles, which could also be related to permeability (Mohr et al., 2021).

Various researchers have reported that the threshold shear stress increases steadily or abruptly with an increase in fines content. For example Mitchener et al. (1996) found that adding sand to mud, or vice versa, increases the resistance to erosion and reduces erosion rates when the critical shear stress of erosion is exceeded. The highest values for the erosion shear stress of homogeneously mixed beds occur at a maximum in the region of 30 to 50% sand by weight. The most significant effect on erosion resistance occurs by adding small percentages of mud by weight to sand. The mode of erosion also changes from cohesionless to cohesive behavior at low mud content added to the sand, with a transition occurring in the region of 3% to 15% mud by weight; see Figure 2.14.

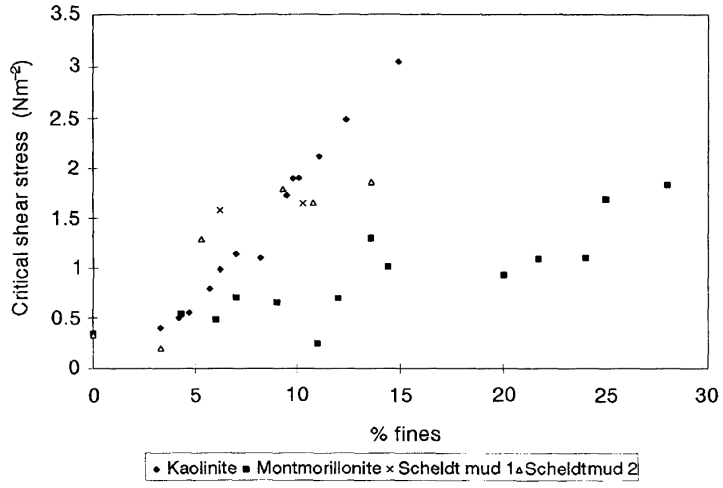

Figure 2.14: Critical shear stress for erosion against % fines for different types of cohesive material (Mitchener et al., 1996).

2.5.5. Inclined filter

According to den Bos and Verhagen (2018, p.86) a gentle, regular rubble mound structure has a slope of around 1:1.5. The gentler the slope of the rear side of the rubble mound structure, the less damage occurs because the impact caused by wave overtopping is distributed over a larger area. In the case of a rubble mound structure with base fill, the slope at the rear end is somewhat more gentle, but definitely not horizontal. On the other hand, a steeper slope at the rear end is more economical. Because the filter is inclined and placed at the rear end of the rubble mound structure, symmetry of the flow is rarely seen in reality. Van de Ven (2019) estimated the flow for an inclined filter with a numerical model. It turned out that the perpendicular gradients inward of the sand layer were larger than the outward gradients. For parallel flow, the downward gradients were larger than the upward parallel gradients.

The influence of inclination on the mechanics of the filter can be explained by two significant differences. First of all, the primary soil pressure is not perpendicular to the base-filter interface when the filter is inclined. This can influence the arching mechanism of the soil in the base fill. Second, the force of gravity does not work perpendicular to the base-filter interface. Because the gravitational forces work on an angle to the interface, the could reduce the destabilizing force and strengthen the filter.

2.6. Summary of literature study

- The hydraulic gradient in an open rear rubble mound structure increases with increasing wave period, wave height and/or wave length and closer to sea water level (SWL) (Vanneste & Troch, 2012). An irregular wave pattern might decrease the critical gradient compared to a regular wave pattern. Furthermore, oblique wave attack creates long shore currents, i.e. another parallel gradient in another direction. Polidoro et al. (2015) concluded that the hydraulic gradient did not exceed 0.03 within the core at the downward extend of the geotextile, Van de Ven (2019) modeled the perpendicular gradient in the base fill which ranged between 0.2 and 0.6.
- The **coefficient of uniformity** (C_u) and the coefficient of gradation (C_c) describe the variability of soil particle sizes within a soil mixture. Grain crushing will not occur due to the self-weight of the base fill (Hattamleh et al., 2010). The type of sand used for land reclamations is largely dependent on the material available on the construction site and the most important criteria for the base fill is a maximum fine content ($<$ 63micron).
- A geotextile can get blocked by large particles or clogged. A geometrically closed filter is recommended for inverted filters (Schiereck & Verhagen, 2019, pp. 133–135). According to Graauw et al. (1984), the minimum layer thickness of an open granular filter must be more than several times the diameter of the largest grain size to cope with irregularities. Within an open granular filter, grains in the base layer can move through the filter layer. This erosion only occurs when the critical filter gradient is exceeded, before that the filter is stable (Schiereck & Verhagen, 2019, pp. 130–133), so this requires detailed information on the loading gradients.
- During **parallel flow**, a velocity gradient at the interface occurs, which induces a (shear) stress on the upper grains in the base layer (Schiereck & Verhagen, 2019, pp. 133–135). The diameter of the base material is a measure of stability and the diameter and porosity of the filter material is a measure of the flow through the filter. During cyclic parallel flow, cyclic gradients perpendicular to the interface may occur because of the amplitude differences between the cyclic pressures in both materials.
- During **perpendicular flow** in open inverted filters, the smaller hydraulic conductivity of the sand causes a much larger gradient in the base layer. The formation of arches is the main strength mechanism, which depends on the Stability Ratio, the effective stress in the filter, and the angularity of the base fill material. It is difficult for arches to build up and remain during cyclic loading, which explains the lower critical gradient in this situation.
- Graauw et al. (1984) found that during combined flow in a non-inverted open filter, the critical hydraulic gradient parallel to the interface is constant for varying low critical perpendicular gradients ($<$ 0.4). This suggests that in a non-inverted open filter with combined flow, the parallel gradient is critical instead of the perpendicular gradient.
- The research of Bratli and Risnes (1981) concluded that a base fill in a cylinder can have erosion at the bottom from the collapse of the shells of the arches at a certain hydraulic gradient, without reaching the ultimate critical hydraulic gradient.
- According to Graauw et al. (1984), the strength of the arches increases due to **superimposed load**. However, for higher values for the surcharge, the critical hydraulic gradient increases less. The influence of a surcharge on the critical parallel hydraulic gradient has not been investigated by Graauw et al. (1984).
- In the case of **graded base material**, a higher concentration of migrated material was measured, so a less well functioning open filter (Graauw et al., 1984).
- Finer sediments can cling together by means of cohesive bonds (Winterwerp & van Kesteren, 2004) or due to negative pore pressures. The threshold shear stress for sediments with a significant **fines content** exceeds the prediction of the Shield curve (Mohr et al., 2021). The most significant effect on erosion resistance occurs with the addition of small percentages of mud by weight to sand, with a transition from cohesionless to cohesive behavior occurring in the region 3% to 15% of mud by weight (Mitchener et al., 1996).

3

Numerical model

A numerical model of the expected flow in the physical model has been created and explained in section 3.1. The one-dimensional model represents the physical model and the test programs of this research. The objective of the numerical model is to understand the flow processes that occur within the physical testing facility. The flow within the filter system can be predicted by the two-dimensional model, as explained in section 3.4. The one-dimensional numerical model is based on the numerical model of Boersma (2020), and the two-dimensional model is based on the equations used by Lengkeek (2022). The relevant modifications that are made are listed in section 3.5.

3.1. One-dimensional numerical model

The physical test setup has been schematized in Figure 3.1. The relevant parameters used in the numerical model are mentioned below. According to Gu and Wang (1990), the porous flow through the base material is dominated by the laminar resistance ($-I = \frac{u}{K_s}$), so Darcy's law. For rubble mound structures, the flow type could also be turbulent or transitional. For filter material the Forchheimer formula can be rewritten as follows:

$$-I = \frac{1}{K_f}u + \omega_f u|u| \tag{3.1}$$

In which I represents the hydraulic gradient, u represents the velocity, K_f the hydraulic conductivity of the filter material and ω_f the coefficient quadratic friction term. According to E. Ghane (2014) the non-Darcy effect increases with increasing specific discharge (q). This means that Darcy's law ($-I = \frac{u}{K_f}$) may not necessarily be assumed for the filter material in the physical test setup.

From the data from the physical model, only the hydraulic gradient and the water depths can be measured, which depend on the specific discharge. By plotting the filter velocity versus the hydraulic gradient, an estimation for the value of ω_f can be made. The influence of turbulence and inertia could also be determined by the Reynolds number and Keulegan-Carpenter number, respectively (Equation 2.11).

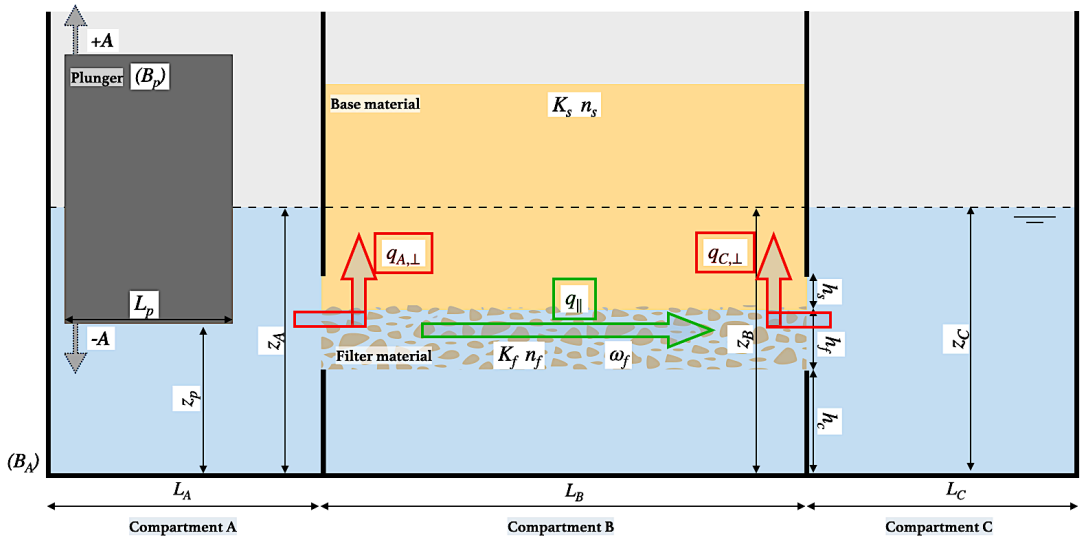

Figure 3.1: Schematization test setup with parameters used in numerical model. The positive direction of the specific discharges is illustrated as well.

Symbol	Definition	Unit
L_A	Length of compartment A	mm
B_A	Width of compartment A(, B, and C)	mm
L_B	Length of compartment B	mm
L_C	Length of compartment C	mm
L_p	Length of plunger	mm
B_p	Width of plunger	mm
A_p	Amplitude plunger movement	mm
$z_{p,0}$	Initial distance between bottom plunger and setup	mm
z_p	Distance between bottom plunger and setup	mm
z_A	Water depth in compartment A	mm
z_B	Water depth in compartment B	mm
z_C	Water depth in compartment C	mm
K_s	Hydraulic conductivity of base material	mm/s
n_s	Porosity of base material	-
K_f	Hydraulic conductivity of filter material	mm/s
n_f	Porosity of filter material	-
ω_f	Coefficient quadratic friction term	s^2/mm^2

3.2. Inducing porous flow

In order to understand the flow processes, the numerical model must calculate the pressure distribution within the filter system. The flow in the model is induced by the oscillating movement of the plunger in compartment A. The complete plunger programs are modeled. A plunger program represents the complete movement of the plunger to generate hydraulic gradients in the physical model in an ascending manner. "Reference heights" are included at the highest and lowest positions of the plunger, to create moments ("reference times") of hydrostatic pressure that can be used to check the "calibration" formulas of the pressure sensors. Furthermore, uniform accelerations and decelerations are taken into account for a precise development of the water depth in compartment A. With these adjustments, the whole development of changes in water depth and perpendicular and parallel hydraulic gradients during a test are modeled. The details of the physical plunger are shown in Appendix A, and the different plunger programs are described in Table 4.1.

The movement of the plunger in the numerical model is described as follows: Each test segment starts at the highest position $(z_{p,0} + A_p)$ followed by the lowest position $(z_{p,0} - A_p)$ both for a period specified

by "reference time" (t_r). The switching time (t_s) indicates how long it takes for the plunger to switch between the reference heights. After the reference heights, the plunger starts to oscillate within the specified period. The plunger accelerates from $z_{p,0} - A_p$ for a period of t_a, then moves at a constant velocity and then decelerates for a period of t_d until the bottom of the plunger is placed at $z_{p,0} + A_p$. In this position, the plunger waits a certain time (t_w). Then it moves down to $z_{p,0} - A_p$, including acceleration, constant velocity, and deceleration, for the next waiting period, etc. Part of the plunger movement of plunger program 1, and the complete plunger program 2 are shown in Figure 3.2. The plunger programs are specified in Table 4.1.

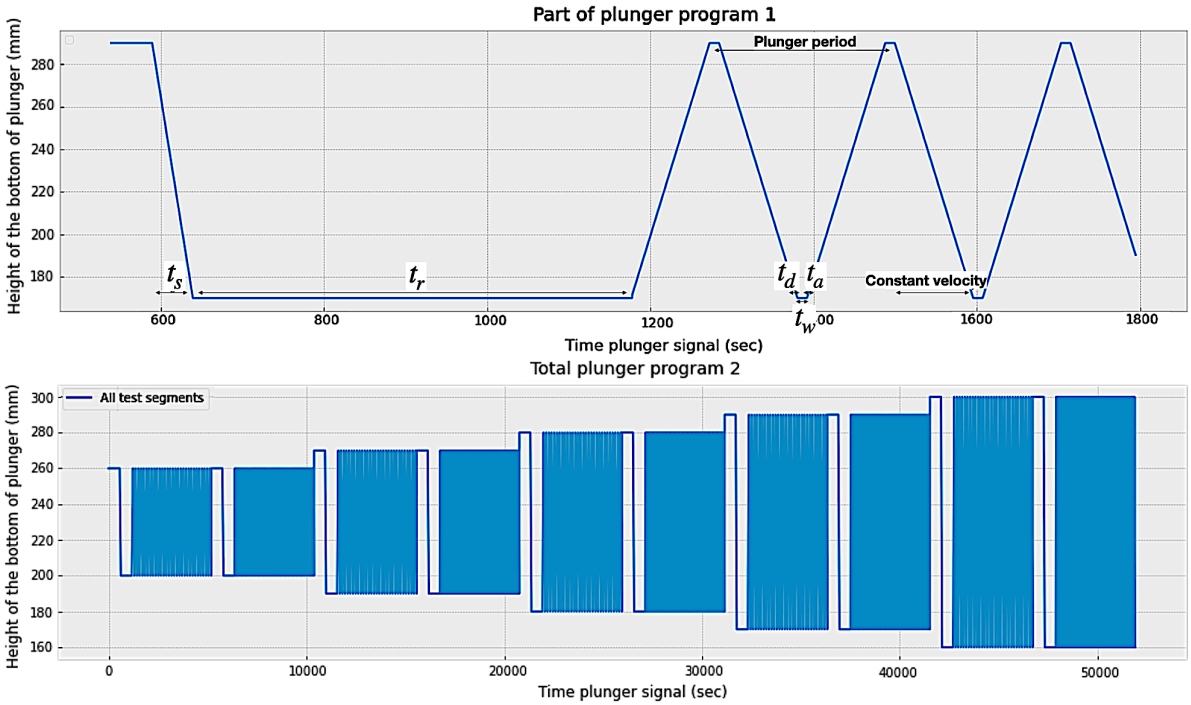

Figure 3.2: Part of plunger program 1, with a period of 120 sec and a waiting time of 6 sec. Plunger program 2 with a period of alternately 72 and 36 sec, an initial position of the plunger at 230 mm from the bottom and an amplitude of 30 till 70 mm. Plunger programs are specified in Table 4.1.

The plunger is partly underwater, and its movement influences the change in water depth in compartment A, which then influences the water depth in the other compartments. According to Archimedes, the change in submerged volume of the plunger causes a change in the water depth of the area around the plunger within compartment A. This means that the water depth in compartment A (z_A) is inversely related to the distance between the bottom of the plunger and the bottom of the model (z_p). The other parameters that are important for the volume balance are the length and width of the plunger (L_p, B_p) and of compartment A (L_A, B_A). The change in water depth in compartment A, based on the movement of the plunger and assuming that there is no flow of water to compartment B, is described in Equation 3.2.

$$z_A(t+1) = z_A(t) - \frac{\frac{\delta}{\delta t} z_p \cdot L_p \cdot B_p}{L_A \cdot B_A - L_p \cdot B_p} \tag{3.2}$$

3.3. Flow configurations in numerical model

The water depth changes in compartment A create a head difference that causes porous flow through the grains. The hydraulic gradients for each flow configuration and the resulting specific discharge are explained below. This determines the water depths in all three compartments.

3.3.1. Hydraulic gradients

During parallel flow, the hydraulic gradient depends on the difference in water depth between compartments A and C, divided by the length of compartment B. For the perpendicular flow configuration, there

is only a flow between compartments A and B. The difference in water depth in compartment A and the ground water level in B over the height of the water level in the sand layer determines the hydraulic gradient for the perpendicular flow configuration ($I_{\perp,A}$). Only the height of the sand layer is taken into account, due to the relatively low permeability, as explained in subsection 2.4.6. In case a perpendicular hydraulic gradient occurs over the filter layer as well, this material is part of the calculation as well. This turned out to be the case for the physical model, the adjustment is described in chapter 5 by Equation 5.1. For the combined flow configuration, there is also a perpendicular hydraulic gradient between compartments B and C ($I_{\perp,C}$). The formulas for the hydraulic gradients are as follows:

$$i_{\parallel}(t) = \frac{z_C(t) - z_A(t)}{L_B} \tag{3.3}$$

$$i_{\perp,A}(t) = \frac{z_B(t) - z_A(t)}{z_B(t) - h_c - h_f} \quad i_{\perp,C}(t) = \frac{z_B(t) - z_C(t)}{z_B(t) - h_c - h_f} \tag{3.4}$$

3.3.2. Specific discharge

The specific discharge from compartment A to B and C, and from compartment C to B are considered positive; see Figure 3.1. During the parallel flow configuration, only the specific discharge through the filter layer (h_f) and sand layer covered with geotextile (h_s) is important, and thus the hydraulic conductivity of the filter layer (K_f) and the sand layer with geotextile (K_s). This in relation to the hydraulic gradient at a certain moment causes a parallel specific discharge through the setup ($q_{\parallel}$). The parallel gradients are described with Equation 3.5 and Equation 3.6.

The perpendicular flow configuration does not use compartment C, so its specific discharge only depends on the water levels in compartments A and B ($q_{\perp,A}$). For perpendicular flow, the hydraulic gradient to induce erosion is only significant in the sand layer, see Equation 3.7. During the combined flow configuration, there is a parallel and perpendicular specific discharge. This perpendicular specific discharge ($q_{\perp}$) depends both on the water depths in compartments A and C ($q_{\perp,A}$ and $q_{\perp,C}$). The formulas for the specific discharge according to Forchheimer are given below.

$$-I_{\parallel,f}(t) = \frac{1}{K_f \cdot h_f} q_{\parallel}(t) + \frac{\omega_f}{h_f^2} q_{\parallel}(t)|q_{\parallel}(t)| \tag{3.5}$$

$$-I_{\parallel,s}(t) = \frac{1}{K_s \cdot h_s} q_{\parallel}(t) \tag{3.6}$$

$$-I_{\perp,A}(t) = \frac{1}{K_s \cdot L_B} q_{\perp,A}(t) \tag{3.7}$$

$$-I_{\perp,C}(t) = \frac{1}{K_s \cdot L_B} q_{\perp,C}(t) \tag{3.8}$$

$$q_{\perp}(t) = q_{\perp,A}(t) + q_{\perp,C}(t) \tag{3.9}$$

3.3.3. Water depths

The water depths within the different compartments depend on the movement of the plunger, see Equation 3.2, and the specific discharges. For the parallel flow configuration, the parallel specific discharge is of importance: $q_{\parallel}$. During the perpendicular flow configuration, only the specific perpendicular discharge between compartments A and B, $q_{\perp,A}$, should be taken into account. The combined flow configuration takes into account both these specific discharges, as well as the specific discharge between compartments B and C: $q_{\perp,C}$. The formulas to calculate the water depths in each compartment are given below for the combined flow configurations. Water depths during the parallel or perpendicular flow configuration are calculated by only part of these equations.

$$z_A(t+1) = z_A(t) - \frac{\frac{\delta}{\delta t} z_p \cdot L_p \cdot B_p + (q_{\parallel} + q_{\perp,A}) \cdot \Delta t \cdot B_A}{L_A \cdot B_A - L_p \cdot B_p} \tag{3.10}$$

$$z_B(t+1) = z_B(t) + \frac{(q_{A,\perp} + q_{C,\perp}) \cdot \Delta t}{L_B} \cdot \frac{1}{n_s} \tag{3.11}$$

$$z_C(t+1) = z_C(t) + \frac{(q_{A,\parallel} - q_{C,\perp}) \cdot \Delta t}{L_C} \tag{3.12}$$

3.4. Two-dimensional flow

The flow through the open inverted filter can be visualized more extensively with a two-dimensional numerical model. The pressure distribution in the base material can be described with the potential flow equation. A one-way coupling can be made between the one-dimensional and two-dimensional numerical models. The water depth outputs in the different compartments of the one-dimensional numerical model can be used as input for the two-dimensional model. When assuming steady, incompressible, and irrotational flow, the two-dimensional LaPlace equation can be used:

$$\frac{\delta^2 \phi}{\delta x^2} + \frac{\delta^2 \phi}{\delta y^2} = 0 \tag{3.13}$$

Wall effects are neglected and laminar resistance is assumed to be dominant in the base material. The potential flow is discretized in the numerical approach with central differences:

$$P_{n_{j,i}} = \frac{\delta x^2 * (P_{n_{j,i+1}} + P_{n_{j,i-1}}) + \delta y^2 * (P_{n_{j+1,i}} + P_{n_{j-1,i}})}{2 * (\delta x^2 + \delta y^2)} \tag{3.14}$$

The hydraulic head at the current moment at x-position i (over the length) and y-position j (over the height) is expressed as $P_{n_{j,i}}$. This corresponds to the length and height coordinates in the two-dimensional Python-model. The boundary conditions are computed with virtual grid points. A grid of 30 points by 30 points was used.

3.4.1. Boundary conditions

At the left and right wall there is no flow possible, so a Neumann boundary condition can be used:

$$\frac{\delta P}{\delta x} = 0 \tag{3.15}$$

During the combined and perpendicular flow configuration, the hydraulic head at the top equals the water level in compartment B. This is defined by a Dirichlet boundary condition:

$$P = z_B \tag{3.16}$$

For the parallel flow configuration, no flow is possible in y-direction. This is described by a Neumann boundary condition:

$$\frac{\delta P}{\delta y} = 0 \tag{3.17}$$

At the bottom boundary of the base material for the combined en parallel flow configuration, the hydraulic head is assumed to be equal to the linear interpolation between the water depths of compartments A and C. This Dirichlet boundary condition is as follows:

$$P = z_A \cdot (x - L_B) + z_C \cdot x \tag{3.18}$$

For the perpendicular flow configuration, the hydraulic head at the bottom of the base material is assumed to be the same as the water depth in compartment A ($P = z_A$), as such no 2D effects occur in this configuration.

3.4.2. Hydraulic gradients

The hydraulic gradients can be calculated based on the differences in hydraulic heads:

$$I_{\perp_{j,i}} = \frac{P_{j+1,i} - P_{j-1,i}}{2 * \delta y} \quad I_{\parallel_{j,i}} = \frac{P_{j,i+1} - P_{j,i-1}}{2 * \delta x} \tag{3.19}$$

3.5. Modifications numerical models

The one-dimensional numerical model is based on the numerical model of Boersma (2020). Whereas the previous model only took laminar resistance into account, the current model also takes turbulence into account, as this can be required for the filter material. Additionally, the precise dimensions of the plunger are included in the formulas instead of only the width. Another plunger movement has been programmed that models its precise movement including acceleration and deceleration. This avoids instant shifts in hydraulic gradients, which would also not occur in the physical model.

Furthermore, the entire tests are programmed with all different plunger movement periods and amplitudes. This shows the expected development of the hydraulic gradients during the test, instead of only one test segment. The reference heights preceding each test segment are included as well. The two-dimensional model is based on the equations used by Lengkeek (2022). Based on the measurements in the physical model, adjustments to the two-dimensional model are shown in chapter 5. These adjustments consist of a higher hydraulic conductivity on the sides of the model, modeled by a smaller hydraulic head difference on the sides.

4

Physical model

First the test setup is explained in section 4.1 per compartment with a more detailed description of the measuring equipment in Appendix A. In the next section, section 4.2, the research method from test preparation to data analysis is explained. Subsequently, the different test configurations are visually depicted and explained in section 4.3 and section B.1. In the next section, the characteristics of the base and filter material are explained. Furthermore, an overview of the adjustments compared to the previous research is given in section 4.5. Finally, an overview of all the tests performed is given in section 4.6.

4.1. Test setup

This section provides an explication of the test setup, which remains consistent with the configuration devised by Boersma (2020) and subsequently used by Lengkeek (2022), with several improvements as explained in section 4.5. The physical model is a water resistant container comprising three compartments, depicted in Figure 4.1 and designed by DEMO.

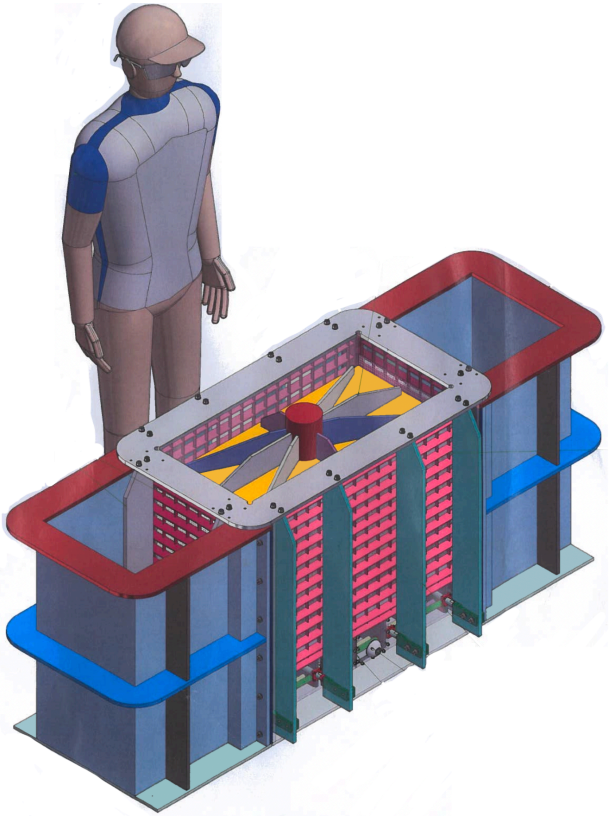

Figure 4.1: Physical model setup as designed by DEMO.

Within the illustrated setup of Figure 4.2, the water can flow through the filter in both a parallel and

perpendicular manner, which would be considered as the combined flow configuration. The initial water depth is 400 mm. The other two flow configurations are parallel and perpendicular and are explained further in section 4.3. The scale of the materials in the tests is the same as that in reality.

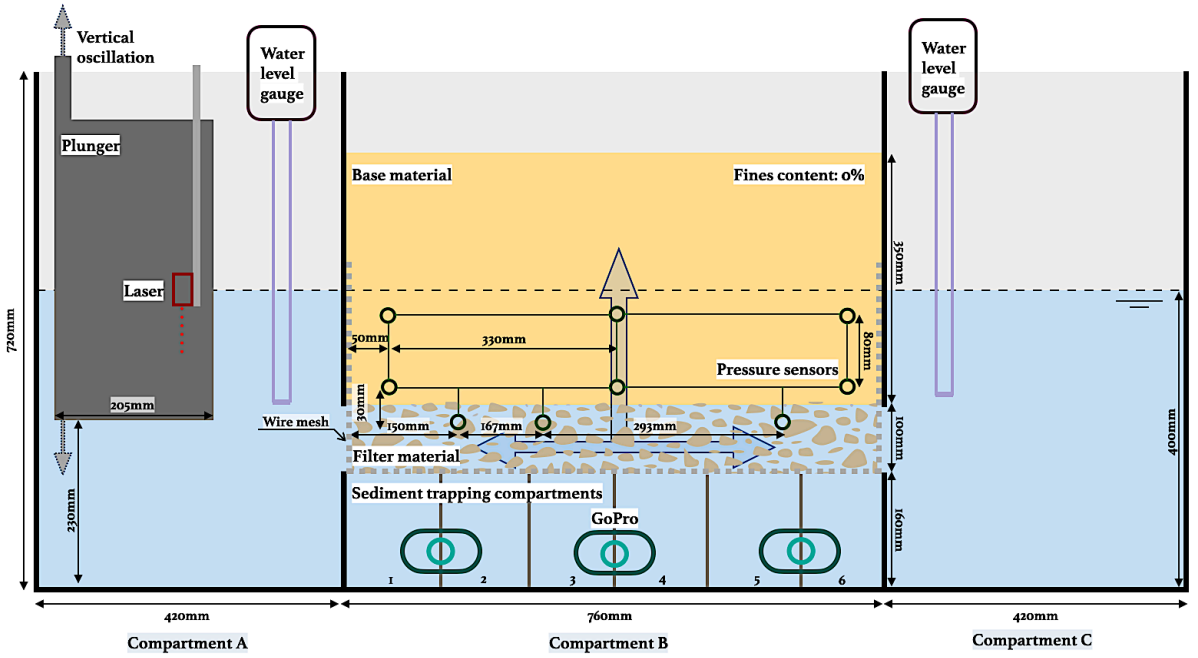

Figure 4.2: Setup of physical model in the base case situation of the combined flow configuration.

4.1.1. Compartment A

Compartment A contains a plunger that executes vertical oscillations, thus exerting control over the water depth within the setup. The plunger does not touch the bottom of the model and partially remains submerged. Variations in the water depth within Compartment A induce a hydraulic gradient within the filter system. The plunger is a hollow box made of wood. A linear motor is attached to the plunger to make it move at an amplitude of 30 to 70 mm and at different velocities that correspond to periods of 120 to 12 seconds. The position of the plunger is measured by a laser, while the water depth is monitored by water level gauges. Further details of the plunger system, laser, and water level gauge are shown in Appendix A.

4.1.2. Compartment B

The middle compartment contains the filter material and the base material. At the bottom, there are 6 bottom cells, which are individual compartments that can be used to detect erosion. The filter material is placed on a wire mesh, allowing it to retain the gravel, while the base material can erode towards the bottom cells. The wire mesh on the left and right side, as illustrated in Figure 4.2, mitigates boundary effects, and bubble wrap is placed on the front and back surfaces of compartment B. Above the 100 mm of filter material, a base material is deposited. Water level differences lead to hydraulic gradients within the filter and the base material. These hydraulic gradients are increased until erosion starts.

Underneath the base and filter material interface, three pressure sensors are strategically located to measure the water pressure relative to the atmospheric pressure (the hydraulic head). The difference in hydraulic head divided by the distance between pressure sensors indicates the parallel hydraulic gradient. In the base material, three sets of dual pressure sensors are vertically mounted to measure the perpendicular hydraulic gradients at three different locations in the base material. Pressure sensors, which are vented gauges, require waterproofing. The higher the number of pressure sensors used, the more the base layer and filter layer will be disturbed. Pressure measurements over the width of compartment B are comparable because the physical model represents a two-dimensional open inverted filter system. Therefore, only one set of pressure sensors will be used in the physical model, and this reasoning has been confirmed by the measurements of Lengkeek (2022). In addition, pressure sensors are placed

in a frame sized equivalent to the length of compartment B to ensure the same positions during each test. A detailed description of the pressure sensors and the pressure sensor frame is shown in Appendix A.

4.1.3. Compartment C

Compartment C will be used during the combined and parallel flow configuration. Water level gauges are placed in compartments A and C to measure water depths. The difference in water levels indicates the maximum parallel hydraulic gradients within the filter system and can be used as a reference for pressure sensor measurements. A detailed description of the water level gauges is given in Appendix A.

4.2. Research method

The methodology of the research is explained below. First, the methodology to perform tests with the physical model is explained, which has been carried out in the laboratory. Second, the methodology of the data analysis is given.

4.2.1. Methodology physical model

The procedure for performing a base case test in a parallel flow configuration is outlined below. The methodology varies slightly when other configurations are executed. The connections between the compartments should be adjusted according to the flow configuration. Furthermore, fines can be added to the base material and a surcharge can be placed atop the base material. The preparation of the test is of great importance to prevent erosion transport at the sides of the filter and for the visibility of erosion through the filter.

1. Dry and clean model

To initiate the preparation of the test, it is essential that the model is dry and clean. To enhance erosion visibility, black-white checkered plastic sheets are positioned at the bottom of the sediment trapping compartments. A wire mesh is placed on top of the sediment trapping compartments, of which the edges at compartments A and C should be completely sealed using water resistant aluminum tape to minimize erosion to the other compartments. Geotextile is placed between the base material and compartments A and C over a height of 100 mm, just above the filter material. This geotextile layer facilitates the flow of water through the sand layer. Bubble wrap is placed on the front and back of compartment B, completely sealed with water resistant aluminum tape, to minimize erosion on the front and back sides of the sediment trapping compartments.

2. Filter material, water depth, and pressure sensors

The subsequent stage involves positioning the 100 mm filter layer atop the wire mesh. The filter material should have been extensively washed to remove all the sand and smaller particles. Subsequently, a 20 mm wide strip of geotextile is laid over the width of the filter material close to compartments A and C and these edges are sealed to the wall. This measure serves to prevent erosion from compartment B to adjacent compartments.

The water depth in the setup is increased to around 330 mm. Thereafter, the pressure sensors are injected with water and the air bubbles are expelled. Subsequently, the entire frame with pressure sensors is placed in the setup in the wire mesh. This arrangement ensures a fixed and consistent position for each test, as shown in Figure 4.3.

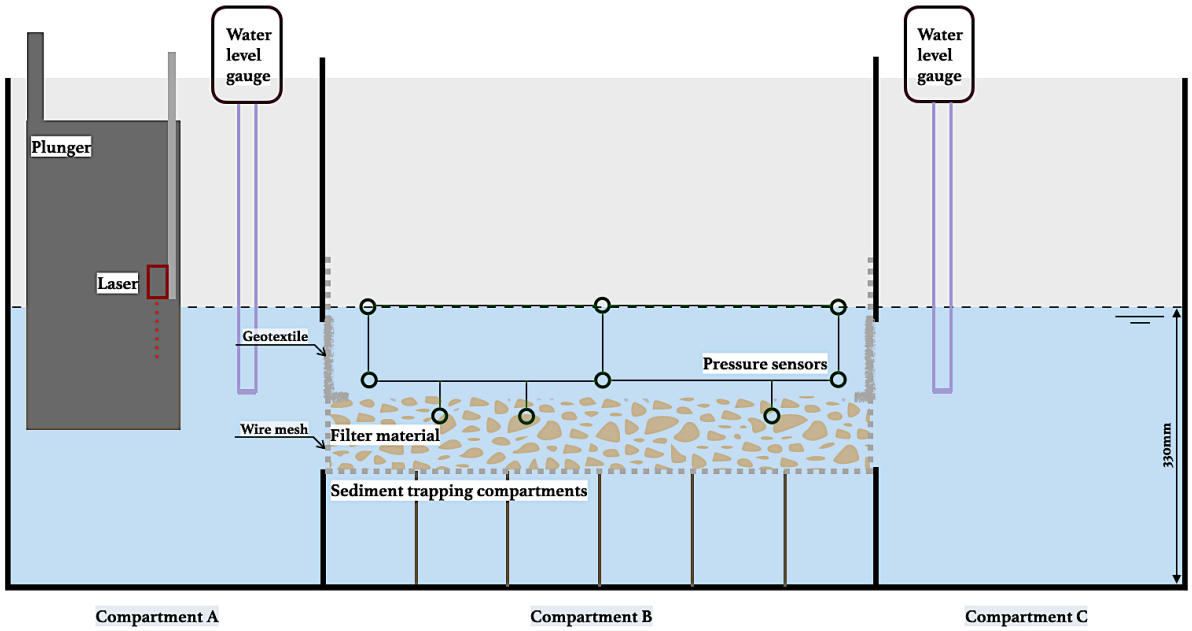

Figure 4.3: Parallel flow configuration when the filter material and pressure sensors have been placed.

3. Base material, water depth, and lighting
Subsequently, the base material is carefully added to the filter material and pressure sensors. The thickness of the base material depends on the test configuration executed. In cases involving parallel flow configuration, the base material layer should be above the wire mesh, allowing space for a sealing plate to be placed on top of the base layer. It is imperative that the base material is level. The next step involves threading the cables and air tubes through the sealing plate and interlocking them with 3D printed rubber sealing pieces. Subsequently, 63 kg of lead is placed on top of the seal to compensate for the reduced thickness of the base material layer compared to the other configurations. The base layer must at first reach the same level as the water level. The water level is adjusted to align with the plate level to release trapped air.

Once this is achieved, the sides of the plate are sealed with water-resistant aluminum tape and aqua blocker. Aqua blocker is a universal hybrid sealant. The sealing pieces surrounding the cables and tubes are screwed onto the plate and also sealed with aqua blocker.

The water level should be carefully adjusted to a few centimeters above the sealing plate, to check waterproofness but avoid high pressure build-up. Therefore, a constant water level can be guaranteed in compartment B. Adequate lighting is placed at the back of compartment B to ensure clear visibility in the sediment trapping compartments. If the water is too turbid for good visibility, it is necessary to allow the particles to settle, which takes about a day. The frame with GoPro cameras is placed in front of compartment B, as shown in Figure 4.5.

4. Execution of the test
Once a clear image is established through the GoPro cameras, the monitoring can begin with a timelapse interval of 5 seconds. Recording of sensor outputs using DASYlab is started for the pressure sensors, water level gauges, and the laser. Subsequently, the plunger system test program can be launched via Arduino. Throughout the test, the sealing plate should be regularly checked and fixed with aqua blocker when a small leak occurs.

The plunger test program has been varied throughout the research, depending on the flow configuration of the test. Table 4.1 gives the characteristics of the plunger movement per segment: the amplitude, period and velocity. This is converted to a maximum rate of change of the water depth in compartment A. The plunger range can be varied from 60 to 140 mm, while the period can be varied from 120 to 12 s. A waiting time of 6 s is implemented at the upper and lower positions, with exceptions for the shortest periods (24 and 12 s), to mitigate plunger-induced vibrations that could affect the whole setup.

Table 4.1: Test programs of the plunger described per test segment.

Plunger program (pp)		Test segment:	1	2	3	4	5	6	7	8	9	10
1	Amplitude (mm)		60	60	60	60	60	60	60	60	60	60
	Period (s)		120	108	96	84	72	60	48	36	24	12
	Velocity (mm/s)		2.2	2.5	2.9	3.3	4.0	5.0	6.7	10.0	12.0	20.0
	Maximum rate of change water depth comp. A (mm/s)		1.5	1.6	1.9	2.2	2.6	3.3	4.4	6.5	7.9	13.1
2	Amplitude (mm)		30	30	40	40	50	50	60	60	70	70
	Period (s)		72	36	72	36	72	36	72	36	72	36
	Velocity (mm/s)		2.0	5.0	2.7	6.7	3.3	8.3	4.0	10.0	4.7	11.7
	Maximum rate of change water depth comp. A (mm/s)		1.3	3.3	1.7	4.4	2.2	5.5	2.6	6.5	3.1	7.6
3	Amplitude (mm)		70	70	70	70	70	70	70	70	70	70
	Period (s)		120	108	96	84	72	60	48	36	24	12
	Velocity (mm/s)		2.6	2.9	3.3	3.9	4.7	5.8	7.8	11.7	14.0	23.3
	Maximum rate of change water depth comp. A (mm/s)		1.7	1.9	2.2	2.5	3.1	3.8	5.1	7.6	9.2	15.3

A test is made up of 10 test segments, each of which spans approximately 45 minutes. Before each test segment, the plunger is held at both the minimum and maximum positions of the test segment's range for around 10 minutes. This practice establishes hydrostatic reference heights for the pressure sensors.

5. Determination of erosion
Different levels of erosion can be indicated. The critical hydraulic gradient of an open filter within this research line is the gradient at which initial erosion occurs. Initial erosion is defined as follows: The first moment of a noticeable difference in the time-lapse images of the sediment trapping compartments 2, 3, 4 and 5. Another type of erosion is transport erosion: The start of continuous noticeable differences in the time-lapse images of the sediment trapping compartments. During tests where a fines content is added to the base material, erosion is more difficult to notice because some fines wash out and cloud the water.

Two continuous lighting LED lamps are used to light up the setup under the same conditions during each test. Three GoPro cameras are used to record the bottom cells. More information about GoPro cameras and lighting is given in Appendix A.

6. Finalizing the test
When the whole test program of the plunger system is finished, DASYlab and the GoPro cameras can stop recording. The water can be removed from the setup using a water vacuum. The sealing plate can be carefully removed when all the aqua blocker and aluminum tape has been removed. Then the base material can be carefully removed. Furthermore, the pressure sensor frame should be carefully removed, rinsed off and checked for possible sand blockage (this can influence the function of the pressure sensor). The infiltrated filter material with the base material is also removed and must be washed extensively. The bubble wrap, wire mesh, and black-white checkered plastic sheets are then removed. Finally, the setup should be completely cleaned and dried for the next test.

4.2.2. Data analysis
The hydraulic gradient cannot be measured directly but can only be determined by using pressure sensors or water level gauges. It is essential that the sensors have sufficient accuracy and reliability to obtain results. Details on the accuracy of the sensors used in the physical model and the calibration of the sensors are shown in Appendix A. The reliability of the calibrations is further discussed in Appendix C. According to technical specifications, water level gauges measure with an accuracy of 1.0 mm, the laser with a resolution of 50 μm, and pressure sensors with 0.7 mm.

Periodic comparison pressure sensors to reference water levels
As can be concluded from the reliability of the pressure sensors, elaborated in Appendix C, it is desired to frequently determine the scaling of the pressure sensors. By keeping the plunger in its minimum and maximum position before each test segment, the water levels in the setup can equalize and the last 20

to 10 seconds of each reference height can be used to calculate a linear regression for the voltage of the pressure sensors towards meters water column; see Figure 4.4.

The volume change in compartment B equals the volume change of the plunger between the two reference heights subtracted by the water level difference in compartments A and C multiplied by their free surface. The volume change in compartment B, divided by the surface of compartment B and the effective porosity of the base material, shows the change in meters water column that the pressure sensors are measuring. In this way, the voltage change of the pressure sensors before each test segment can be referred to as the hydrostatic pressure. This creates a ”calibration” formula for each pressure sensor per test segment.

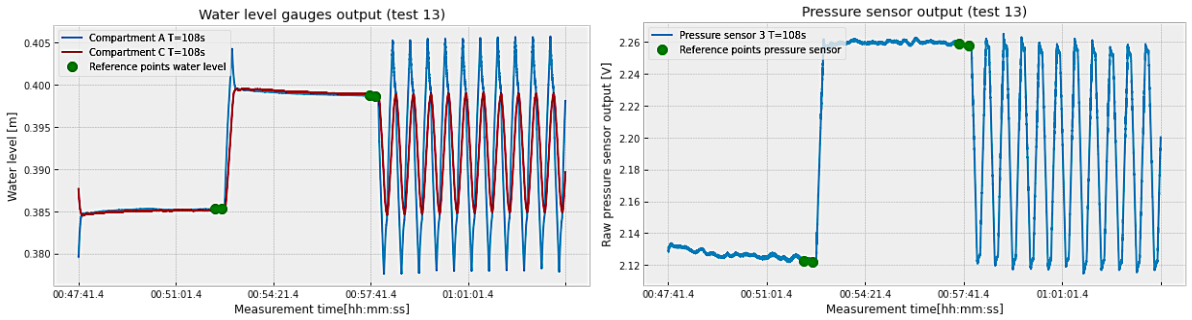

(a) Water level gauges.

(b) Raw pressure sensor output.

Figure 4.4: Reference points of water level gauges and pressure sensor output (test 13).

The average slope of the ”calibration” formula is used, as further explained in Appendix D. It is also desired to remove the offset from the pressure sensor data, as this can vary significantly according to Appendix C. This is also explained in more detail in Appendix D.

Filtering data output

In this research, the low-pass Bessel filter, of 5th order and with a cutoff frequency of 1 Hz, is applied to the pressure sensor data. The advantage of a Bessel filter is the nearly constant group delay, which means that phase distortion and time delays are minimized and this preserves the shape of the signal. This is desirable when comparing two pressure sensor signals at a certain moment. The Bessel filter is further explained in Appendix D.

Hydraulic gradients

There are different methods to calculate the hydraulic gradients in the filter system with the sensor data from the physical model. The methods are applied to all the test data and compared with the expected results of the numerical model.

During parallel flow configuration tests, the difference in water level measured by the water level gauges over the length of the filter gives a parallel gradient ($I_{\parallel}$) with an accuracy of 0.0013. The accuracy calculation is based on the accuracy of the water level gauges (1 mm) and the measurement distance (760 mm). By assuming a constant water level in compartment B during the perpendicular flow configuration and calculating the difference in water depth with compartment A divided by the water level of only the base material, gives a perpendicular gradient ($I_{\perp}$) with an accuracy of 0.006.

Pressure sensors can also be used to calculate hydraulic gradients in the filter system. By reference of the voltage to meters water column, as described in the previous subsection, the pressure difference can be calculated. The difference in pressure expressed in meters water column over the distance between the sensors gives the hydraulic gradient. For the perpendicular hydraulic gradient ($I_{\perp}$), the vertical distance between the pressure sensors located in the base material is used; this gives an accuracy of the perpendicular gradient of 0.012 based on the accuracy tests of the pressure sensors in Appendix C. The horizontal distance between pressure sensors in the filter material is used to calculate the parallel hydraulic gradient ($I_{\parallel}$) with an accuracy of 0.0035 based on the accuracy tests of the pressure senors in Appendix C. Details on how the maximum hydraulic gradient per test segment is determined are given in Appendix D.

4.3. Test configurations

In order to answer the subquestions, multiple physical model configurations are required. The initial stage involves conducting tests in base-case situations and variations in the fines content of the base material. Subsequently, the application of a surcharge on the setup is researched. These different types of test configurations are explained in the following subsections. Originally, different angles of the filter were researched as well; however, too much leakage occurred for meaningful results. The adjustments required for an inclined setup are shown in Appendix A.

4.3.1. Base cases

In the base situation of the setup, the container remains untilted and no surcharge is imposed on the base layer. The fines content is 0%, accompanied by a base layer thickness of 350 mm. In particular, the classification of the base material will be wider graded compared to previous research, with a C_U of 2.9. Three different flow configurations will be tested; parallel flow configuration (see Figure 4.5), perpendicular flow configuration (see Figure 4.6), and combined flow configuration (see Figure 4.2). Analyzing these base case situations makes it possible to compare the different flow configurations with each other and discerns the impact of the varied parameters in this research.

In the parallel flow configuration, the top of compartment B is hermetically sealed. This design requires the water to flow mostly parallel through the base filter interface; see Figure 4.5. That means that three pressure sensors are placed below the base-filter interface to calculate the parallel hydraulic gradient during this flow configuration. To compensate for the smaller layer of base material compared to the combined and perpendicular flow configuration, weights are placed on top of the sealant plate. The parallel flow configuration has a smaller layer of base material, because the sealing plate needs to be placed below the equilibrium water level.

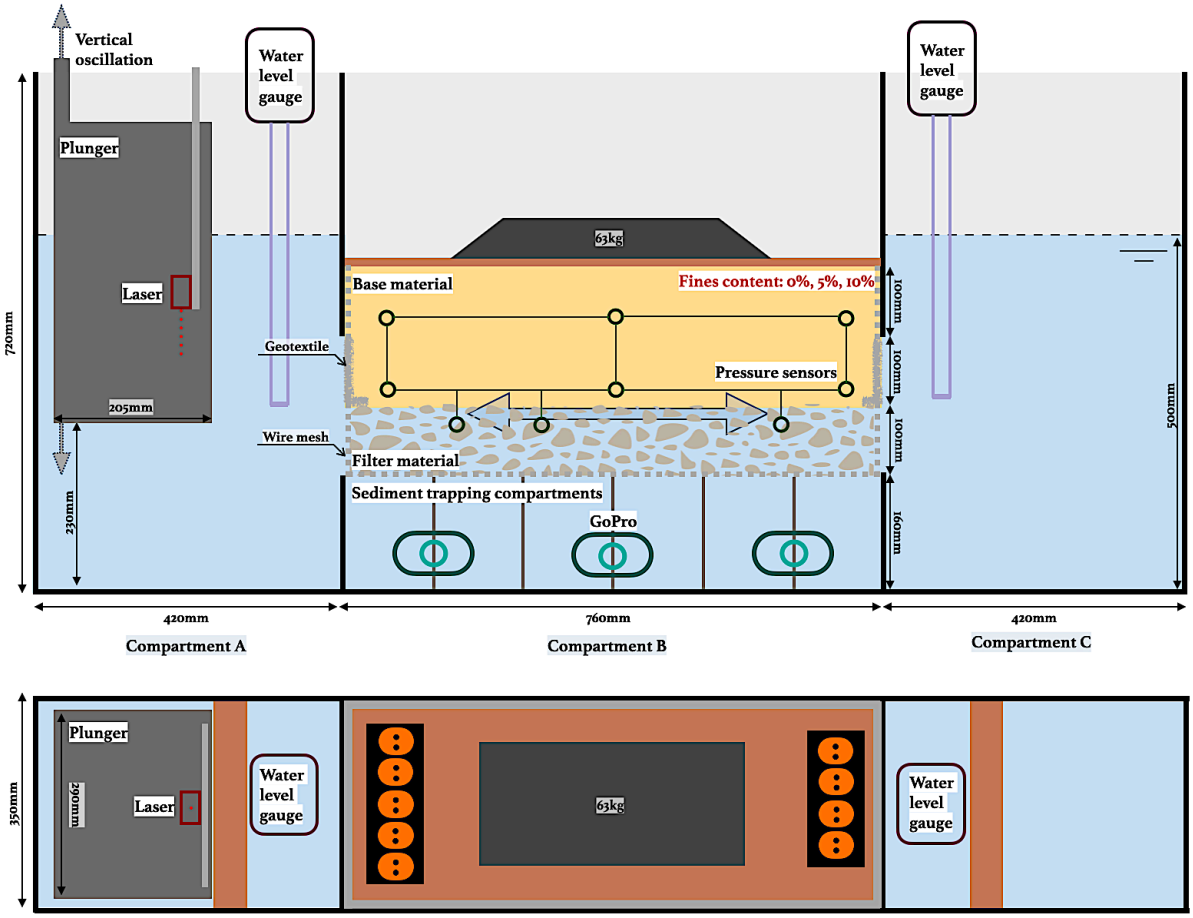

Figure 4.5: Setup of physical model in the parallel flow configuration.

In the perpendicular flow configuration, compartment C is closed from compartment B, forcing the water to flow perpendicular to the base filter interface; see Figure 4.6. Initially, the same water level is assumed in compartment A and B. During the reference heights, the change in submerged plunger volume and water volume in compartment A can be used to estimate the water level in compartment B (z_B). Pressure sensors are placed above each other at three different locations along the length of compartment B, to indicate perpendicular hydraulic gradients. During the combined configuration (see Figure 4.2) parallel and perpendicular flow conditions occur. During the combined flow configuration, the perpendicular hydraulic gradient is expected to increase closer to compartment A. As a result, this elevation can be quantified by the pressure sensors close to compartments A and C in the experimental setup.

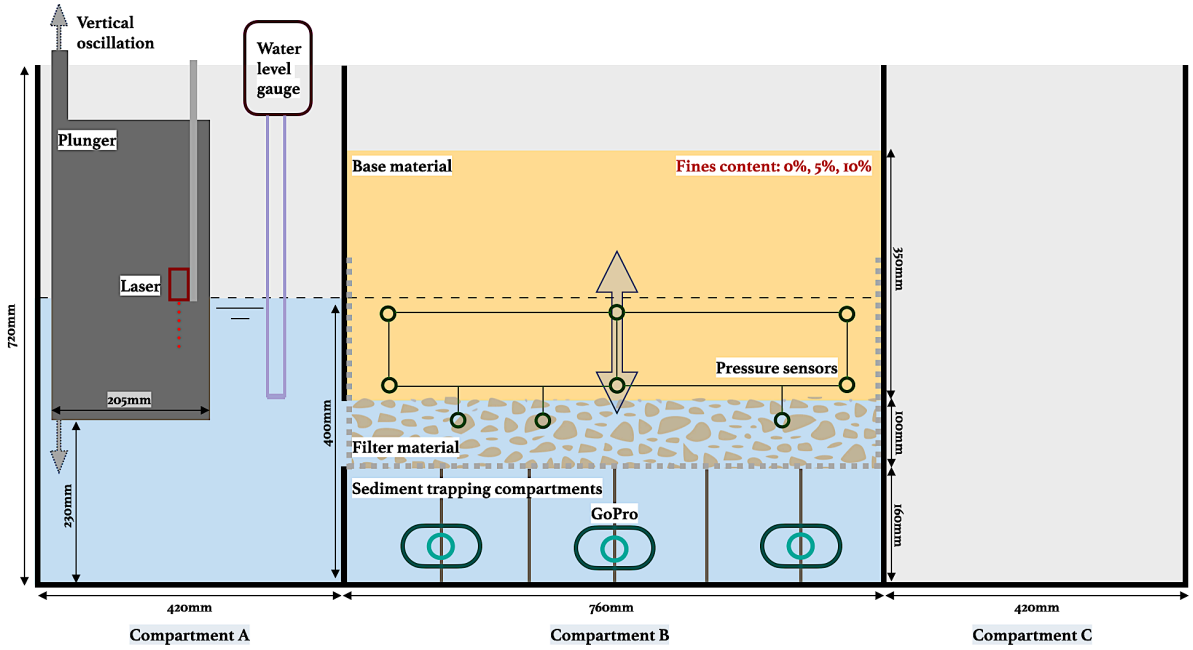

Figure 4.6: Setup of physical model in the perpendicular flow configuration.

4.3.2. Fines content

The fines content (particles < 63 microns) within the base fill affects permeability and is often an important criterion in land reclamation projects, according to Van Oord (2023). Based on examples of land reclamations from Table A.1, it is apparent that the fines content is significantly dependent on the location. A higher fines content tends to make the detection of erosion more challenging in the current experimental setup. Therefore, a fine content of 5% is tested and possibly 10 %, depending on the result. This type of experiment is carried out for both the parallel and perpendicular flow configurations.

When designing an open inverted filter, the perpendicular and parallel components of the hydraulic gradient can be analyzed separately to determine the predominant factor. The fines content is achieved through the sieving of the loam sand. It is important that the filter material is washed extensively after each test to ensure complete removal of fine particles.

4.3.3. Surcharge

The research also investigates the influence of a surcharge. During the tests of Lengkeek (2022), the critical hydraulic gradient was measured for the configuration of the perpendicular flow with a surcharge of 100 kPa. Extending this surcharge to the current setup allows an evaluation of the impact of a wider graded base fill (C_u is 2.9 instead of 1.2 and 1.6). A more powerful plunger system, with an increased amplitude, aims to cause erosion of the filter system at larger effective stresses in the base material.

For an extreme situation of land reclamation made of only a base fill protected by a rubble mound structure without the use of caissons, calculations yield a situation with 12 m of saturated sand (19.7 kN/m^3) and 3 m of dry sand (14.8 kN/m^3). Consequently, the effective vertical stress, for a horizontal

filter, at the bottom, would become:

$$\sigma'_v = 20 \cdot 12 – 9.81 \cdot 12 + 3 \cdot 16 = 170kPa \tag{4.1}$$

In reality the filter would be inclined, which would reduce the effective stress on the filter with around 30%, depending on the slope. On the other hand, if there is a structure placed on the land reclamation, this further elevates the effective stress. Therefore, it is decided that a 200 kPa surcharge will be applied to the test setup, as well as 100 kPa to determine the critical hydraulic gradients. These tests encompass all flow configurations: parallel, perpendicular, and combined, as illustrated in Figure 4.7, B.1, and B.2. The physical model has been designed to withstand additional surcharges of 200 kPa, as described by Boersma (2020). During the combined flow configuration, the progression of the perpendicular hydraulic gradient along the width can be visualized by the different pressure sensors.

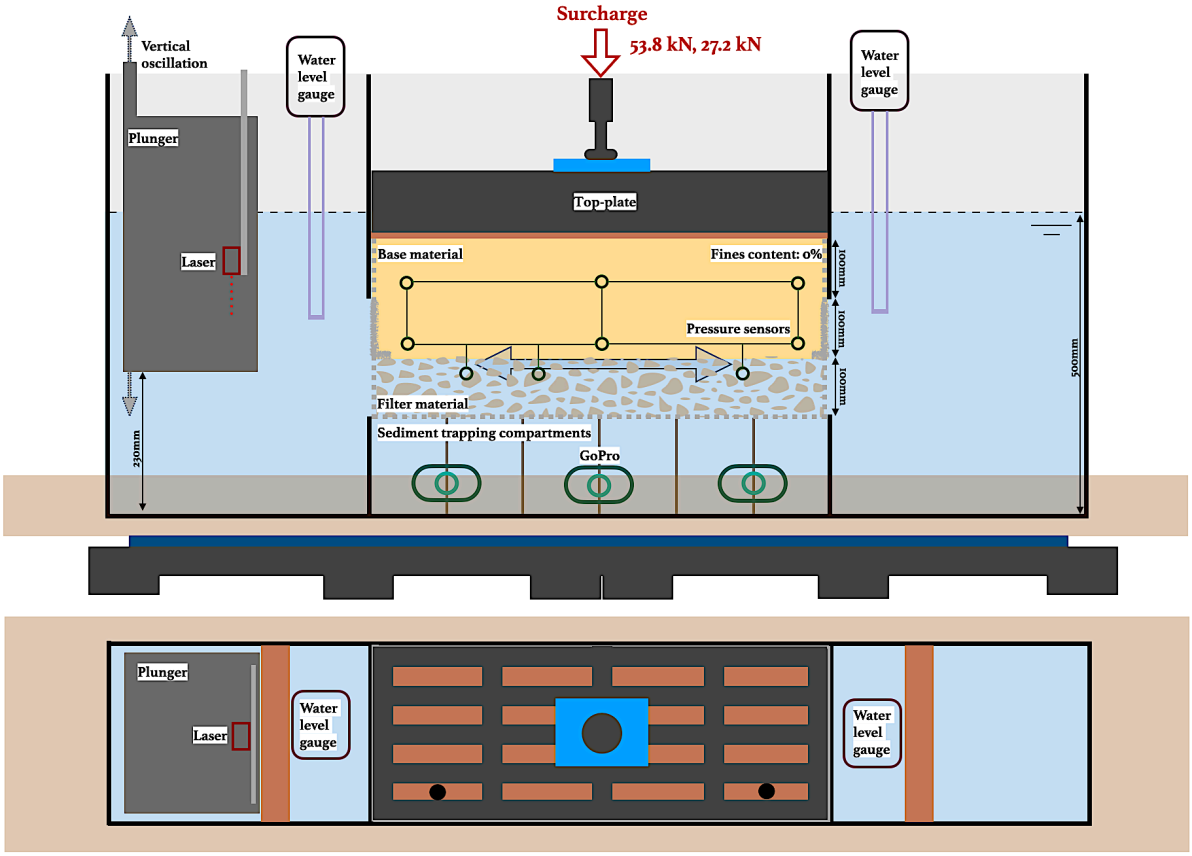

Figure 4.7: Setup of the physical model under a surcharge in the parallel flow configuration.

4.4. Base and filter material

The setup contains a layer of 100 mm of filter material. For the parallel flow configuration, the base material measures a thickness of 200 mm, while the perpendicular and combined flow configurations contain a base layer of 350 mm. The filter layer consists of gravel, while the base layer consists of sand. The characteristics of both layers are explained below and specified in Table 4.2. SR is the Stability Ratio between the base and filter material (d_{15f}/d_{85b}), which should be between 7.5 and 10 to give a reasonable ratio for an open filter in line with the research line. The Stability Ratio is one of the indicators for the strength of the open filter. The coefficient of uniformity (C_u) is aimed around 3.0 to be realistic for dredged sand and the hydraulic conductivity (K) influences the hydraulic gradients.

4.4.1. Sand

In the context of this research, a realistic value of a coefficient of uniformity (C_u) for the base material of land reclamation projects is aimed. Based on Table A.1, a coefficient of uniformity (C_u) of around 3.0

Table 4.2: Characteristics of the base and filter material in this research.

	d_{50}	C_u	C_c	SR	n	K measured	K empirical formula
Gravel	7.1 mm	1.44	1.03	-	0.39	0.2 m/s	0.056 m/s (Slichter)
Sand Combination	0.52 mm	2.9	1.5	8.0	0.32	0.6 mm/s	0.2 mm/s (Chapuis)
Sand with 5% fines	0.49 mm			8.2	0.31	0.2 mm/s	
Sand with 10% fines	0.48 mm			8.5	0.31	0.1 mm/s	

is desired with a coefficient of grading (C_c) between 0.75 and 3.0. This is wider graded than the base fills in previous research where more narrow graded sand was used: C_u of 1.2-1.7 Lengkeek (2022), C_u of 1.5-1.6 Boersma (2020) and C_u of 1.2-2.1 Van de Ven (2019). It is important that the grains exhibit minimal salt content, as elevated salt levels can damage laboratory settings. The sands used in this research originate from the North Sea, which represents narrow graded sand. By combining different sizes of sand, a desired grading of base fill can be created.

The eventually used sand combination, as well as the particle size distribution of the different types of sand where the combination is composed of, are shown in Figure 4.8. The wider graded sand distribution is eventually created by composing 1/5 of "M32 sand", 1/5 of "dyke sand", and 3/5 of the more coarse "Kremer sand", as is shown with the black line. Its coefficient of uniformity (C_u) is approximately twice as large compared to the other base fills in the research line. The characteristics of the sand combination are shown in Table 4.2. The empirical formula of Chapuis and Aubertin (2003) can be used to estimate the hydraulic conductivity of the sand (Schulz et al., 2019). Hydraulic conductivity can also be calculated using Darcy's law (Equation 2.4) with the constant head permeability test; see Figure 2.4.

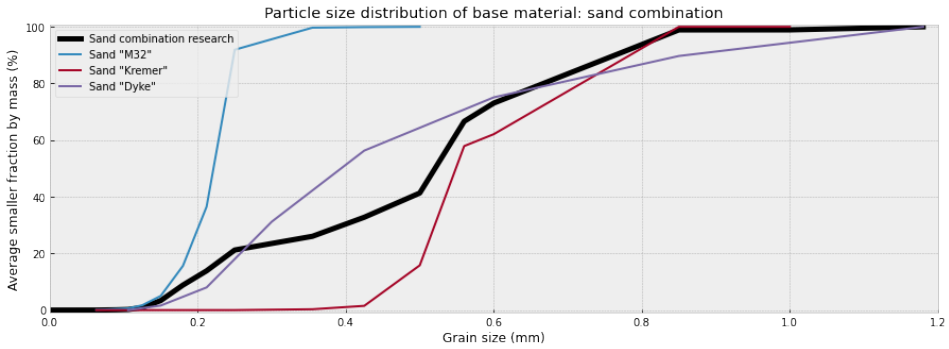

Figure 4.8: Particle size distributions of sand combination used in this research.

4.4.2. Fines

Often, the base material used for land reclamation includes a fines content. Fines are added to the base fill to investigate a possible influence on critical hydraulic gradients. Loam sand is sieved and only particles smaller than 63 microns are added to the sand fill during the fines content tests. This means that the remaining part of the base material remains the same. The particle size distributions of the base fill combination, including the fines of 5% and 10%, are shown in Figure 4.9. The empirical formula of Chapuis and Aubertin (2003) can only be used to estimate the hydraulic conductivity of sand (Schulz et al., 2019). The permeability of the sand including fines has been estimated by the permeability test with constant head (Figure 2.4), see Table 4.2.

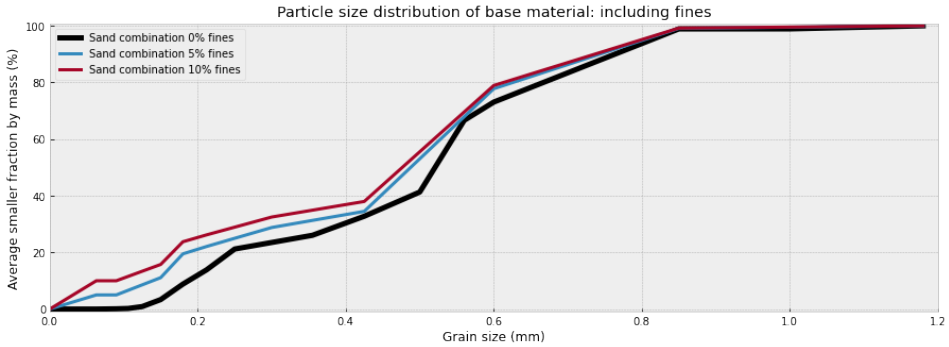

Figure 4.9: Particle size distributions of the base material including fines.

4.4.3. Gravel

The Stability Ratio between the base layer and the filter layer should be between 7.5 and 10, which is a reasonable ratio for an open filter. This means that the diameter of the sieve for which 15% of the mass of the filter material is smaller ($d_{15,f}$) should fall between 4.95 and 6.6 mm. The particle size distribution of the gravel shown in Figure 4.10 has a Stability Ratio of 8.0 with the combination of sands used in the physical model. The relevant characteristics of the gravel are listed in Table 4.2. Since natural gravel has a $d_{10} > 3$ mm and $0.23 < n < 0.5$, the empirical formula articulated by Slichter (1897) becomes applicable to approximate its hydraulic conductivity.

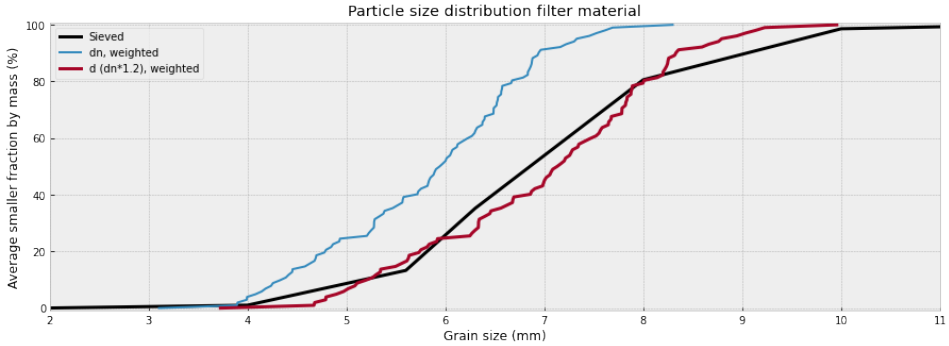

Figure 4.10: Particle size distribution of the filter material used in this research.

4.5. Adjustments compared to previous research

The physical model has been adjusted, as well as the research methodology and data analysis.

The following adjustments to the physical model have been made:

- The physical model has been improved to get reliable data for the parallel flow configuration tests. The sealing plate for the parallel flow configuration was placed below the equilibrium water level, so air was not trapped and the waterproofness could be checked. Therefore, a constant water level could be guaranteed in compartment B. Many 3D printed sealing pieces for cables and aquablocker were used to improve the waterproofness of compartment B and increase the parallel flow.
- The impact of wider graded sand ($C_u = 2.9$) has been investigated, to make the base material more realistic to dredged sand.
- Fines content in the base material is researched as well, which is another characteristic of dredged material.
- A more powerful plunger system was used, with a measurement range of 350% of the previous measurement range. This allows for greater hydraulic gradients, which is required for critical hydraulic gradients when a surcharge of 200 kPa is applied on the base-filter interface. The installation of

the water level equipment and the high point of attachment of the plunger to the linear conductor caused a reduction in the plunger area with 14% for safety. Another difference from previous research was that the linear conductor mechanism of the motor did not slip in the movement of the plunger and the amplitude of the movement did not decrease over time, which means that the hydraulic gradient did not decrease over time.

- The equilibrium water level in the base layer during the perpendicular and combined flow configuration has been decreased by 25% to increase the perpendicular hydraulic gradient.
- Pressure sensors have been replaced by temperature-compensated pressure sensors with a measurement range twice as large and more reliable. For more details on pressure sensors, see Appendix A and C. In the current research, the perpendicular pressure sensors are placed not only in the center of compartment B but also close to compartments A and C to provide information on the course of the perpendicular hydraulic gradient. Furthermore, the location of the pressure sensor frame is fixed within the setup. Air tubes connected to relative pressure sensors are replaced by stiff tubes, so the tubes cannot be pressed shut.
- From test 13, the wire mesh has been reformed so that the geotextile between the filter material and compartments A and C could be removed, to decrease the obstructing of the flow from and to compartment B.
- Water level gauges have been used instead of lasers with water-resistant paper to measure the water levels in compartments A and C. Folding of the water-resistant paper cannot occur anymore, so this adjustment greatly increased the accuracy of the water level measurements. It made it possible to measure not only the reference heights before the test segments but also the water levels during the test. This added another method to calculate the hydraulic gradients.

The following adjustments during the execution of the test have been made:

- Initially (till test 10) the perpendicular and combined flow configuration tests have had a similar plunger program compared to previous research but with a 3 times larger range. After test 10, the plunger program has been changed to a program where the range of the plunger movement is increased as well.
- The plunger program during the parallel flow configuration follows a similar increase in forcing period compared to previous research, but the range is 3 to 3.5 times as large.
- The erosion detection area has been subdivided into four different areas, which could subdivide each test into 4 separate tests.
- The hydraulic gradients in the current research are not only based on pressure sensors, but can also be calculated with water level gauges.

4.6. Test overview

Various tests have been performed with the physical model and these test configurations are described in Table 4.3. The base case tests for the different flow configurations have been repeated, to obtain a more reliable base case situation. An overview of the tests is given in Table 4.3. The most important parameters that have been researched are:

- The influence of a wider graded base material.
- Influence of the plunger movement on the perpendicular and parallel gradients in the filter system.
- The influence of a fines content on the perpendicular and parallel gradients in the filter system and on the critical hydraulic gradients.
- The influence of a surcharge at the base filter interface on the critical hydraulic gradients.

Table 4.3: Overview of the tests performed with the physical model.

Test	Test configuration	Plunger program	Stability Ratio	Fines content	Surcharge (kPa)	Base layer (mm)	Scheme
1	Perpendicular Base case (1)	1	8.0	0%	0	350	Figure 4.6
2	Combined Base case (1)	1	8.0	0%	0	350	Figure 4.2
3	Parallel Base case (1)	1	8.0	0%	0	200	Figure 4.5
4	Parallel Base case (2)	1	8.0	0%	0	200	Figure 4.5
5	Perpendicular Base case (2)	1	8.0	0%	0	700	Figure 4.6
6	Parallel Fines 5%	1	8.2	5%	0	200	Figure 4.5
7	Perpendicular Fines 5%	1	8.2	5%	0	350	Figure 4.6
8	Parallel Fines 10%	1	8.5	10%	0	200	Figure 4.5
9	Perpendicular Base case (3)	2	8.0	0%	0	350	Figure 4.6
10	Combined Base case (2)	2	8.0	0%	0	350	Figure 4.2
11	Perpendicular Surcharge 100 kPa	2	8.0	0%	100	350	Figure B.1
12	Perpendicular Surcharge 200 kPa	2	8.0	0%	200	350	Figure B.1
13	Combined Surcharge 100 kPa	2	8.0	0%	100	350	Figure B.2
14	Combined Surcharge 200 kPa	2	8.0	0%	200	350	Figure B.2
15	Parallel Surcharge 100 kPa	3	8.0	0%	100	200	Figure 4.7

5

Results: Analysis of hydraulic gradients

This chapter describes the pressures and hydraulic gradients measured in the physical model using water level gauges and pressure sensors. First, the pressures and hydraulic gradients of the parallel flow configuration tests are shown in section 5.1. Subsequently, these results are shown for the perpendicular and combined flow configuration tests, in section 5.2 and section 5.3, respectively. Finally, the results of the physical model are compared with those of the numerical model in section 5.4.

5.1. Parallel flow configuration

The parallel flow configuration is designed to maximize the parallel flow direction and minimize the perpendicular flow direction. There is a watertight sealing plate placed on compartment B and the initial water level is just above the plate to check watertightness. This setup is schematized in Figure 4.5. An overview of the location of the (normative) pressure sensors and water level gauges is shown in Figure 5.1.

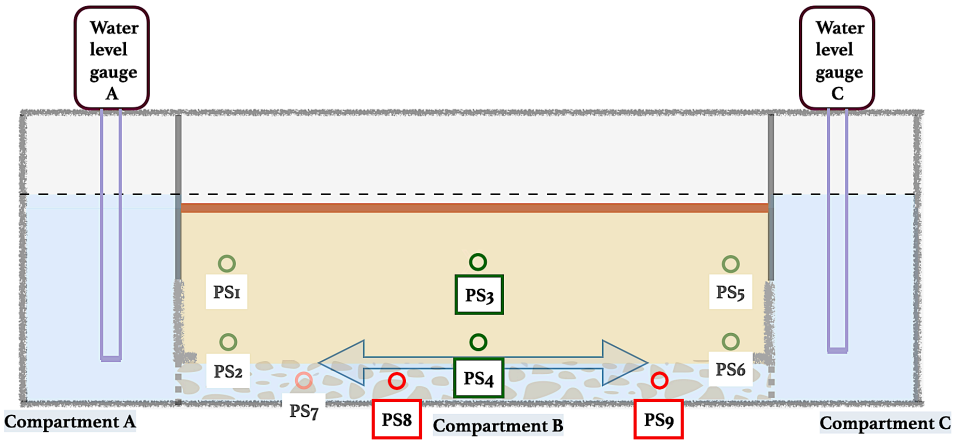

Figure 5.1: Overview locations (normative) pressure sensors and water level gauges.

Figure 5.2(a) shows the pressures over the length of the base-filter interface. The water depth change in compartment A transforms towards the water depth change in compartment C. The black dots in Figure 5.2(a) show the actual measured peaks of the pressures. According to the water level gauges in compartments A and C, the average velocity over the filter was 0.304 m/s. The peaks of the pressures for this constant velocity, according to the position of the pressure sensors, are indicated by the colored dots in Figure 5.2(a).

In Figure 5.2(a) it is observed that the black and colored dots do not overlap, so the movement of the pressure through the filter does not follow a constant velocity. Pressure sensors 7, 8 and 9 are located in the filter material and can be used to obtain the parallel gradient. Between these pressure sensors, a higher hydraulic conductivity occurs than expected. That is based on the steeper slope between the measured peaks (black dots) compared to the average slope (colored dots). This occurs relatively the most between pressure sensors 7-8 and relatively the least between pressure sensors 8-9. Possible reasons

for this are a less well functioning pressure sensor 7 or local disruptions of the base filter interface, caused by e.g. the pressure sensors frame, which can cause local sand penetration in the filter and this could change the cross sectional area for the flow, and therewith flow velocities and gradients.

The difference between the water depths in compartment A and C, divided by the length of compartment B, determines the parallel hydraulic gradient. Another method to calculate the parallel hydraulic gradient is dividing the pressure difference (m water column) by the horizontal distance in the filter material. This is possible between pressure sensors 7 and 8; 7 and 9; 8 and 9. Figure 5.2(b) shows the smallest hydraulic gradient between pressure sensors 7-8, whereas the hydraulic gradient based on pressure sensors 8-9 is maximum and most comparable to the hydraulic gradient based on the water level gauges. This is according to the difference in hydraulic conductivity, based on Figure 5.2(a).

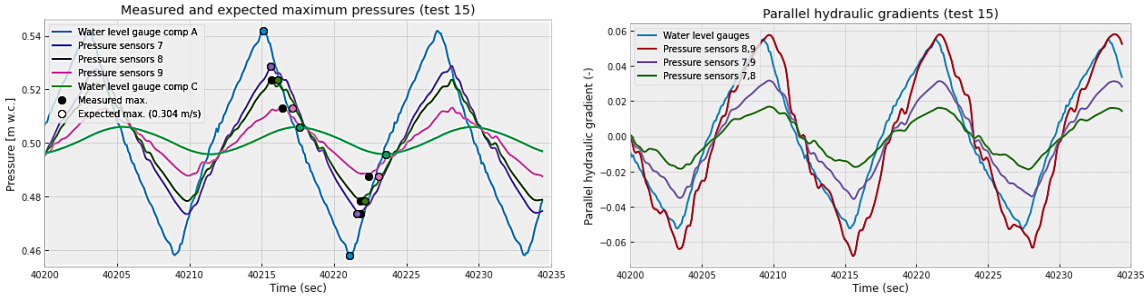

(a) Pressures

(b) Parallel hydraulic gradients

Figure 5.2: (a) Pressures base filter interface, including measured and expected peaks based on constant velocity of 0.304 m/s. (b) Parallel gradients within the parallel flow configuration test.

The initial build-up of the hydraulic gradients with the plunger, plunger program 1, consists of increasing the velocity of the plunger movement at a constant amplitude for all test segments. It turned out that this build-up of hydraulic gradients is suitable for parallel flow configuration tests. The plunger program increases the change in water depth in compartment A and decreases the change in water depth in compartment C. For example, the unfiltered parallel hydraulic gradients during a parallel flow configuration test are shown in Figure 5.3. In all parallel flow configuration tests, the parallel hydraulic gradient increases from around 0.009 to 0.050.

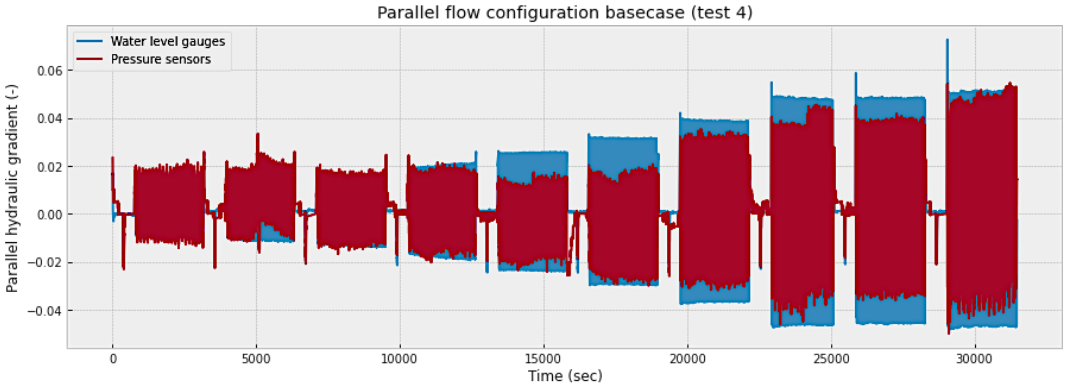

Figure 5.3: Unfiltered parallel hydraulic gradients during parallel flow configuration (test 4).

The parallel hydraulic gradients based on the water level gauges are in good correspondence with the parallel hydraulic gradients between pressure sensors 8 and 9, when no geotextile is placed in front of the filter material (test 15). Otherwise, the parallel hydraulic gradients measured with the pressure sensors are lower. Therefore, the parallel hydraulic gradients are based on the pressure sensors. Pressure sensors 8 and 9 are preferred, because there is no pressure sensor located in between, the distance is relatively large, which increases the accuracy, and these sensors correspond best with the water level gauges.

There are still perpendicular hydraulic gradients present in the parallel flow configuration, due to amplitude differences between the cyclic pressures (Graauw et al., 1984), which is most obvious for the base material with a fines content; see Figure 5.4. The results of the three sets of perpendicular pressure sensors are comparable and the water level gauges overestimate the perpendicular gradient. Pressure sensors 3 and 4 give slightly higher gradients and are centrally located, so used as the normative perpendicular hydraulic gradient. If there is a geotextile in between the filter material and compartments A and C, the perpendicular gradients can be 2 times as large as the parallel gradient. This is further explained below.

The relevant results of all parallel flow configuration tests are shown in Figure 5.4. The averages of the minimum and maximum hydraulic gradients are used, and ”pp” refers to plunger program.

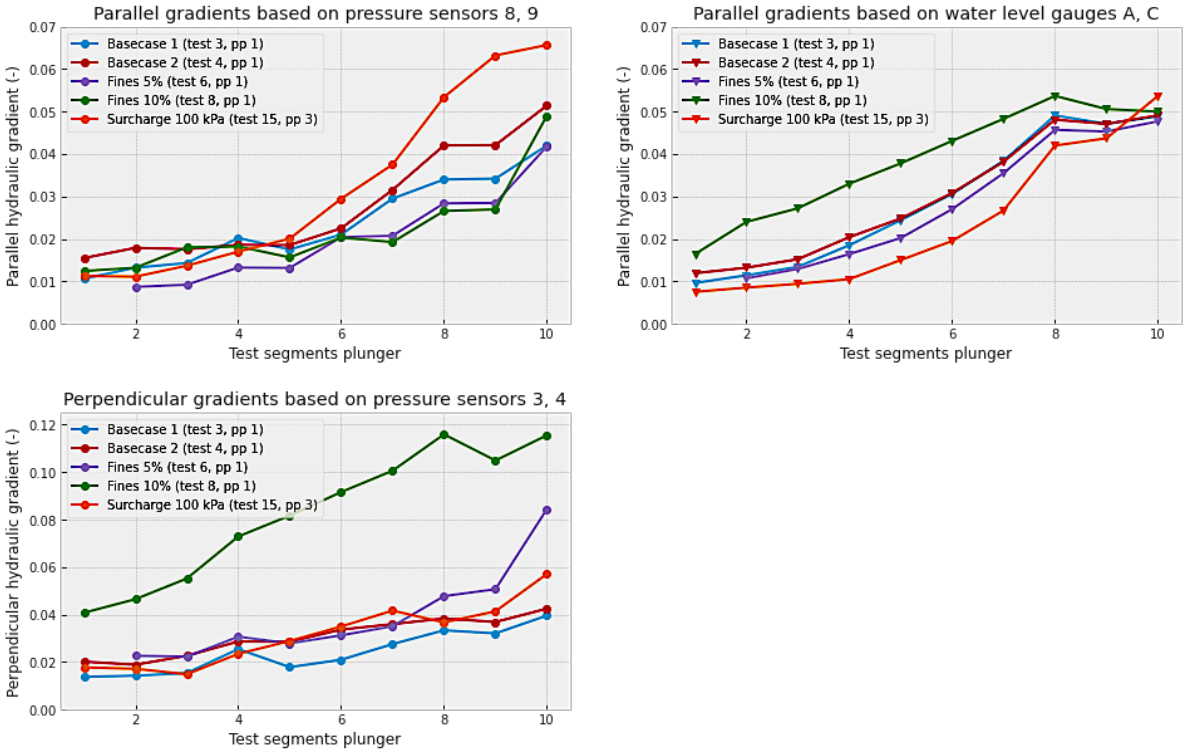

Figure 5.4: Relevant results maximum hydraulic gradients of parallel flow configuration tests. ”pp” means plunger program, specified in Table 4.1.

Geotextile

For practical reasons a geotextile was placed between the filter material and compartments A and C, till test 11. The geotextile avoided erosion towards these compartments, fortunately as this was very time-consuming to remove. After test 10 the wire mesh has been changed, so the geotextile was only located between the sand and compartments A and C, and in such a way that erosion remained limited, see Figure 4.5. Due to this conversion, the hydraulic conductivity changed from 0.02 to 0.2 m/s on the sides of the filter material, according to the hydraulic conductivity test of Figure 2.4. This change has significant influence on the parallel hydraulic gradients determined by the pressure sensors, which are overestimated by the water level gauges in case a geotextile was placed on the sides of the filter material and underestimated in case there was no geotextile. This also becomes clear from the results in Figure 5.4.

The following summary can be made based on the results of the pressures and hydraulic gradients of the parallel flow configuration:

- No constant velocity of the pressures is observed over the length of the filter, Figure 5.2. This corresponds to different magnitudes of parallel hydraulic gradients over the length. Possible reasons for this are a less well functioning pressure sensor 7 or local disruptions of the base filter interface,

caused by e.g. the pressure sensors frame, which can cause local sand penetration in the filter and this could change the cross sectional area for the flow, and therewith flow velocities and gradients.

- Pressure sensors 8 and 9 are used to calculate the parallel hydraulic gradients, because there is no pressure sensor located in between, the distance is relatively big which increases the accuracy, and these sensors correspond best with the water level gauges.
- The perpendicular hydraulic gradients are based on pressure sensors 3 and 4, and its magnitude is at maximum 2 times the parallel hydraulic gradient.

5.2. Perpendicular flow configuration

The perpendicular flow configuration setup is designed to maximize the flow perpendicular to the filter layer. This setup is schematized in Figure 4.6. Figure 5.5(a) shows similar pressures over the length of the filter, so for pressure sensors 7, 8 and 9, and therefore the parallel hydraulic gradients are not taken into account. From the pressure sensors in the base material, so pressure sensors 1-2, 3-4 and 5-6, only pressure sensor 3 measures a smaller pressure range. This smaller pressure range would also be expected for pressure sensors 1 and 5, which are located at the same height as pressure sensor 3, but closer to the side-walls. Possible explanations for the difference could be: inaccuracies of the pressure sensors 1 and 5, or higher hydraulic conductivity close to the walls.

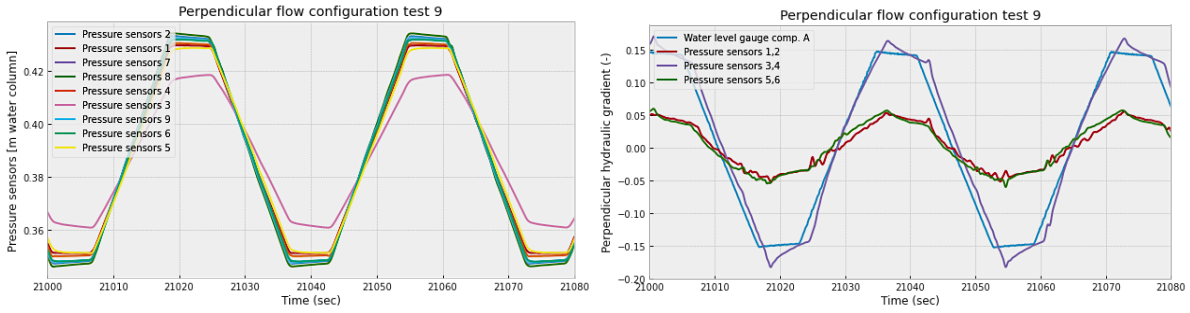

(a) Pressures

(b) Perpendicular hydraulic gradients

Figure 5.5: Measured pressures and hydraulic gradients within perpendicular flow configuration tests.

Perpendicular hydraulic gradients can be calculated with the water level gauge in compartment A, as well as with the pressure sensors in the base material. Higher perpendicular hydraulic gradients are measured in the middle of the filter than close to the sides; see Figure 5.5(b).

In Figure 5.6(a) the hydraulic head and hydraulic gradient distribution are shown for a perpendicular flow configuration with a homogeneous pressure distribution over the length of the filter. In this case, the perpendicular hydraulic gradient is homogeneous in the base material, so no two-dimensional effects occur. This did not appear from the measurements. The possible higher hydraulic conductivity close to the walls has been adjusted in the two-dimensional numerical model and the effects are visualized in Figure 5.6(b). These effects are included by decreasing the pressure difference between compartments A and B over the height of the base material on the sides of the model. These effects could indeed decrease the perpendicular gradient at the sides.

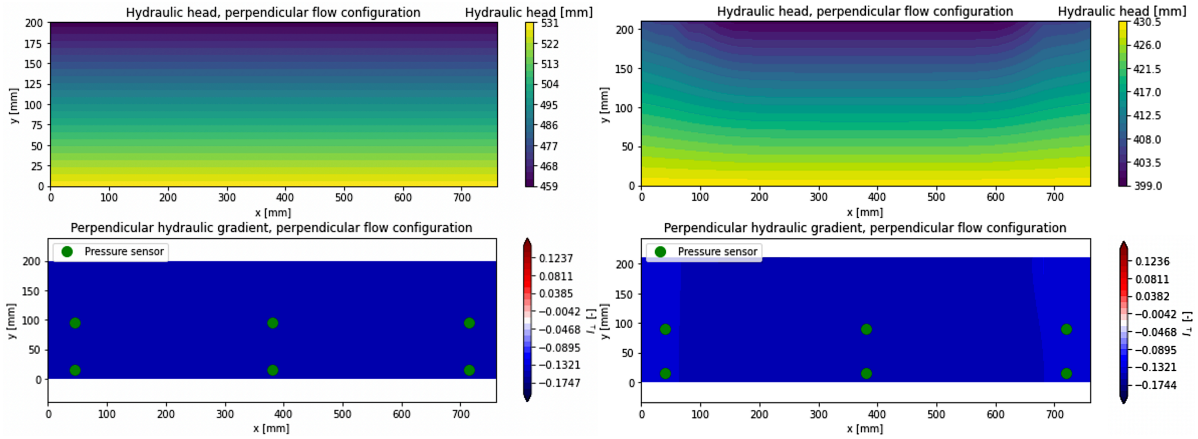

(a) Without decreased pressure difference over height close to the walls. **(b)** With decreased pressure difference over height close to the walls.

Figure 5.6: Distribution of perpendicular hydraulic gradients during perpendicular flow configuration based on two-dimensional numerical model, with and without decreased pressure difference over the height on the sides. The locations of the pressure sensors are indicated by the green dots.

A gradual build-up of the perpendicular hydraulic gradients, consists of increasing the velocity of the plunger movement as well as the amplitude. This plunger program (plunger program 2, see Table 4.1) increases the change in water depth in compartment A during the test. The water depth in the base material (z_B) is based on the water levels at the reference heights before each test segment. The increase in the perpendicular gradient during the perpendicular flow configuration is illustrated in Figure 5.7(a). Perpendicular hydraulic gradients from the water level gauge are based on the assumption that these gradients only take place over the height of the water level in the base material, so Equation 3.4. In this situation, the perpendicular hydraulic gradient increases from 0.10 to 0.25 based on pressure sensors, and from 0.15 to 0.37 based on the water level gauge, which is a big difference. This big difference is the case for all perpendicular tests, so with and without a geotextile between the filter material and compartment A.

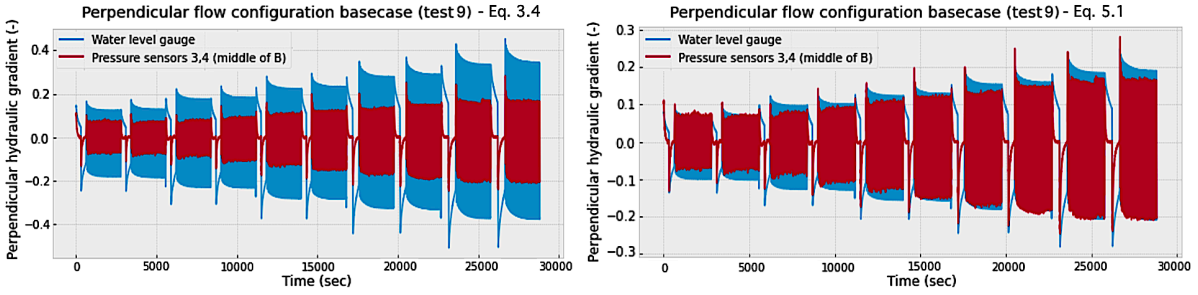

Figure 5.7: Perpendicular hydraulic gradients during perpendicular flow configuration (test 9) without and with the height of the filter material (h_f) taken into account for the water level gauge, corresponding to Equation 3.4 and Equation 5.1 respectively.

As the base material infiltrates and decreases the permeability of the filter material, a possible explanation of the different gradients in Figure 5.7 could be a perpendicular hydraulic gradient over the height of the filter material (h_f) as well. When the height of the filter material is also taken into account as if the filter layer would be base material for 70% of the height, the pressure progression of test 9 is according to Figure 5.7(b) and Equation 5.1. Based on this research, this factor gives the optimal correspondence for the perpendicular tests between the hydraulic gradients of the water level gauges and pressure sensors 3 and 4.

$$i_{\perp}(t) = \frac{z_B(t) - z(t)}{z_B(t) - h_c - 0.3h_f} \tag{5.1}$$

The relevant results of the perpendicular flow configuration tests are shown in Figure 5.8. The perpendicular hydraulic gradients based on the water level gauge in compartment A are only influenced by the amplitude of the water level change in compartment A, and not on the velocity. However, pressure sensors 3 and 4 also shows the influence of the velocity of the water level change in compartment A, which is relevant as well. Furthermore, when fines are added to the base material, the perpendicular gradients based on the pressure sensors are elevated, due to the lower hydraulic conductivity of the fines. This was also observed at the parallel flow configuration, see Figure 5.4. When fines are added to the base (and filter) material, Equation 5.1 gives a too rough estimation of the perpendicular gradients. Therefore, pressure sensors 3 and 4 are used to determine the critical hydraulic gradients.

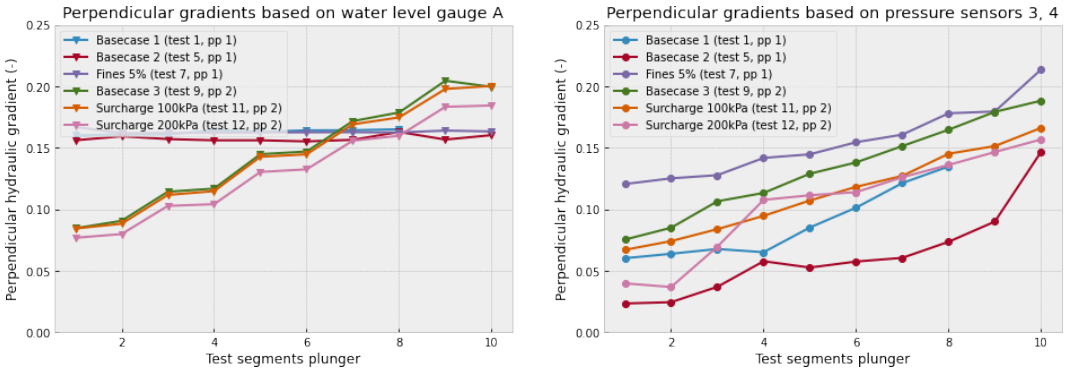

Figure 5.8: Relevant results maximum hydraulic gradients of perpendicular flow configuration tests. ”pp” means plunger program, specified in Table 4.1.

The following summary can be made based on the results of the pressures and hydraulic gradients of the perpendicular flow configuration:

- Low perpendicular hydraulic gradients are measured close to the sides. Possible explanations could be: inaccuracies of the pressure sensors 1 and 5, and higher hydraulic conductivity close to the walls. The second possible mechanism is added to the two-dimensional numerical model in Figure 5.6.
- The height of the water level in the base material and 70% of the filter material gives a more similar approximation of the perpendicular hydraulic gradients based on the water level gauge, in relation to pressure sensors 3-4.
- The results of test 5 are based on pressure sensors 1-2 instead of pressure sensors 3-4, because pressure sensor 3 broke down during the test.
- Increased perpendicular hydraulic gradients are measured with the pressure sensors when fines are added to the base material.
- The increase in gradients when fines are added to the base material is not observed with the water level gauges. Therefore, the gradients measured with pressure sensors 3-4 are used to determine critical hydraulic gradients.

5.3. Combined flow configuration

In the combined flow configuration setup, there are no flow restrictions in the vertical and horizontal directions. This setup is schematized in Figure 4.2. This type of flow configuration is most comparable to a rubble mound structure with a base fill reclamation. Its division between parallel and perpendicular hydraulic gradients is of interest, which also depends on the type of filter and the base material. In this regard, it is recommended to use the hydraulic gradients based on the pressure sensors to avoid inaccurate assumptions.

The plunger was designed to always be partly submerged with sufficient margin during all tests, however, the original built plunger deviated from the design. The original built plunger has had some influence

on the development of the water depths and the hydraulic gradients and this caused the odd behavior of the lower pressures in Figure 5.9(b).

The parallel hydraulic gradient is largely influenced by a geotextile in front of the filter material, and the highest parallel gradients are measured between pressure sensors 8 and 9. This is similar to the parallel flow configuration tests. Therefore, it is decided that the normative parallel hydraulic gradient for the combined flow configuration tests is based on pressure sensors 8 and 9 (I_{89}). The parallel gradient largely increases when the period of water level change in compartment A decreases, as shown in the results in Figure 5.10.

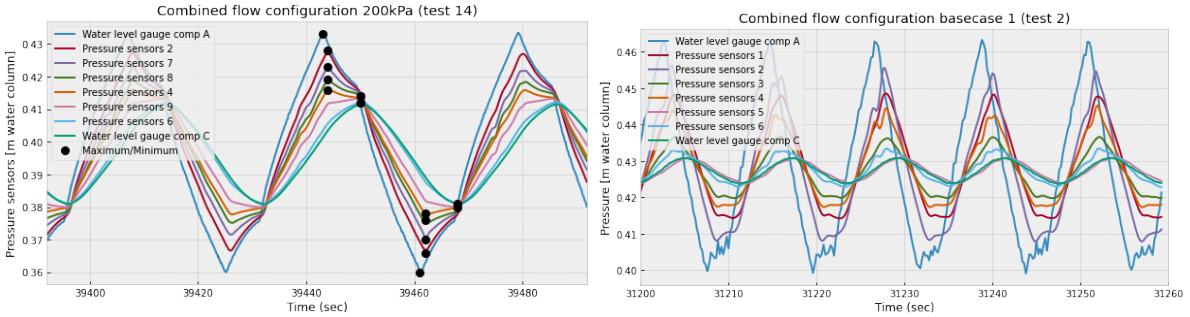

(a) Pressures, incl. waiting time plunger movement

(b) Pressures, excl. waiting time plunger movement

Figure 5.9: Measured pressures combined flow configuration. Change shape of pressures in base material towards sinusoidal.

The perpendicular hydraulic gradient has a positive correlation with the rate of change of the water level in compartment A as well, but only for perpendicular gradients larger than 0.06. More details on this behavior are given in subsection 5.4.1 in combination with the two-dimensional numerical model. This is in correspondence with the change in pressure shape in the base material towards sinusoidal; see Figure 5.9. For the combined flow configuration tests, the perpendicular gradients measured with the pressure sensors are slightly higher in the middle (I_{34}), just as during the parallel and perpendicular flow configuration tests. Since this gradient is also located above the sediment trapping compartments that are used to detect erosion, the normative perpendicular gradient is based on pressure sensors 3 and 4 (I_{34}).

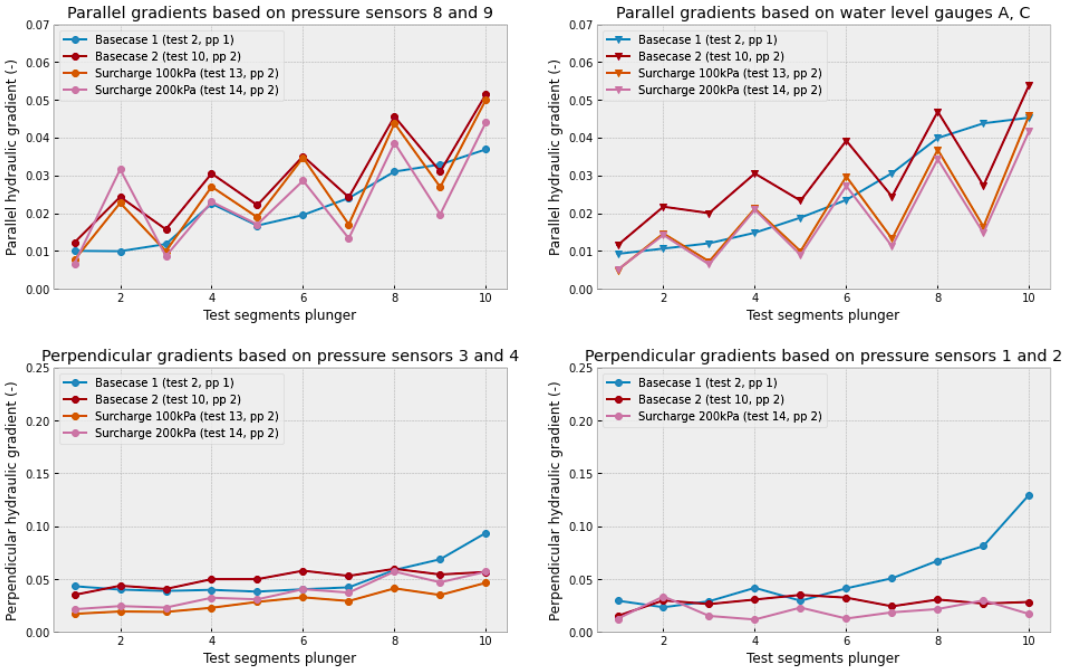

Figure 5.10: Relevant results maximum hydraulic gradients of combined flow configuration tests. ”pp” means plunger program, specified in Table 4.1.

The following summary can be made based on the results of the pressures and hydraulic gradients of the combined flow configuration:

- A geotextile in front of the filter material causes an overestimation of the parallel hydraulic gradients based on the water level gauges and vice versa. Therefore, the normative parallel hydraulic gradient is again based on pressure sensors 8 and 9.
- The perpendicular gradients measured with the pressure sensors are slightly higher in the centre of the filter (I_{34}). The perpendicular hydraulic gradient based on pressure sensors 3 and 4 is the normative hydraulic gradient, just as during the parallel and perpendicular flow configuration tests.
- Based on Figure 5.10, during the combined flow configuration the perpendicular hydraulic gradients do not increase when the rate of change of the water level in compartment A is increased. During all perpendicular flow configuration tests, the perpendicular hydraulic gradients increase during these circumstances. The perpendicular hydraulic gradients starts increasing for perpendicular gradients above 0.06 and this is specified in subsection 5.4.1 with the two-dimensional numerical model.
- All parallel hydraulic gradients during the combined flow configuration do highly increase when the rate of change of the water level in compartment A increases. Therefore, the development of the hydraulic gradient during the combined flow configuration tests is similar to the parallel configuration tests during this research.

5.4. Comparison to numerical models

A comparison between the numerical model and the measured data is given in this section. First, details on the parallel flow configuration are given. Second, an example of the perpendicular flow configuration is shown for the one-dimensional model. Finally, the combined flow configuration in relation to the two-dimensional model is given. The measured and modeled water depth is illustrated in Figure 5.11.

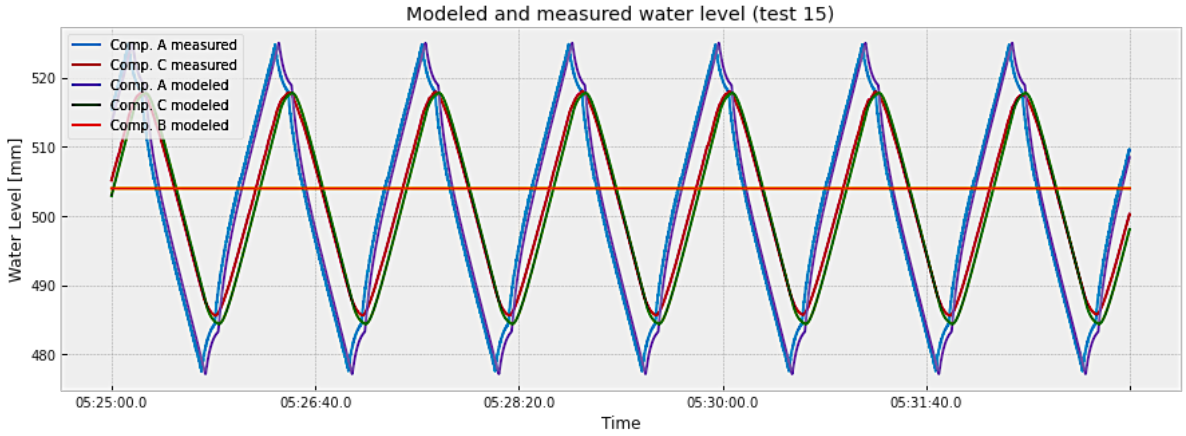

Figure 5.11: Part of measured and modeled water depths.

The increase in parallel gradient during the parallel flow configuration test is shown in Figure 5.12. The instant movement in between the reference heights causes the peaks in hydraulic gradient.

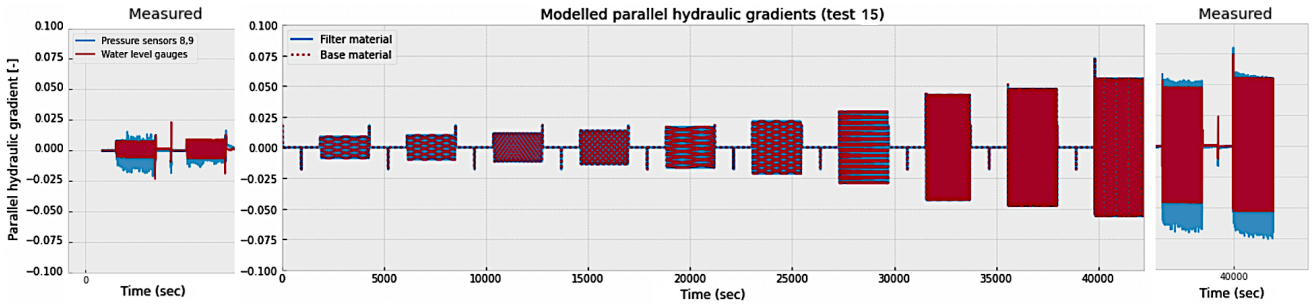

Figure 5.12: Measured and modeled parallel gradients during the parallel flow configuration (test 15).

In Figure 5.13 a close-up of the measured hydraulic gradients according to the water level gauges and pressure sensors is shown, as well as the gradients according to the one-dimensional numerical model. A representative fit occurs with a hydraulic conductivity of the base material (K_s) of 0.583 mm/s and a porosity (n_s) of 0.31. These values correspond very well with the measured characteristics of the base material, (K_s=0.6 mm/s, n_s=0.32) see Table 4.2. Sand behaves according to Darcy's law, so the hydraulic conductivity test of Figure 2.4 can give a good indication.

The hydraulic conductivity (K_f) of the filter material is 155 to 300 mm/s in the numerical model, to give the right fits between the modeled and measured gradients. According to the hydraulic conductivity test of Figure 2.4 a K_f of 0.2 m/s was expected, which was an uncertain estimation because there can be turbulence effects in the filter material, whereas Darcy's law was assumed. The values for K_f deviate a bit, because the base material infiltrates in the filter material during the test which lowers the hydraulic conductivity. A coefficient of quadratic friction (ω_f) of 0.00002 s^2/mm^2 gives the right fit between the modeled an measured hydraulic gradients of Figure 5.13. According to the physical model results, the non-Darcy effect only occurs at the largest parallel gradients, which is above 0.05, so at large filter velocities. This is comparable to the numerical model results where ω_f usually equals 0 s^2/mm^2, unless high parallel gradients occur.

The signal from the water level gauges is very smooth and shows the exact movement as the numerical model. However, both gradients are dependent on the same assumption, so this similarity is not complete evidence of the actual gradients. Pressure sensors can be used more directly to determine the hydraulic gradients. Unfortunately, these signals show many irregularities, as elaborated in Appendix C and Appendix D.

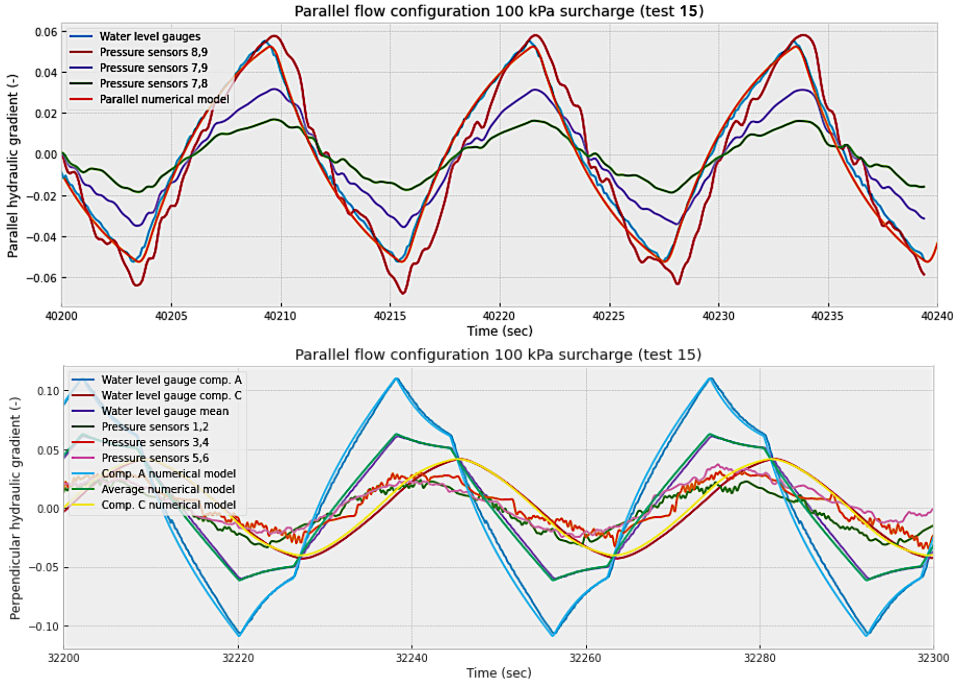

Figure 5.13: Measured and modeled hydraulic gradients from the parallel flow configuration. K_s = 0.58 mm/s, K_f = 0.16 m/s, n_s = 0.321.

Figure 5.14 is an example of a comparison between the one-dimensional numerical model and the measured gradients for the perpendicular flow configuration. The perpendicular hydraulic gradients based on the water level gauge are again more similar to the numerical model, but are both based on the assumption that the water level in the base material is fixed. The difference in calculation of this assumption between Equation 3.4 and Equation 5.1 is also illustrated in Figure 5.14. The perpendicular hydraulic gradients based on pressure sensors 3-4 are most similar to the gradients based on the water level gauge and the numerical model.

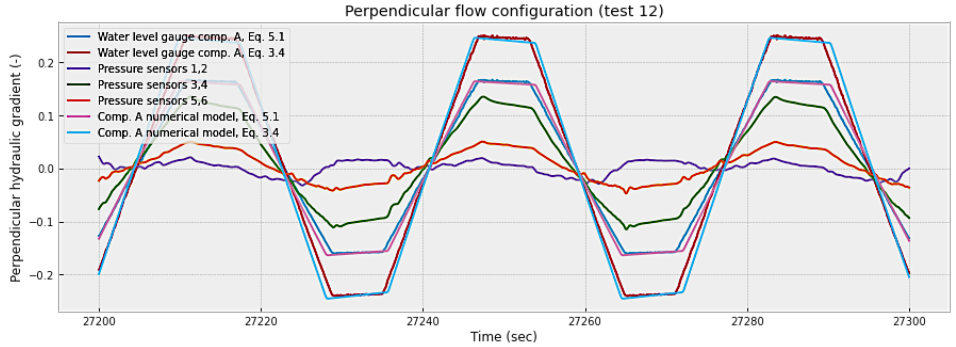

Figure 5.14: Measured and modeled hydraulic gradients from the perpendicular flow configuration. K_s = 0.58 mm/s, n_s = 0.321. The difference between Equation 3.4 and Equation 5.1 is illustrated as well.

5.4.1. Perpendicular gradients in the combined flow configuration

Figure 5.15 shows the perpendicular gradients during the combined flow configuration, according to the pressure sensors and the water level gauges. Remarkable is the change in relative magnitudes of the perpendicular gradients based on the pressure sensors.

At lower test segments, so at perpendicular gradients up to 0.06, pressure sensors 3-4 measure greater gradients than pressure sensors 1-2 and 5-6. At the higher test segments, so at perpendicular gradients larger than 0.06, the perpendicular gradients are greatest close to compartment A (pressure sensors

1-2) and decrease toward compartment C (pressure sensors 5-6). This corresponds to the perpendicular gradients measured with the water level gauges, which are also greater in compartment A than in compartment C. This behavior indicates a change in flow: the flow is mainly parallel for perpendicular gradients until 0.06 and becomes more perpendicular for perpendicular gradients greater than 0.06.

A comparison can be made with a transformation from a situation where the water level in compartment C completely adjusts to the water level change in compartment A towards a situation where the water level changes too fast in compartment A for compartment C to adjust and so the water level in compartment C does not change at all. In this last case, the perpendicular hydraulic gradient based on the water level gauge in compartment A would be maximal, and in compartment C would be zero.

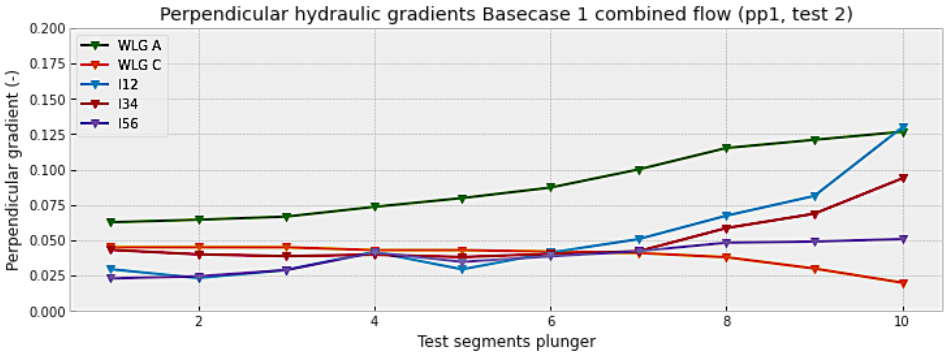

Figure 5.15: Perpendicular hydraulic gradients test 2 (plunger program 1, see Table 4.1).

Figure 5.16 shows the results of the two-dimensional numerical model based on the maximum water depth difference of the oscillation, for both the start and end of the test. The maximum perpendicular hydraulic gradient in the base material cannot be measured, because the pressure sensors measure the average perpendicular gradient over 8 cm. The locations of the pressure sensors are indicated with the green dots in Figure 5.16.

From the two-dimensional numerical model, it becomes clear that the maximum occurring perpendicular gradient is higher than the perpendicular gradient measured with the pressure sensors and that this increase is not constant throughout the test. The maximum perpendicular gradient increases from 1.3 times the perpendicular gradient based on pressure sensors 3-4 (for the start of the test), until 2.2 times the perpendicular gradient based on pressure sensors 3-4 (for the end of the test). This is extremely relevant for the critical perpendicular hydraulic gradient of the combined flow configuration in chapter 6.

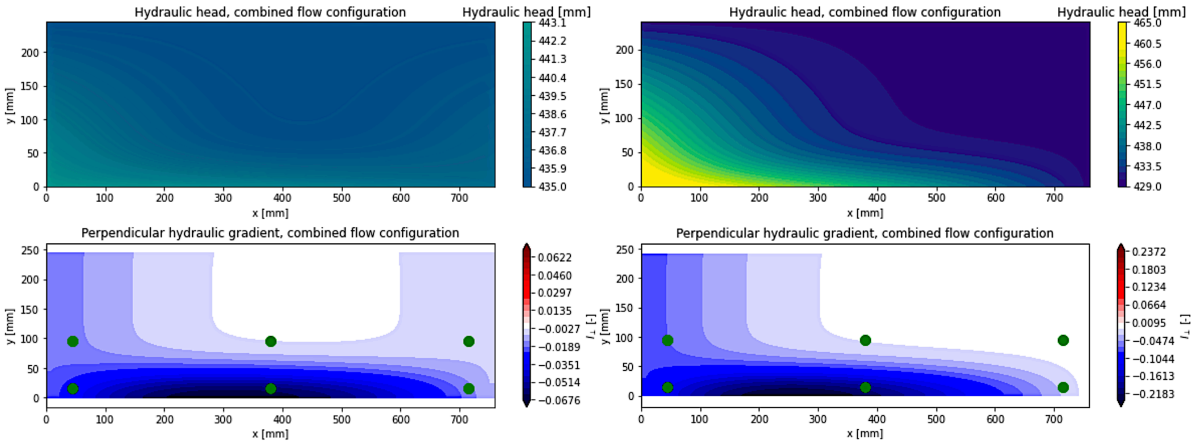

(a) Test segment 1 of test 2.

(b) Test segment 10 of test 2.

Figure 5.16: Maximum perpendicular hydraulic gradients within the base material according to the two-dimensional numerical model results for the combined flow configuration. Green dots at location pressure sensors.

The following conclusions can be made based on the numerical model compared to the measured results:

- There seems to only by a non-Darcy effect visible in the filter material at the largest parallel gradients, so above 0.05, based on the physical model. This is in accordance with the numerical model, where the coefficient of quadratic friction usually equals 0 s^2/mm^2, and a maximum of 0.00002 s^2/mm^2 is estimated.
- There is great correspondence between the hydraulic gradients from the one-dimensional numerical model and those based on the water level gauges, because the water level gauges give very accurate measurement data. They are both based on the same assumption that the water level in the base material is fixed.
- The maximum perpendicular gradient during the combined flow configuration increases from 1.3 times the perpendicular gradient based on pressure sensors 3-4 (for the first test segment) to 2.2 times the perpendicular gradient based on pressure sensors 3-4 (for the last test segment).
- It is decided to persist using pressure sensors for the determination of hydraulic gradients, as for these hydraulic gradients the influence of a fines content and possible geotextile are not ignored.

6

Results: Critical hydraulic gradients

The final results, which are the critical hydraulic gradients, are discussed in this chapter. First, the definition of the critical hydraulic gradient within this research is explained in section 6.1. Then an overview of the critical hydraulic gradients is shown in section 6.2. In section 6.3, the results of this research are shown in relation to future stability. Thereafter, the influence of the fines content is discussed in section 6.4. The results are then compared with the previous results from the research line, based on the Stability Ratio (subsection 6.5.1) and on surcharge (section 6.6). The last section puts the critical hydraulic gradients in perspective.

6.1. Definition critical hydraulic gradient

The critical hydraulic gradient of an open filter is the gradient at which erosion begins to occur. During each test, the gradients increase over 10 test segments. The erosion is determined at the bottom of the physical model, underneath the filter layer. There are six sediment trapping compartments at the bottom. To exclude the influence of wall effects, only the middle four sediment trapping compartments are used for the determination of erosion.

The first start of erosion in the physical model is called the **initial erosion**. Initial erosion is defined as: *The first moment of a noticeable difference in the time-lapse images of the central sediment trapping compartments*. This is the type of erosion that determines the upper limit of the **critical hydraulic gradient**. The lower gradient endured before the upper limit defines the lower limit of the critical hydraulic gradient. This is the same definition of critical hydraulic gradient as for the other researches in the research line. After the initial erosion in a certain sediment trapping compartment, more erosion can occur at higher gradients or no more erosion. If no more erosion occurs afterward, the filter layer has come to a new, more stable situation because it can withstand higher gradients. Erosion that occurs in an instant and then stops, is defined as **incidental erosion**. An example of incidental erosion is shown in Figure 6.1. Incidental erosion is the only type of erosion that occurred in this research and the limit state of the critical gradient. **No ultimate failure** of the filter system occurred during the research.

(a) Before incidental erosion.

(b) After incidental erosion.

Figure 6.1: Example of incidental erosion in sediment trapping compartment 3 during test 4.

Continuously occurring erosion is defined as **transport erosion**, and can be seen as ultimate failure of the filter. During land reclamation projects, transport erosion is also of interest, as at this moment, sand is continuously eroding through the rubble mound structure. Transport erosion within this research is defined as: *The start of continuous noticeable differences in the time-lapse images of the sediment trapping compartments*. Transport erosion did not occur in this research, so (much) higher hydraulic gradients than the maximum measured hydraulic gradients are required for transport erosion.

6.2. Overview critical hydraulic gradients

Table 6.1 gives an overview of the lower and upper limits of the critical hydraulic gradient. Additionally, the maximum measured hydraulic gradient for each test is given. Relevant notes, such as the placement of a geotextile in between the filter material and compartments A and C, are also indicated.

According to the two-dimensional numerical model, the perpendicular hydraulic gradient is not homogeneous over the base material during the combined flow configuration; see Figure 5.16. These maximum perpendicular gradients increase from 1.3 times the perpendicular gradient based on pressure sensors 3-4, till 2.2 times the perpendicular gradient based on pressure sensors 3-4. Therefore, the measured critical perpendicular gradients of the combined flow configuration are adjusted to the maximum perpendicular gradient, according to the two-dimensional numerical model output.

The uncertainty of the perpendicular hydraulic gradient is 0.012 (I_{34}) and that of the parallel hydraulic gradient (I_{89}) is 0.0035. These uncertainties are based on the intrinsic uncertainty of the pressure sensors. The intrinsic uncertainty of the pressure sensors is determined by the maximum fluctuations in pressure output (m w.c.) when no fluctuations are expected, so when measuring atmospheric pressure relative to atmospheric pressure. This fluctuation compared to the distance between the pressure sensors determines the uncertainty of the parallel and perpendicular hydraulic gradient. Details on the calculation of the uncertainty are given in subsection C.2.1. The uncertainty is visualized with error bars around the critical hydraulic gradients.

An overview of all the lower and upper limits of the critical hydraulic gradients is visualized in Figure 6.2. The combined configuration tests show critical parallel gradients most similar to the parallel flow config-

Table 6.1: Results critical and maximum hydraulic gradients per test. Including notes, e.g. if geotextile is placed in between filter material and compartments A and C.

Test	Notes	Geotextile at filter		Critical hydraulic gradient Lower	Upper limit	Maximum gradient measured
1		Yes	$I_{\perp}(-)$	0.060	0.064	0.165
2		Yes	$I_{\perp}(-)$	0.051	0.052	0.279
			$I_{\parallel}(-)$	0.012	0.023	0.045
3		Yes	$I_{\parallel}(-)$	0.014	0.020	0.049
4		Yes	$I_{\parallel}(-)$	0.018	0.019	0.051
5	Pressure sensor 3 broke down	Yes	$I_{\perp}(-)$	0.061	0.074	0.160
6		Yes	$I_{\parallel}(-)$	0.028	0.029	0.048
7		Yes	$I_{\perp}(-)$	0.125	0.128	0.214
8	Turbidity fines	Yes	$I_{\parallel}(-)$	0.027	0.049	0.050
9	White turbidity sediment trapping compartments 1, 3	Yes	$I_{\perp}(-)$		0.075	0.199
10		Yes	$I_{\perp}(-)$	0.046	0.057	0.244
			$I_{\parallel}(-)$	0.012	0.024	0.054
11	Sediment trapping compartment 2 ”tunnel” erosion	No	$I_{\perp}(-)$	0.107	0.118	0.200
12		No	$I_{\perp}(-)$	0.114	0.126	0.184
13	Pressure sensor 2 broke down	No	$I_{\perp}(-)$	0.023	0.030	0.218
			$I_{\parallel}(-)$	0.027	0.035	0.050
14		No	$I_{\perp}(-)$	0.061	0.074	0.155
			$I_{\parallel}(-)$	0.039	0.044	0.044
15		No	$I_{\parallel}(-)$	0.053	0.063	0.066

uration tests. Another remarkable part of Figure 6.2 is the increase in critical hydraulic gradients when fines are added or when a surcharge is applied; this is further elaborated in section 6.4 and section 6.6.

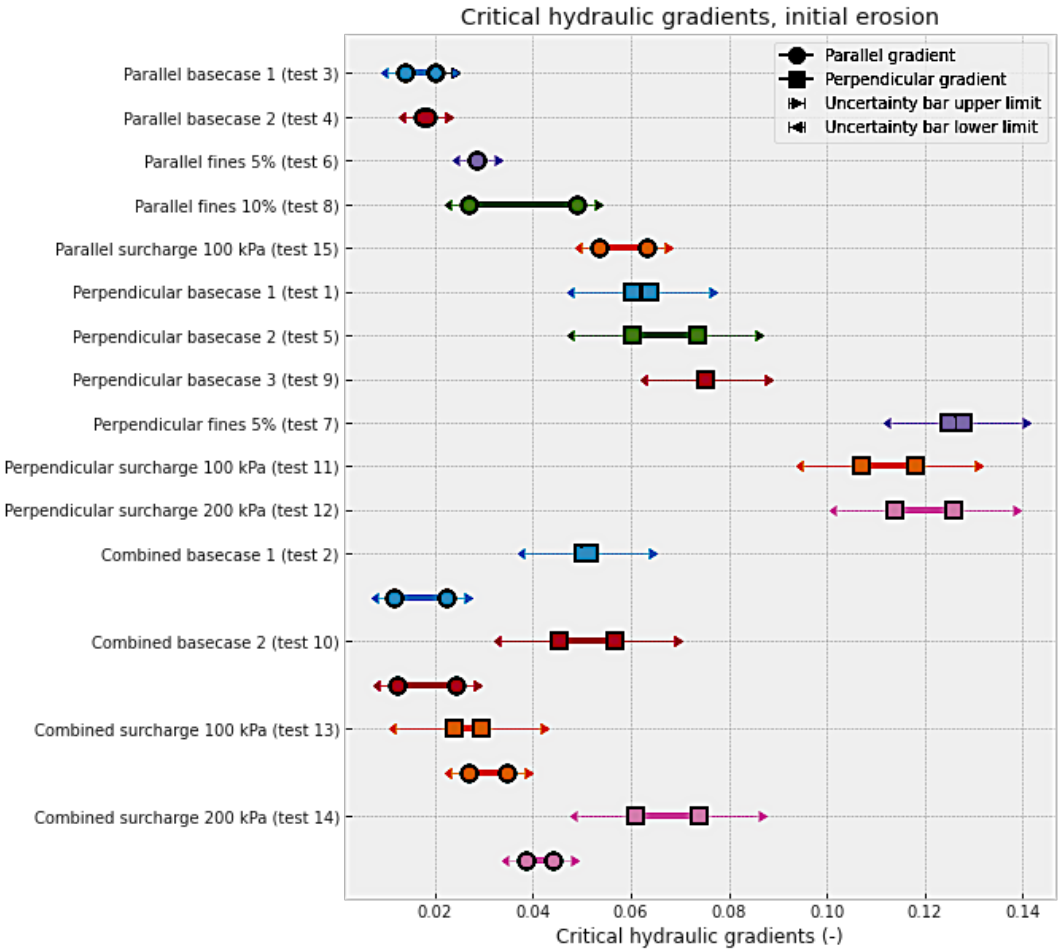

Figure 6.2: Lower and upper limit of the critical hydraulic gradients, including error bars.

6.3. Initial erosion and future stability of the filter

During each physical model test, the hydraulic gradient increases over time through 10 segments. However, when the critical hydraulic gradient in the open inverted filter was reached, this did not necessarily mean that more erosion occurred at higher gradients. Therefore, the filter is able to stabilize itself after initial erosion, which is an interesting characteristic for land reclamations. Figure 6.3 shows the upper and lower limits of the critical hydraulic gradient, as well as the incidental moments of erosion during each base case test. Figure 6.3 indicates that:

- The critical hydraulic gradients are comparable between the base cases per flow configuration.
- When the critical hydraulic gradient has been reached, this does not necessarily imply erosion at higher gradients, and thus the filter can restabilize itself.
- Critical hydraulic gradients during combined flow configuration tests occur when the parallel hydraulic gradient is increased. In addition, incidental erosion occurs during the combined flow configuration as the parallel hydraulic gradient increases.
- Hydraulic gradients that cause transport erosion are not reached.

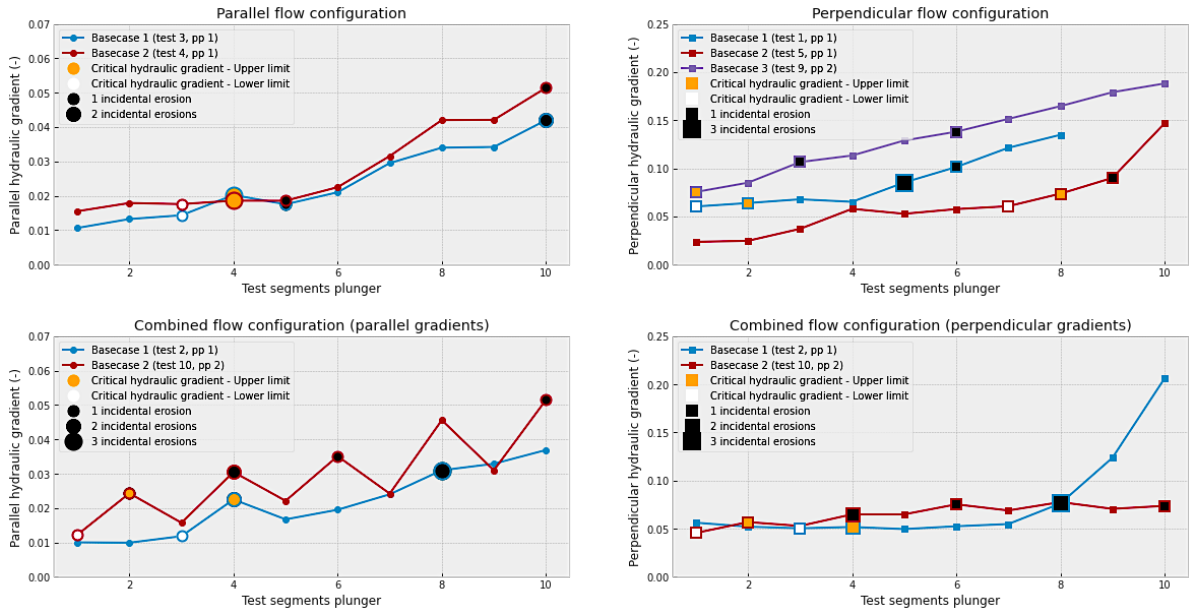

Figure 6.3: Incidental moments of erosion during each base case test.

6.4. Fines content

During this research it is investigated if fines influence the critical hydraulic gradients. Therefore, a fines content of 5% and of 10% were added to the base material during the parallel flow configuration test and a fines content of 5% was applied to the perpendicular flow configuration. The critical hydraulic gradients per fines content for the parallel flow configuration are shown in Figure 6.4. The following influence of fines in the base material on the critical parallel gradients can be observed on the basis of this research:

- A higher fines content gives higher critical parallel hydraulic gradients for the parallel flow configuration.
- A slightly higher increase in the critical parallel hydraulic gradient is observed for a fines content between 5 and 10%, compared to 0 to 5%.
- An increasingly increased critical parallel hydraulic gradient is expected for only low-fines contents. This prediction is based on research by Mitchener et al. (1996), who concluded that the most significant effect on erosion resistance occurs with the addition of small percentages of mud to the sand, within the region of 3% to 15% mud by weight.
- The exact correlation and the influence of a fines content greater than 10% can be determined with further research.

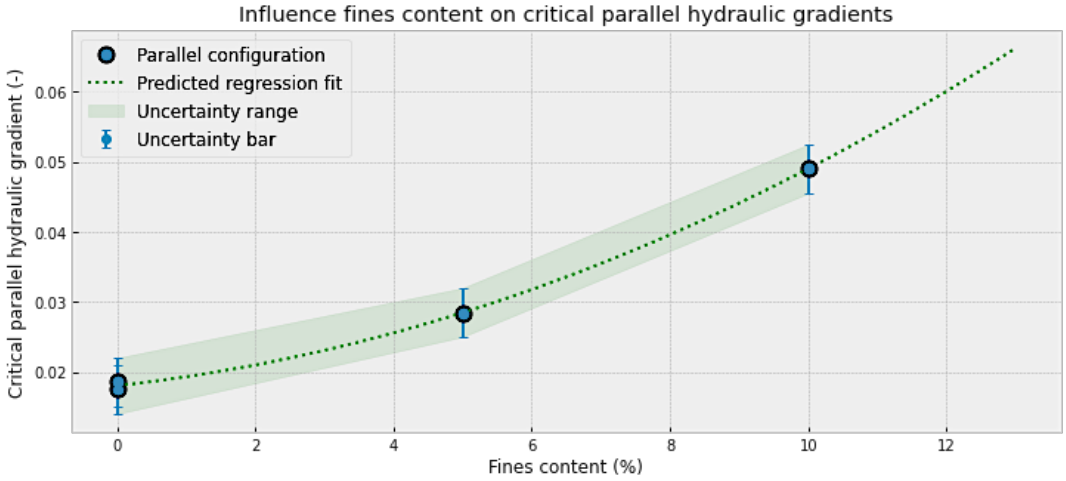

Figure 6.4: Critical parallel hydraulic gradients when fines are added to the base material, including the predicted regression fit.

The effect of fines added to the base material on the critical perpendicular hydraulic gradients is also investigated. Figure 6.5(a) shows these gradients in relation to the fines content for the perpendicular flow configuration. Figure 6.5(b) shows the perpendicular hydraulic gradients during tests 1 and 7, based on the pressure sensors, as well as on the water level gauge. The following results are found:

- A higher fines content gives higher critical perpendicular hydraulic gradients.
- The fines content significantly alters the hydraulic perpendicular gradients in the base material. This becomes clear from Figure 6.5(b), where all perpendicular hydraulic gradients based on pressure sensors are higher when 5% fines are added (purple line). The gradients based on the water level gauge are the same between the two tests (green and red lines), indicating equal changes in water level in compartment A. This result was already expected from the measured difference in hydraulic conductivity.
- The positive influence of a fines content on the critical perpendicular hydraulic gradient is expected to equalize for higher fines contents, because the hydraulic conductivity reduces less for higher fines contents. The permeability becomes extremely low for fines contents greater than 30%, see Figure 2.6(b).
- It is very important to realize that the increase in critical perpendicular hydraulic gradient is only caused by the difference in hydraulic conductivity and not by an increase in strength of the base material to resist external eroding forces. This should be taken into account when the design of a base fill retaining rubble mound structure is only based on the wave climate, instead of on the hydraulic resistance of the soil as well.
- The exact correlation and the influence of fines contents higher than 5%, can be determined with further research.

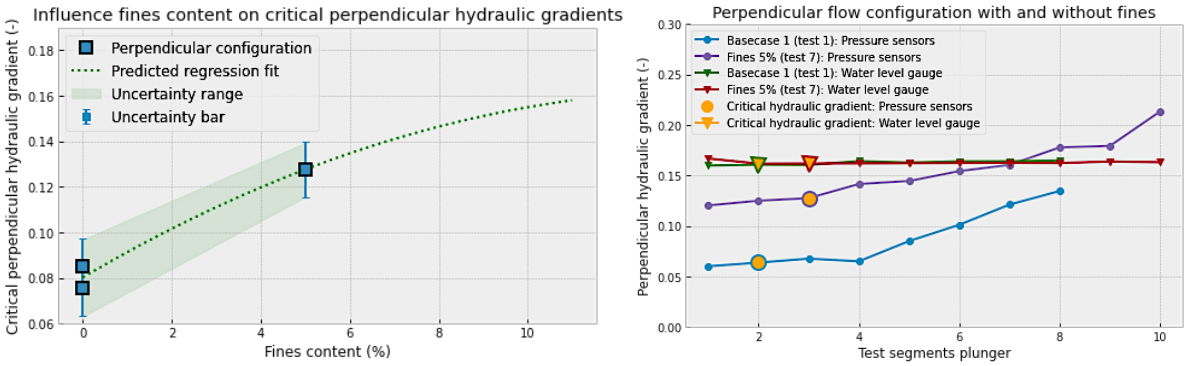

(a) Critical perpendicular hydraulic gradients.

(b) Perpendicular hydraulic gradients during tests.

Figure 6.5: Critical perpendicular hydraulic gradients with fines added to the base material.

6.5. Coefficient of uniformity

During the research line, the influence of the Stability Ratio (SR = $\frac{d_{15f}}{d_{85b}}$) has been investigated by physical modeling. This section compares the results of this research with the previous results in the research line. Dredged sand for land reclamation projects usually has a coefficient of uniformity greater than 2.0, according to Table A.1. In this research, wider graded sand (C_u = 2.9) was used as the base material compared to previous research in which narrower graded sand was used (C_u of 1.2-2.1).

6.5.1. Stability Ratio

The primary strength of the filter is the Stability Ratio. A Stability Ratio greater than 5 is considered an open filter (Schiereck & Verhagen, 2019, pp. 131–132). The Stability Ratio in this research is 8.0 and the lower and upper limits of initial erosion have been added to the other critical hydraulic gradients of the research line, see Figure 6.6. The definition of critical hydraulic gradient is the same for the entire research line.

The following observations and explanations can be made about Figure 6.6:

- The critical hydraulic gradients measured in this research, are similar to those in the research line.
- The critical parallel and perpendicular hydraulic gradients are most comparable to those measured by Van de Ven (2019). Van de Ven (2019) used sand with a coefficient of uniformity (C_u) of 2.1 at a Stability Ratio of 8.0, which is most comparable to the uniformity of the sand combination of this research with a C_u of 2.9.
- The critical parallel hydraulic gradients are high compared to the results of Lengkeek (2022), however, in those tests, leakage occurred.
- The critical perpendicular hydraulic gradients are low compared to the results of Lengkeek (2022), which could be explained by the difference in the coefficient of uniformity. The greater variation in grain sizes could disturb the formation of arches, which would lower the critical perpendicular gradient. Another explanation is that the more graded base material can have finer sand fractions that are not internally stable and are easier to fluidize, and thus easily lost through the filter material.

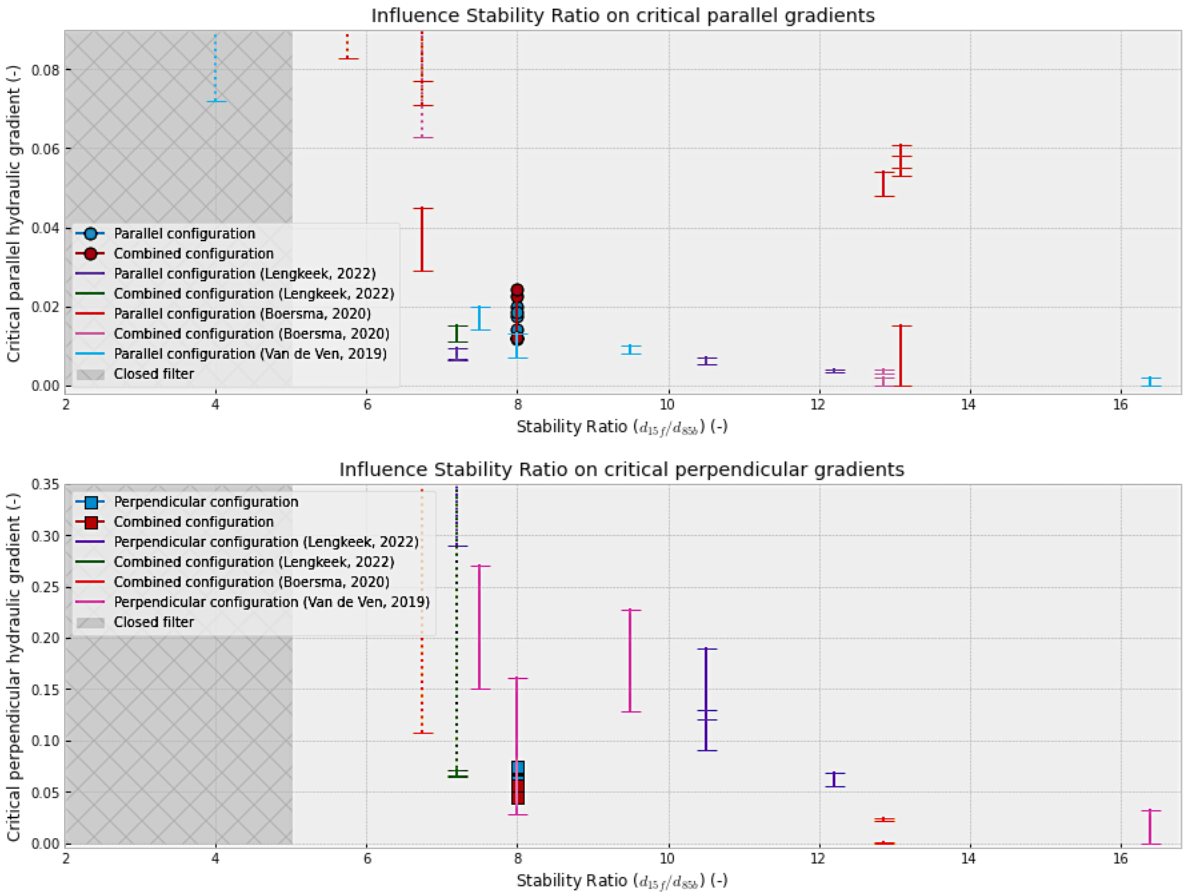

Figure 6.6: Upper and lower limits of the critical parallel and perpendicular hydraulic gradients compared to the Stability Ratio.

6.6. Surcharge

Friction between particles increases when effective stress is applied. Therefore, the influence of a surcharge on the critical hydraulic gradient has been researched for the parallel, perpendicular, and combined flow configuration. The results are combined with the results of Lengkeek (2022).

The surcharge applied to the granular filter in a rubble mound structure increases when a larger layer of sand is retained. The rubble mound structure from Figure 6.7 is used as an example to calculate the surcharge on the granular filter. When the soil exerts the minimum horizontal stress, the soil is in active condition according to (Rajapakse, 2016). Soil particles have room to move in a base fill retaining rubble mound structure. The coefficient depends on the effective friction angle of the soil (ϕ of 36° is assumed). Based on Equation 6.1, the coefficient of active lateral earth pressure (K_a) is 72%, which can be seen as the part of the vertical effective stress working on the granular filter.

$$K_a = (1 - tan(45 - \phi/2)^2) \quad \sigma_h = K_a \cdot \sigma' \tag{6.1}$$

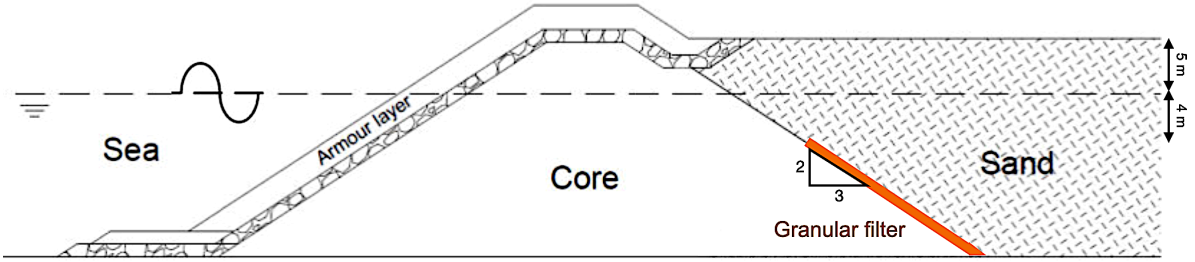

Figure 6.7: Sketch of an example of a base fill retaining rubble mound structure including a granular filter.

The dry sand combination has a density of 1578 kg/m^3 and the saturated sand combination is around 1979 kg/m^3. The effective stress for different heights of the sand fill is shown in Figure 6.8.

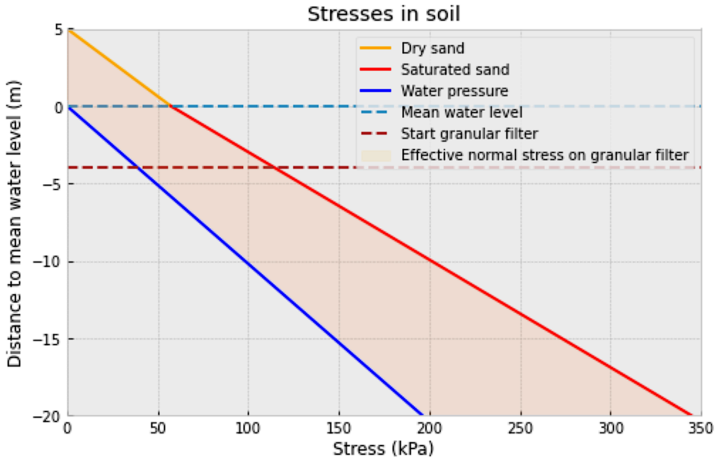

Figure 6.8: Soil stresses over the depth of the sand fill, including the effective stress.

The relative critical perpendicular hydraulic gradients are visualized in Figure 6.9. It is important that the relative increase in critical gradients is calculated per Stability Ratio, to give a fair comparison. Furthermore, only the upper limits of the critical gradients are taken into account, since the relative results to a lower limit value can be highly uncertain. Therefore, the results of this research are shown with SR=8.0, as well as the results of Lengkeek (2022) for SR=12.2. The graph indicates that:

- A surcharge increases the critical perpendicular hydraulic gradient. This can be explained by the increase in strength of the arches as a result of the higher effective stress. The base-filter interface is stabilized by arching at the base-filter material.
- The results are similar between this research and the research of Lengkeek (2022).
- A much larger increase is observed between 0 and 100 kPa, compared to 100 to 200 kPa. This corresponds to the research on open filters from Graauw et al. (1984), who concluded that for larger superimposed loads, the critical perpendicular gradient increases less; see Figure 2.13.
- The exact correlation can be determined with further research.

Figure 6.10 shows the critical hydraulic gradients for the parallel flow configuration and for the combined flow configuration, for different superimposed loads. The following observations are made on this graph:

- Figure 6.10(a): When a surcharge is applied to the parallel flow configuration test, the filter can withstand higher hydraulic gradients.
- Because the critical parallel hydraulic gradient depends mainly on the shear velocity of the filter layer on the base material, stronger arches will have a less positive impact. However, the compaction of the base and filter material is a side effect of the superimposed load. Compaction improves filter characteristics and has a positive impact on the critical parallel hydraulic gradient.

- Figure 6.10(b): The combined flow configuration tests show an increase in critical parallel gradients when a surcharge is applied, but not for the critical perpendicular gradients. It seems like the combined flow configuration depends mainly on the critical parallel hydraulic gradient in this research.
- Based on the tests performed, the parallel configuration tests show a greater positive relationship with surcharge than the combined configuration tests. During the physical model tests, where the top of compartment B was completely sealed, the compaction was larger compared to the combined flow configuration test. This may possibly explain the difference in the critical parallel gradient.
- Further research could quantify the impact of a surcharge on the parallel and combined flow configuration.

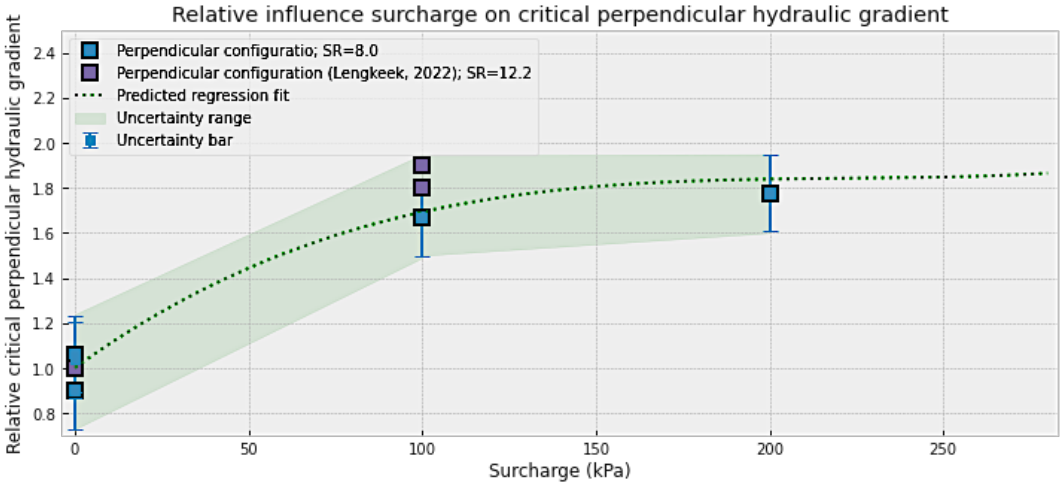

Figure 6.9: Relative critical perpendicular hydraulic gradients compared to the surcharge applied on the base filter interface.

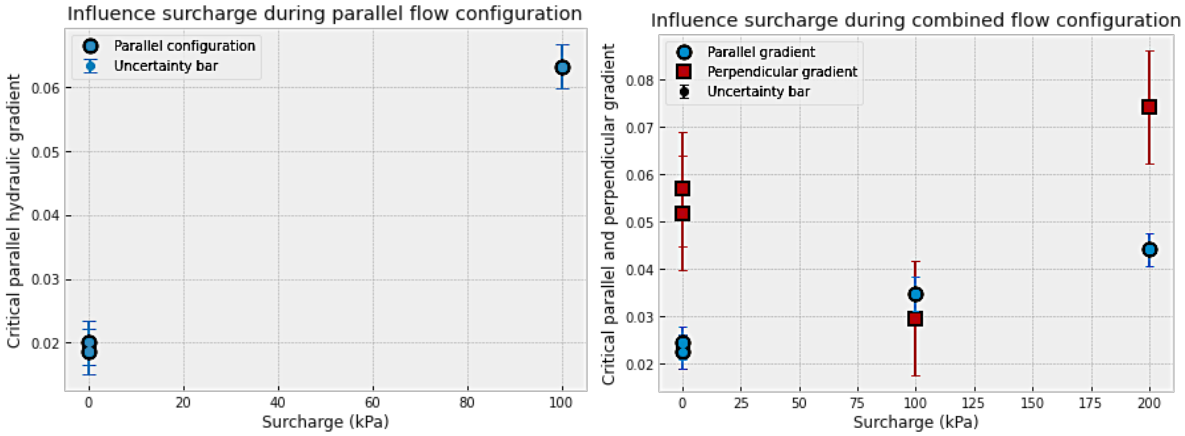

(a) Parallel flow configuration.

(b) Combined flow configuration.

Figure 6.10: Critical hydraulic gradients compared to the surcharge applied on the base filter interface.

6.7. Critical hydraulic gradients into perspective

To put the obtained critical hydraulic gradients into perspective, the results are compared to the estimated hydraulic gradients occurring in a rubble mound structure. Van de Ven (2019) used the OpenFOAM numerical model, to estimate the pressures that occur at the interface of a land reclamation and a rubble mound structure. It should be noted that this model has not been scientifically verified.

Figure 6.11 shows the parallel hydraulic gradients in the left graphs, and the perpendicular hydraulic gradients in the right graphs. The results of the parallel and perpendicular flow configurations are shown in the upper graphs, while the results of the combined flow configuration are shown in the lower graphs. The y-axis shows the height with respect to the mean water level, and the x-axis shows the hydraulic gradient. The 2% highest parallel gradients based on the OpenFOAM model are marked with dots, and the 2% highest perpendicular gradients with squares.

According to the OpenFOAM model, all parallel and combined flow configuration tests form a stable system based on the parallel gradients. For the entire filter, the parallel hydraulic gradients in the case study are lower than the measured critical parallel gradients, indicating a hydraulically closed filter.

The perpendicular gradients obtained from the case study are higher than the critical perpendicular gradients along the entire filter layer. This means that the sand combination and Stability Ratio of the physical model would never give a stable situation in the case study.

Based on the OpenFOAM model, the perpendicular gradients are governing for the erosion for the combined flow configuration. However, it is only governing for this particular case, because the ratio between the gradients is influenced by the geometry of the rubble mound structure cross sections.

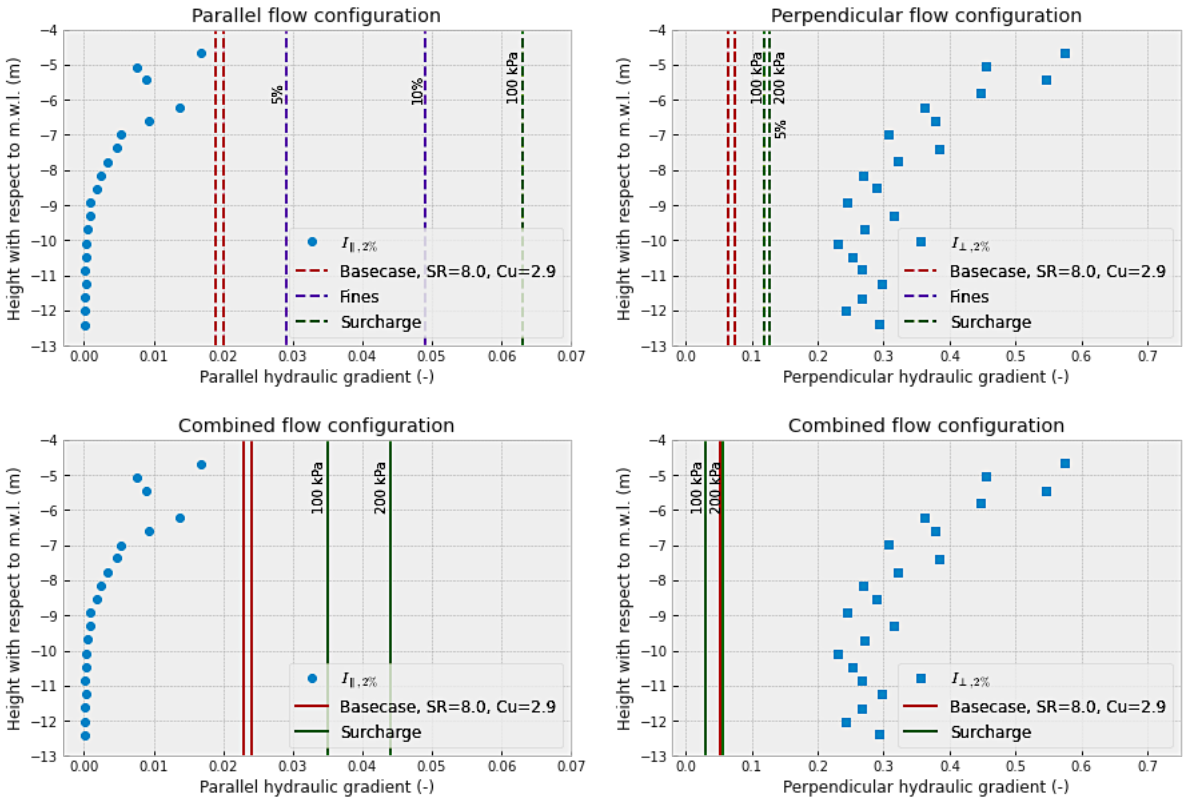

Figure 6.11: The critical parallel and perpendicular hydraulic gradients of all flow configurations determined with the physical model. Values compared to the gradient occurring in a rubble mound structure estimated in OpenFOAM by Van de Ven (2019).

7

Discussion

Within this chapter, the uncertainties of the physical and numerical models are discussed, respectively, in section 7.1 and section 7.2. These models are a simplified representation of reality. A discussion is given on the interpretation of the results in section 7.3. Comparisons are made between the current research and previous research.

7.1. Physical model

Even though the physical model is enlarged in size compared to previous research by Boersma (2020), boundary effects still influence the test results. The same setup has been used as in the previous research from Lengkeek (2022), with various adjustments as described in section 4.5. Nevertheless, uncertainties are still present, and these uncertainties are discussed in this section.

7.1.1. Pressure sensors

The reliability of the calibration of the pressure sensors (”26PCAFA6D”, see Appendix A) is discussed in Appendix C. During a period of 3.5 weeks, the measuring range (α-factor in the calibration formula) of most pressure sensors varied on the order of a few percent, as detailed in Table C.2. In addition, voltage changes of up to 6.3% are also present from the pressure sensors, ascertained by the ”air-to-air” test, as specified in Table C.1. The uncertainty of the pressure sensors based on the ”air-to-air” test are taken into consideration for the uncertainty of the critical hydraulic gradients.

The discussion points concerning the pressure sensors are the potential impact of sand grains on the sensor’s membrane. Sand clogging occurred (at least) twice during the research; however, glass sand grains are not visible. Despite this, no complete functionality impairment was observed due to sand clogging. Protective soil membranes in front of the sensor membrane, that allow water permeation only, could exclude this risk.

Additionally, the stiff air tubes connected to the relative pressure sensors are not transparent, preventing visual identification of moist or grains within the tubes. An air bubble in front of the measuring membrane could influence the detection of vibrating pressures. This risk can be avoided by introducing silicon oil in front of the membrane. Note that this risk is irrelevant for long measurement periods. Furthermore, fluctuations in sensor and amplifier temperature affect the sensor outputs. However, a precautionary measure to ensure that the sensors and amplifiers are powered for at least an hour before starting the tests, coupled with temperature-compensated pressure sensors, mitigates this influence. The discussion points on the pressure sensors mentioned in this subsection can be helpful for further research where pressure sensors are used within the soil.

7.1.2. Plunger mechanism

The velocity range of the plunger motion is restricted to 5 to 35 mm/s, while the maximum acceleration is set at 100 mm/s^2. It is important to note that when the plunger’s movement approaches the limits of the velocity and acceleration, considerable vibrations occur. These vibrations disrupt the functioning of the filter system. Consequently, the waiting intervals in the plunger program for the two shortest loading periods (24 and 12 seconds) are reduced to 2 seconds and no waiting time, respectively. During this research no transport erosion occurred, so if more extreme types of erosion than incidental erosion are of interest, greater parallel gradients than 0.066 and perpendicular gradients than 0.22 are advised.

7.1.3. Surcharge tests

Test 9 till 15 were conducted in the Construction Laboratory of Delft University of Technology, in contrast to other tests that took place in the Hydraulic Engineering Laboratory. The surcharge used in certain tests is calibrated regularly by laboratory technicians. Although the climate variance between the locations will be minimal, two different locations potentially contribute to the reliability of the tests.

The process of elevating the test configuration by 80 cm with a pallet truck, to put it underneath the surcharge, induces vibrations within the filter system. Regrettably, this action increased the initial erosion of the sand through the filter medium and decreased the functioning of the filter. This occurred during test 11 above sediment trapping compartment 2, so this sediment trapping compartment was not taken into account.

7.1.4. Leakage

Leakage of the setup primary emanated from the bottom. This issue was particularly pronounced during the attempts to investigate an inclined filter, leading to the failure of the test. Without the use of sealant, complete isolation of compartment C during perpendicular flow configuration tests was challenging, but the amount of flow was insignificant. When sealant could be used, there was no flow at all to and from compartment C.

Furthermore, a 200 kPa parallel flow configuration test failed due to the impact of the surcharge, which caused the rigid sealant in the sediment trapping compartments and the bottom of the setup to break. Although the leakage in the sediment trapping compartments was repaired with Permacol 3000 glue, unfortunately the bottom of the setup could not be remedied similarly. In parallel flow configuration tests, considerable effort was invested to prevent air pockets under the sealant plate and ensure the watertightness of compartment B throughout the test. However, a complete guarantee of this aspect, especially in the parallel flow configuration test in combination with a surcharge (tests 15), remained elusive, particularly due to the challenges with the top plate. Aqua blocker is recommended for making the sealant plate watertight, as it dries in a couple of hours, can be applied on a wet surface and can be easily removed for further tests.

7.1.5. Turbidity

The evaluation of erosion within the sediment trapping compartments encountered disruptions during some of the tests, attributable to factors such as dust that originated from the base material, washed out silt, or the flocculation of white corrosion from the setup. Postponing the test for one day allowed the turbidity to settle. However, a perpendicular flow configuration test with 10% fines failed because the turbidity persisted despite the delay. The white flocculate of the white corrosion looked similar to that of sand grains, introducing further ambiguity. Employing company water, instead of tap water which contains more oxygen, and treating metal surfaces with ammonia did not solve the problem. In an attempt to accelerate the settling process, 100 ml of flocculant was dissolved in the water of the sediment trapping compartments during test 15. However, this strategy did not have an influence.

7.1.6. Permeability and porosity

The determination of the permeability of the base and filter material presents a challenge. Permeability has been assessed with a constant head permeability test; see Figure 2.4. The subsequent calculation is according to Darcy's law; see Equation 2.4, so laminar flow is assumed which is not valid for gravel (Re_{max}=30). An alternative approach involves the utilization of empirical formulas, of which a multitude have evolved over time. These results are shown in Table 4.2. A third method to determine the permeability of the soil is by fitting the numerical model, capable of accounting for non-Darcy effect.

In addition to the challenge of accurately determining the permeability of the base and filter material, there are limitations within the physical model that influence the porosity and permeability and consequently the hydraulic gradient. First, the particle size distributions of soils are based on several samples, and achieving a homogeneous mixture of the combination of sand (and silt) is challenging. Second, the walls of compartment B can increase the porosity. Remediation efforts involve using wire mesh, bubble wrap and excluding the outer sediment trapping compartments. Approximately 15 mm of the front and back sides of the other sediment trapping compartments are not taken into account for erosion detection either.

Until test 10, a geotextile was placed between the filter material and compartments A and C. This prevented erosion of the sand in these compartments, which took a long time to remove. However, the permeability assessments according to Figure 2.4 indicate that the intrinsic permeability of the filter material is 0.2 m/s, while the intrinsic permeability of the filter material after the test has been performed that includes two layers of geotextile can reduce till 0.02 m/s.

The filter system comprises nine pressure sensors, each having dimensions of 10x11x40 mm, each connected to a cable and an air tube and all attached to the frame shown in Figure A.8. Although the dimensions of the pressure sensor resins are as small as possible, this sensor-equipped frame certainly influences the porosity and, thereby, the internal flow dynamics of the filter system. If pressure sensors are not required to have a general shape in terms of reuse, customized resins that mimic the base or filter material are preferred. This adaption is likely to result in a more impeded flow around the pressure sensors, leading to larger pressure differences between the perpendicular pressure sensors and thus increasing the hydraulic gradient.

Another consideration is that the interface between the filter and the base material is not very evident during testing. This implies that the pressure sensors for the parallel hydraulic gradient become partly surrounded by base material during the test. On the contrary, the lower pressure sensors in the base material to determine the perpendicular hydraulic gradient might be positioned too close to the filter material.

7.2. Numerical model

The numerical model can be used to calculate the flow between compartments. By specifying the characteristics of the base and filter material, the hydraulic gradients can be estimated. Relevant implications are discussed below.

7.2.1. Non-linear effects

Where as the flow through the base material follows Darcy's law, this is not necessarily the case for gravel. Based on the physical model, there seems to only by a non-Darcy effect visible at the largest parallel gradients, so above 0.05. This is in accordance with the numerical model, where the coefficient of quadratic friction usually equals 0 s^2/mm^2, and a maximum of 0.00002 s^2/mm^2 is estimated. This indicates that within the filter material, some turbulent effects can occur. The Reynolds number of the base material is around 0.16, and for the filter material 30 at maximum, whereas laminar flow has a Reynolds number below 10.

7.2.2. Potential flow approach

The two-dimensional numerical model uses the potential-flow approach with the LaPlace equation. This assumption is valid for laminar resistance and therefore for the base material, but not entirely for the filter material. According to the physical model measurements, non-linear effects can occur at the highest parallel gradients.

Effects close to the walls

According to the measurements of the physical model, the pressure difference between the pressure sensors in the base material close to the wire mesh at the walls of compartments A and C (pressure sensors 1-2, and 5-6) is less than in the middle (pressure sensors 3-4). These effects closer to the wall are taken into account in the two-dimensional numerical model by decreasing the total pressure difference between compartment B and compartment A (and C) over the height of the base material, close to the sides of the base material. An estimation of these wall effects is shown in Figure 5.6. However, when more measurement data would be available in this region, these effects could be added more precisely.

7.3. Interpretation of the results

Analyzing the results from the research, arose discussion points, of which the three most important ones are discussed below.

7.3.1. Failure of the base filter interface

In the research line, the failure of the base filter interface is based on initial erosion, so this type of erosion defines the critical gradients, as further explained in section 6.1. This results in a situation where *incidental* erosion defines failure of the filter, and not *transport* erosion. This is debatable, because moments of small erosion losses would be acceptable in practice. The purpose of the land reclamation, its lifespan and the length of the open inverted filter will determine this. Furthermore, the higher gradients required for transport erosion, could cause more dependence on perpendicular gradients during combined flow instead of parallel gradients. However, no transport erosion was observed during the research.

Based on erosion during the tests, visualized for the base cases in Figure 6.3, the critical hydraulic gradient does not necessarily imply erosion at every higher gradient. This indicates that the base-filter interface can reform to a more stable configuration that can withstand higher gradients. This corresponds to the hypothesis and literature study that, based on the strength of the base fill such as the failure angle and negative pore pressures, collapses from the arches can occur without the *ultimate* critical hydraulic gradient being reached (Bratli & Risnes, 1981). When part of the base material particles have found a new, more favorable position, the movement can stop. This implies that the geometrically open granular filter could withstand higher critical hydraulic gradients than it seems from the initial erosion.

7.3.2. Influence of hydraulic conductivity on critical gradients

The investigation of the influence of fines on the critical gradients revealed the great influence of the hydraulic conductivity on the perpendicular gradients, as can be seen in Figure 6.5. This influences the interpretation of the critical hydraulic gradient, and therefore the same comparison is made between the results of the Stability Ratio. The hydraulic conductivity (K) of the sand in this research is 0.6 mm/s according to the permeability test described by Equation 2.4. The sand used by Lengkeek (2022) for SR=10.5 could be traced, and a hydraulic conductivity of 0.4 mm/s has been measured for this sand. A lower hydraulic conductivity increases the perpendicular hydraulic gradients under the same forcing conditions from the plunger. In the case that finer sand is used to obtain higher Stability Ratios, this means that the difference in the strength of the base material could be larger between the different Stability Ratios than expected from the critical perpendicular hydraulic gradients.

7.3.3. Erosion through filter layer

Another point of discussion is the erosion development through the filter material, which cannot be analyzed within the physical model. Before erosion is detected in the sediment trapping compartments, multiple movements of the base particles or broken arches could have already taken place. Therefore the placement method of the base material and the thickness of the filter layer can largely influence the moment of initial erosion, and thus the critical gradients.

8

Conclusions and Recommendations

This chapter concludes the research by answering the subquestions and the research question in section 8.1. Recommendations for further research are given in section 8.2.

8.1. Conclusions

The objective of this research is to further investigate the possibilities of applying an inverted geometrically open granular filter at the interface of a land reclamation and a rubble mound structure. Part of the subquestions contain new studied subjects within the research line and part of the subquestions extend already studied subjects. The subquestions are answered in the following subsections, after which the research question can be answered.

8.1.1. Relation between critical gradients and future stability of the filter

Stabilization of the open inverted filter after the critical hydraulic gradient, which is based on initial erosion, has been reached, is an interesting characteristic for land reclamation. Sand particles can erode due to shear forces and arch-breaking within the base material, when critical hydraulic gradients are reached. It is interesting to investigate a possible rearmouring effect of the base filter system after initial erosion for economic reasons. Based on the tests in this research, the critical hydraulic gradient does not necessarily imply erosion at every higher gradient, so the geometrically open granular filter could withstand higher critical hydraulic gradients than it seems from the initial erosion.

8.1.2. Dominant direction of critical gradients in combined flow

Both parallel and perpendicular hydraulic gradients can cause erosion of the base material at the interface of a land reclamation and a rubble mound structure due to a different erosion mechanism. It is of interest which hydraulic gradient during the combined flow configuration is leading and thus critical. Within this research, separate parallel and perpendicular flow configurations, as well as combined flow configurations, have been tested.

During this research, the critical hydraulic gradients during the combined flow configuration tests occur when the parallel hydraulic gradient increases and while the perpendicular gradient remains the same. Based on this research, it is therefore concluded that during the combined flow configuration, the critical hydraulic gradient depends on the parallel hydraulic gradient. The smaller the period of the water level change in compartment A, the more prominent the perpendicular gradient becomes. This is visualized with a two-dimensional numerical model in Figure 5.16. This behavior indicates a change in flow: based on this research, the flow is mainly parallel for maximum perpendicular gradients below 0.08 and becomes more perpendicular for perpendicular gradients greater than 0.08. The critical hydraulic gradients in this research line are based on initial erosion, which occurred in the stage where the flow is mainly parallel and the maximum perpendicular gradient is smaller than 0.08. For transport erosion, it is possible that the critical hydraulic gradients become more dependent on the perpendicular gradient.

8.1.3. Influence of fines content in base material on critical gradients

In this research a lower hydraulic conductivity and higher perpendicular hydraulic gradients were measured when fines are added to the base material. The critical perpendicular hydraulic gradients are increased for a higher fines content. However, it is very important to realize that the increase in critical perpendicular hydraulic gradient is caused by the difference in hydraulic conductivity and not by an

increase in strength of the base material to resist external eroding forces. This should be taken into account when the design of a base fill retaining rubble mound structure is only based on the wave climate, instead of on the hydraulic resistance of the soil as well. Therefore, the influence of a fines content on the critical perpendicular hydraulic gradient is expected to equalize for higher fines contents, when the hydraulic conductivity approaches zero.

A higher critical parallel gradient has been measured when fines are added to the base material. Due to the lower flow velocity from the lower hydraulic conductivity, the fines can act as a protective layer that protects larger sand grains, reducing their exposure to erosive forces. A slightly higher increase in the critical parallel hydraulic gradient is observed for a fines content between 5 and 10%, compared to 0 to 5%. An increasingly increased critical parallel hydraulic gradient is predicted for only low-fines contents. This prediction is based on research by Mitchener et al. (1996) who concluded that the most significant effect on erosion resistance occurs with the addition of small percentages of mud to the sand, within the region of 3% to 15% mud by weight.

8.1.4. Influence of coefficient of uniformity of base material on critical gradients

In this research, a wider graded sand (C_u=2.9) has been used as a base material compared to previous research in which more narrow graded sand was used (C_u of 1.2-2.1). The hypothesis was that the critical hydraulic gradients are lower because of unstable, finer sand fractions. To determine the influence of wider graded sand, compared to more narrow graded sand, critical hydraulic gradients from this research have been added to the results on the Stability Ratio of the research line. The Stability Ratio (SR = $\frac{d_{15f}}{d_{85b}}$) in the current research is 8.0. A higher Stability Ratio means a lower critical hydraulic gradient.

The critical hydraulic gradients measured in this research, are most comparable to those measured by Van de Ven (2019). Van de Ven (2019) used sand with a coefficient of uniformity (C_u) of 2.1 at a Stability Ratio of 8.0, which is most comparable to the uniformity of the sand combination of this research with a C_u of 2.9. The critical parallel hydraulic gradients are relatively high, because no leakage occurred during the parallel flow configuration tests. On the other hand, the critical perpendicular hydraulic gradients are low compared to the results of Lengkeek (2022). This could be explained by the difference in the coefficient of uniformity. The greater variation in grain sizes could disturb the formation of arches, which would lower the critical perpendicular gradient. The results of Graauw et al. (1984) showed that in the case of graded base material, a higher concentration of migrated material was measured, so a less well functioning open filter.

8.1.5. Influence of effective stress at the base-filter interface on critical gradients

The larger the layer of base material above the granular filter in a rubble mound structure, the larger the effective stresses at the base-filter interface. Higher critical perpendicular gradients are expected for higher effective stresses at the base-filter interface. This hypothesis is based on the expected increase in the strength of the sand arches, as the friction between the sand particles depends on the normal force. The results of the relative critical perpendicular hydraulic gradients are combined with the results of Lengkeek (2022) and show, indeed, a positive relationship. An increase of 60% of the critical perpendicular gradient is observed for a superimposed load of 100 kPa. For larger superimposed loads, a smaller increase is expected; 80% increase in critical perpendicular gradient for 200 kPa compared to 0 kPa. Non-load zones do not change significantly with increased superimposed load, so local fluidization can still occur.

The results of the parallel critical hydraulic gradients relative to effective stress, for both the parallel and combined flow configuration, show a positive correlation as well. The arching mechanism is enhanced and a side effect arises from increased effective stresses, which is compaction within the base material as the top layer was moved several millimeters down. This can lead to an increased critical parallel hydraulic gradient.

The critical perpendicular gradient of combined flow does not show a clear positive relation. However, based on this research, the parallel flow is assumed to be the main loading mechanism for maximum perpendicular gradients below 0.08, which is the case for the critical gradients during the surcharge tests.

8.1.6. Research question

The main question of the research is:

How do the fines content and coefficient of uniformity of the base material, and effective stress, influence the applicability of an inverted geometrically open granular filter at the interface of a land reclamation and a rubble mound structure in terms of both parallel and perpendicular hydraulic gradients?

According to this research line, an open inverted filter at the interface of a land reclamation and a rubble mound structure can be used as a valid alternative of a geotextile, which can have a positive effect on execution methods and costs. The research line also showed different factors that can influence the applicability based on critical hydraulic gradients, of which Stability Ratio (negative correlation) and effective stress (positive correlation with critical perpendicular gradient) were already researched. Within the current research, the following factors are investigated: future stability after initial erosion, dominant direction of critical gradient in combined flow, fines content in and coefficient of uniformity of the base material, and the effective stress on the base-filter interface. Within this research line, the critical hydraulic gradient is determined by the initial moment of erosion.

The tests performed in this research are based on a Stability Ratio of 8.0. A fines content in the base material and a superimposed load on the base-filter interface show the most significant influence on the critical gradients. Based on this research, it can be concluded that a higher fines content increases the critical perpendicular and parallel hydraulic gradients, while a higher coefficient of uniformity (i.e. less uniform) slightly decreases the critical hydraulic gradients. The open inverted filter could withstand higher gradients than the critical hydraulic gradients based on initial erosion, which means the filter can restabilize itself. Furthermore, parallel gradients up to 0.07 are measured and the parallel flow direction showed to be critical for combined flow for the conditioned tested in this research. This was the case for the critical gradients within this research, however these values are dependent on the research situation. Both for the critical parallel and perpendicular gradients, a positive relationship with the effective stress at the base-filter interface was found.

8.2. Recommendations

This research provided more insight into the functioning of the open inverted filter, which also raises new questions. Recommendations for further research are provided in this section.

Transport erosion

To investigate a higher level of erosion, for example, transport erosion, a setup that can induce larger hydraulic gradients is recommended. This requires perpendicular hydraulic gradients of at least 0.30 and parallel hydraulic gradients of at least 0.08 for Stability Ratios close to a closed filter. Investigating the limit for a more extreme type of failure, in case incidental erosion is allowed, can create a more economic design. It also allows for further investigation of the rearmouring effect of broken arches.

Inclined filter

One of the objectives of this research was to investigate the influence of inclination of the filter. Unfortunately, due to major leakage at the bottom of the setup, this was not possible. An adjusted design for the physical model to perform these tests is shown in Appendix A section B.2. The interface between a land reclamation and a rubble mound structure is inclined instead of horizontal. Higher critical hydraulic gradients are predicted for an inclined open filter system, because the direction of gravity is not perpendicular to the bed, so this is an interesting topic to research. Furthermore, the behaviour of the flow direction at an inclined filter is interesting for the critical hydraulic gradients.

Fines content

This research investigated whether a fines content has an influence on critical hydraulic gradients. Fines content is one of the most important characteristics of dredged sand for land reclamation, which can amount to tens of percent of the base material according to the overview in Table A.1. Furthermore, geotextile can get clogged with fines. The tests performed showed a positive relationship between the fines content and the critical hydraulic gradient. To determine a quantified relation, more tests are required.

To investigate higher fines contents, it is advised to increase visibility within the sediment trapping compartments to determine erosion, because of turbidity. For example, longer settling time and underwater lighting.

Gradient measurement locations within filter
The distribution of the parallel and perpendicular hydraulic gradients within the physical model is important to determine the maximum gradients. This research showed multiple perpendicular and parallel gradients along the length of the filter, giving insight into where the highest hydraulic gradients are located. By measuring other locations, e.g. perpendicular gradients at 1/4th and 3/4th of the length of the filter, one can gain more insight about the exact development of the gradients. This can be used to improve the verification of the two-dimensional numerical model.

Two-dimensional numerical model
Within this investigation, influences of the filter material are added to the two-dimensional numerical model of the base material. Within the base material, the laminar resistance is valid, but this is not always the case for the filter material. It is recommended to actually model the two-dimensional effects of the filter material separately: the inertial and turbulent resistance.

8.2.1. Field experiments

The current physical model is a full-scale horizontal section of an open inverted granular filter at the interface of a land reclamation and a rubble mound structure. This means that the results should also be interpreted in that way. Important conditions specific for this research are: two-dimensional model, fines content up to 10%, coefficient of uniformity of 2.9, Stability Ratio of 8.0, surcharge up to 200 kPa, parallel gradients up to 0.066 and perpendicular gradients up to 0.22. Further research can reduce the amount of open filter layers needed by making the relationships found less conservative. Furthermore, field experiments can increase the knowledge about the factors described below.

Irregular wave climate
During the physical model tests, the gradient is gradually increased to determine the critical hydraulic gradients. In the field, there will be an irregular wave climate. For example, the influence of a significant wave height on the critical hydraulic gradients can be investigated.

Dredged placement of base material
The method of placement of the base material can largely determine its characteristics, and thus influence the critical hydraulic gradients. In this research, there was wet placement of the base material on the filter layer and the sand combination cannot be completely homogeneously distributed. In the field, the base material is dredged, which causes variability in sediment sorting. The effects of dredged base material can be investigated.

Quarry run
Within the physical model, the shape of the induced pressures is directly transforming over the length of the filter layer during the combined flow configuration. In the field, the shape of the induced pressures is likely to already transform in the quarry run towards a sinusoidal shape. During wave transmission, the shape of the wave front is typically altered. The wave front may deform and the wave energy may be dissipated. This would create a pressure development over the granular filter, where only the ”amplitude” of the sinusoidal shape is changing.

References

Blackburn, S., Pelling, M., & Marques, C. (2019). Megacities and the coast: Global context and scope for transformation. *Coasts and estuaries journal*, 661–669.

Boersma, G. (2020). Inversed open granular filters in land reclamation structures: Modeling of the interface stability. *MSc. thesis, Delft University of Technology*.

Bratli, R., & Risnes, R. (1981). Stability and failure sand arches. *Society of petroleum engineers Journal*.

Carman, P. (1939). Permeability of saturated sands, soils and clays. *The Journal of Agricultural Science*, *29*(2), 262–273.

Chapuis, R., & Aubertin, M. (2003). Predicting the coefficient of permeability of soils using the kozeny-carman equation. *Canadian Geotechnical Journal*, *40*(3).

Chevalier, B., Combe, G., & Villard, P. (2012). Experimental and discrete element modelling studies of the trapdoor problem: Influence of the macro-mechanical frictional parameters. *Acta geotechnical journal*, *7*(1), 15–39.

CIRIA; CUR; CETMEF. (2007). *The rock manual: The use of rock in hydraulic engineering.* (2nd ed.). C683, CIRIA.

Dalrymple, R., Losada, M., & Martin, P. (1991). Reflection and transmission from porous structures under oblique wave attack. *Journal Fluid Mechanics*, *224*, 625–644.

Damen CNC. (2023). *Stepper motor dcnc-nema34-8.0nm (ip54)*. https://www.damencnc.com/nl/stepper-motor-dcnc-nema34-8-0nm-ip54/a2217?search=Stepper%20Motor%20DCNC-NEMA34-8.0Nm%20(IP54)

Deltares. (2023). *Deltares, instrument, wave height meter*. https://cms.deltares.nl/assets/common/downloads/Wave-height-meter.pdf

den Bos, J. V., & Verhagen, H. (2018). *Breakwater design Lecture notes CIE5308*. Delft University of Technology.

Dolzyk, K., & Chmielewska, I. (2014). Predicting the coefficient of permeability of non-plastic soils. *Soil Mechanics and Foundation Engineering*, *51*(5).

E. Ghane, L. B., N.R. Fausey. (2014). Non-darcy flow of water through woodchip media. *Journal of Hydrology*, *519*, 3400–3409.

Farnell. (2023). *Farnell, an avnet company, 26pcafa6d, pressure sensor*. https://nl.farnell.com/honeywell/26pcafa6d/pressure-sensor-0-1psid/dp/731742?ost=731742

Graauw, A. D., der Meulen, T. V., & der Does de Bye, M. V. (1984). Design criteria for granular filters. *Journal of Waterway, Port, Coastal and Ocean Engineering*.

Gu, Z., & Wang, H. (1990). Gravity waves over porous bottoms. *Coastal Engineering Elsevier*, *15*(5), 497–524.

Gunberg, K., Green, R., & Ashmawy, A. (2007). NEESR-II: Mechanisms and implications of time-dependent changes in the state and properties of the recently liquefied sands.

Hattamleh, O. A., AlShalibi, F., Qablan, H. A., & Al-Rousan, T. (2010). Effect of grain crushing and bedding plane inclination on aqaba sand behavior. *Bulletin of engineering geology and the environment*, 41–49.

Honeywell. (2015a). *Datasheet: Miniature low pressure flow-through sensors 24pc series. uncompensated/unamplified 0.5 psi to 250 ps*. https://prod-edam.honeywell.com/content/dam/honeywell-edam/sps/siot/en-us/products/sensors/pressure-sensors/board-mount-pressure-sensors/24pc-flow-through-series/documents/sps-siot-board-mount-24pc-series-miniature-flow-through-low-pressure-sensors-product-sheet-32302911-a-en-ciid-154169.pdf?download=false

Honeywell. (2015b). *Datasheet: Miniature low pressure sensors 26pc series. compensated/unamplified 1 psi to 250 psi*. https://www.farnell.com/datasheets/2002509.pdf

Iglesia, G. R., Einstein, H. H., & Whitman, R. V. (2013). Investigation of soil arching with centrifuge tests. *Journal of geotechnical and geoenvironmental engineering*, *140*(2), 248–256.

Jebur, Y. (2018). *Al-mustaqbal university college: Soil mechanics.* Retrieved March 20, 2023, from https://uomus.edu.iq/img/lectures21/MUCLecture_2021_10311889.pdf

Keaton, J. (2018). *Coefficient of uniformity. Encyclopedia of Engineering Geology*. Springer.

Khan, T., Farooq, K., Muhammad, M., Khan, M., Shah, S., Shoaib, M., Aslam, M., & Raza, S. (2019). The effect of fines on hydraulic conductivity of lawrencepur, chenab and ravi sand. *Advances in Experimental and Theoretical Studies of Fluid Flow and Solute Transport in Porous Media*.

Leadshine Technology Co. (2017). User manual em882s digital microstep drive. *The Title of the Journal*.

Lengkeek, R. (2022). Geometrically open inverted granular filters. *MSc. thesis, Delft University of Technology*.

Micro-Epsilon. (2000). *optoNCDT 1300 low cost sensors with analogue outputs*. http://www.micro-epsilon.pl/download/dat--optoNCDT-1300--en.pdf

Miedema, S. (2010). Constructing the shields curve, a new theoretical approach and its applications. *WODCON XIX dredging congress Beijing China*.

Mitchener, H., Torfs, H., & Whitehouse, R. (1996). Erosion of mud/sand mixtures. *Elsevier Coastal Engineering*, *29*, 1–25.

Mohr, H., Draper, S., White, D., & Cheng, L. (2021). The effect of permeability on the erosion treshold of fine-grained sediments. *Coastal Engineering Journal*, *163*.

Nolthenius, R. T. (2018). Sandfill-retaining rubble mound structures: Evaluating the behaviour of sediments at the interface of a rubble mound with a reclamation, by means of physical modelling. *MSc. thesis, Delft University of Technology*.

Ockeloen, W. (2007). Open filters in breakwaters with a sand core: Study into the stability of granular geometrically open, hydraulically sand-open filters in breakwaters with a sand core. *MSc. thesis, Delft University of Technology*.

Osserman, R. (2010). How the gateway arch got its shape. *Nexus Network Journal*, *12*(2), 167–189.

Pap, M., & Mahler, A. (2021). Prediction of permeability coefficient for quaternary sediments of drava river using different empirical correlations. *The paper was published in the proceedings of the 6th International Conference on Geotechnical and Geophysical Site Characterization*.

Polidoro, A., Allsop, A., & Pullen, T. (2015). Conference paper: Exploring the need for geotextile filters for rubble bunds retaining sand-fill islands [DOI: 10.1061/9780784480304.080].

Rahardjo, H., Satyanaga, A., D'Amore, G., & Leong, E. (2012). Soil–water characteristic curves of gap-graded soils. *Engineering geology journal*, *125*.

Rajapakse, R. (2016). Static and dynamic analysis for pile design and construction rules of thumb, 81–98.

Rui, R., Tol, A. F., Xia, Y. Y., Eekelen, S. J. M. V., & Hu, G. (2016). Investigation of soil-arching development in dense sand by 2d model tests. *Geotechnical testing journal*, *39*(3).

Schiereck, G. J., & Verhagen, H. J. (2019). *Introduction to bed, bank and shore protection* (2nd ed.). Delft Academic Press.

Schulz, R., Ray, N., Zech, S., Rupp, A., & Knabner, P. (2019). Beyond kozeny–carman: Predicting the permeability in porous media. *Transport of porous media*, *130*, 487–512.

Shahabi, A., Das, B., & Tarquin, A. (1984). An empirical relation for coefficient of permeability of sand. *Conference of geomechanics*.

Shields, A. (1936). *Anwendung der aehnlichkeitsmechanik und der turbulenzforschung auf die geschiebebewegung*. Soil Conservation Service.

Slichter, C. (1897). Theoretical investigation of the motion of ground waters. *U.S. Geological Survey*, *19*, 295–384.

Terzaghi, K. (1943). *Theoretical soil mechanics*. Wiley.

TU Delft. (2020). *Permeability test. Section of Geo-Engineering at Delft University of Technology.* https://www.youtube.com/watch?v=S60sDC3i5pw

Van de Ven, D. (2019). Granular open filter in rubble mound sand retaining structures: Physical model tests of a negative geometrically open filter layer. *MSc. thesis, Delft University of Technology*.

Van Gent, M. (1995). Porous flow through rubble-mound material. *J. Waterway, Port, Coastal, Ocean Eng.*, 176–181.

Van Oord. (2023). *Van Oord: Meer ruimte creëren voor de groeiende wereldbevolking*. Retrieved February 28, 2023, from https://www.vanoord.com/nl/expertise/landaanwinning

Vanneste, D., & Troch, P. (2012). An improved calculation model for the wave-induced pore pressure distribution in a rubble-mound breakwater core. *Coastal engineering journal*.

Verruijt, A. (2017). *Theory and applications of transport in porous media, an introduction to soil mechanics: Permeability*. Springer.

Wils, L., Impe, P. V., & Haegeman, W. (2015). One-dimensional compression of a crushable sand in dry and wet conditions. *Geomechanics from Micro to Macro. Taylor and Francis Group*.

Winterwerp, J., & van Kesteren, W. (2004). *Introduction to the physics of cohesive sediment in the marine environment. developments in sedimentology*.

Details physical model

This appendix gives a detailed description of all the measurement equipment used in the physical model; see section A.1. Furthermore, examples of the characteristics of dredged material used in land reclamation projects are given in section A.2.

A.1. Measuring equipment

In this section, a detailed description of the measuring equipment used in the test setup is given. Figure A.1 shows two pictures of the test setup.

Figure A.1: Empty test setup and the base case test setup during the perpendicular flow configuration.

A.1.1. Plunger system

The plunger moves up and down in a range of 60 to 140 mm and has a cross-sectional area of 6.1 dm^2 and a height of 425 mm. The total area of compartment A is 14.7 dm^2. Over the width, there is just sufficient space available to place the water level gauge and to possibly fill and empty the compartment for the perpendicular flow configuration tests. There is some space left over the length in case a ”play” occurs in the movement of the plunger. Compartment A is shielded for safety. A ”DCNC-NEMA34-8.0Nm (IP54)” stepper motor (Damen CNC, 2023) drives the plunger system in combination with a ”EM882S” digital microstep drive (Leadshine Technology Co., 2017). Pictures of the plunger system are shown in Figure A.2.

Figure A.2: Pictures of the plunger system.

A.1.2. Laser

The ”optoNCDT 1300-200” laser (0904209) is used to measure the movement of the plunger, see Figure A.3. The optoNCDT 1300-200 laser has a measurement range of 60 to 260mm with a resolution of 50 μm (Micro-Epsilon, 2000). The laser has safety class 2, which means that no safety precautions are required.

Figure A.3: Laser optoNCDT 1300-200 (Micro-Epsilon, 2000).

The laser is connected to DASYLab and a measuring frequency of 10 Hz is applied. The laser was calibrated by testing the range of the laser, which is from 1.91 to 10 V, at multiple distances. The correlation is linear, as can be seen in Figure A.4, which also shows the calibration formula.

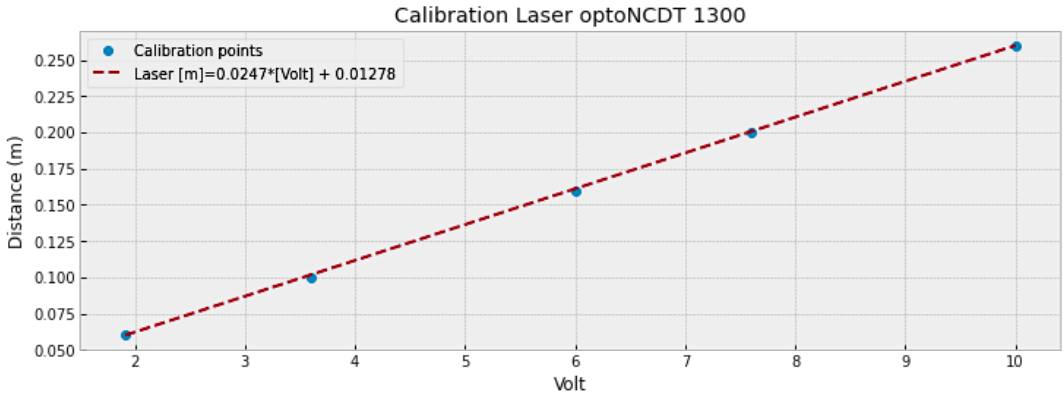

Figure A.4: Calibration laser optoNCDT 1300-200.

A.1.3. Pressure sensors

The setup contains 9 miniature pressure sensors from the 26PC series (26PCAFA6D), see Figure A.5. Sensors provide gauge pressure detection performance and inherently stable mV outputs for 1 psi (Farnell, 2023). That is why the amperage is kept constant, which makes the resistance bridge of these pressure sensors more in balance (compared to constant voltage). Pressure sensors should always be submerged during tests for best performance, and the maximum water level that the sensors endure during experiments is 63 cm.

Figure A.5: 26PC series Pressure sensor (26PCAFA6D), (Farnell, 2023).

To calibrate the pressure sensors, the voltage is measured at certain water depths. The measuring range is from -10 to 10 V. With an amplification of 400 times, this results in the calibration formulas of Figure A.6. The reliability of pressure sensors has been investigated in Appendix C.

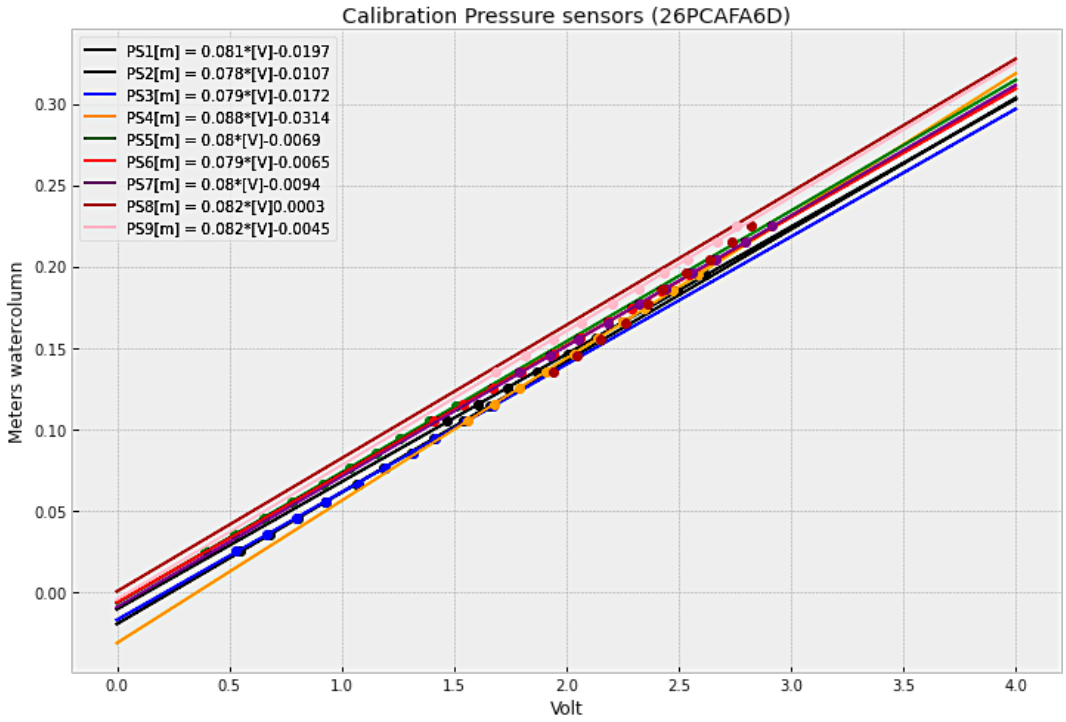

Figure A.6: Calibration pressure sensors.

Design resin pressure sensors

An air tube is connected to the sensor to measure the water pressure relative to the atmospheric pressure. A stiff air tube is used to avoid airtight squeeze during testing. Furthermore, pressure sensors must be waterproof, so a plastic resin is made. The size of the resin must be as small as possible to minimize the disturbance of the filter and the base material. However, a general shape has been created, so they can

still be applied in other research. In addition, a small mounting plate is part of the plastic resin to easily connect the pressure sensors to the frame.

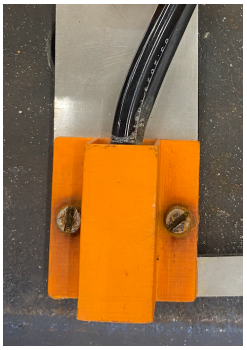

Figure A.7: Resin pressure sensor.

Frame pressure sensors

A pressure sensor frame has been designed to measure the perpendicular gradient at three different locations in the base material and the parallel gradient over the filter-base interface. The larger the distance between the corresponding pressure sensors, the more accurately the gradient can be measured. Sensors are placed in such a way that the pressure sensors are always submerged during testing and that the maximum pressure is below 1 psi (most critical pressure in case of the inclined setup in section B.2).

The frame is made of stainless steel. The frame size is as small as possible to minimize disturbance to the filter and base material. When the frame has the same length as the compartment of the base and filter material, the frame can be connected to both sides to guarantee the same position for each test. The frame is shown in Figure A.8.

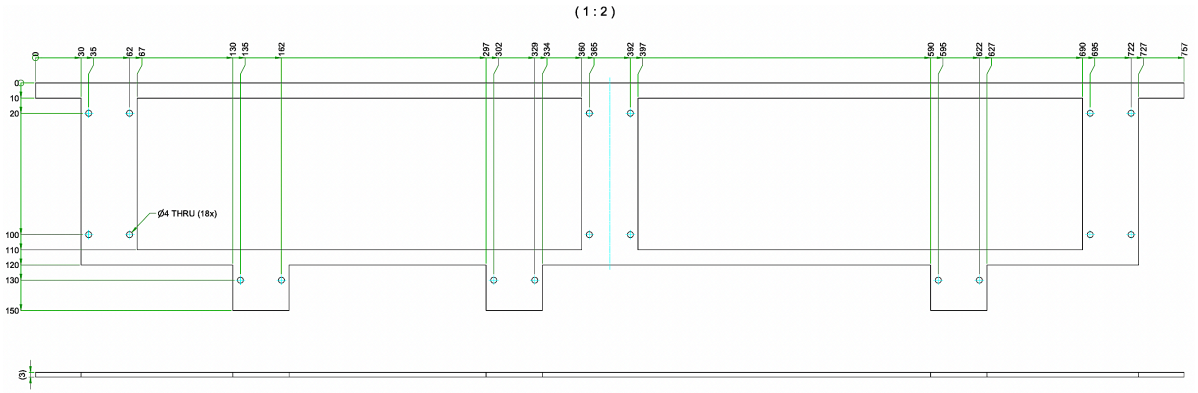

Figure A.8: Stainless steel frame design for the pressure sensors.

A.1.4. Water level gauges

Two water level gauges (”WLG23” and ”WLG25”) are used to measure the water levels in compartments A and C. The maximum range of water levels in compartment A caused by the movement of the plunger is around 6.5 cm. The water level gauges, shown in Figure A.9, have a sufficient length (0.5 m). It consists of two rods that act as the electrodes of an electric conduction meter and a box with electronics (may not get wet) (Deltares, 2023). The gauges are connected to a control unit to adjust the gain and zero shift of the output signal and to provide the probe with power; see Figure A.9.

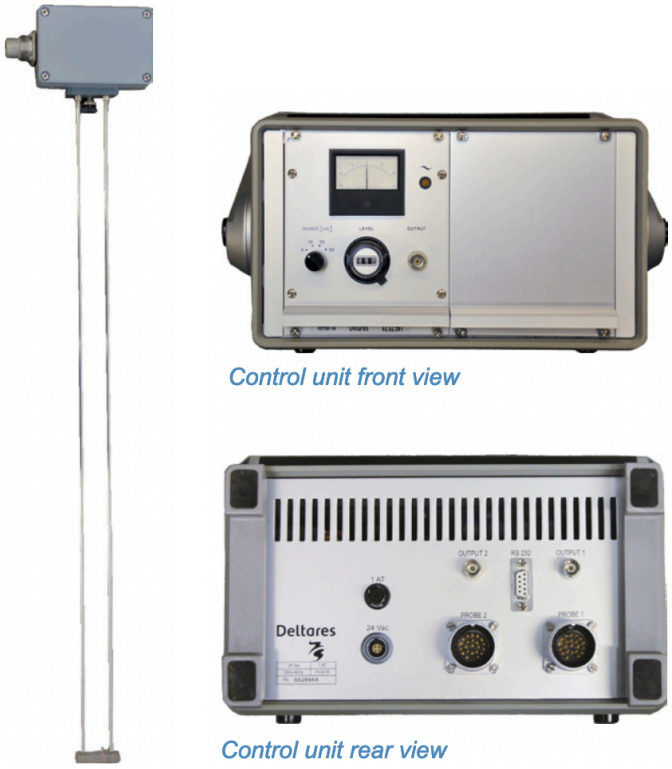

Figure A.9: Water level gauge and control unit (Deltares, 2023).

Both control units are connected to DASYLab. Water level gauges measure at a frequency of 10 Hz. The sensor output ranges from -10 to 10 V, which corresponds to a range of 20 cm ("WLG23") and 50 cm ("WLG25"), depending on the position within the setup. The calibration points are shown in Figure A.10. The reliability of the water level gauges has been researched in the Appendix C. It shows that the analog output signal is linearly proportional to the change in water level between the sensor rods.

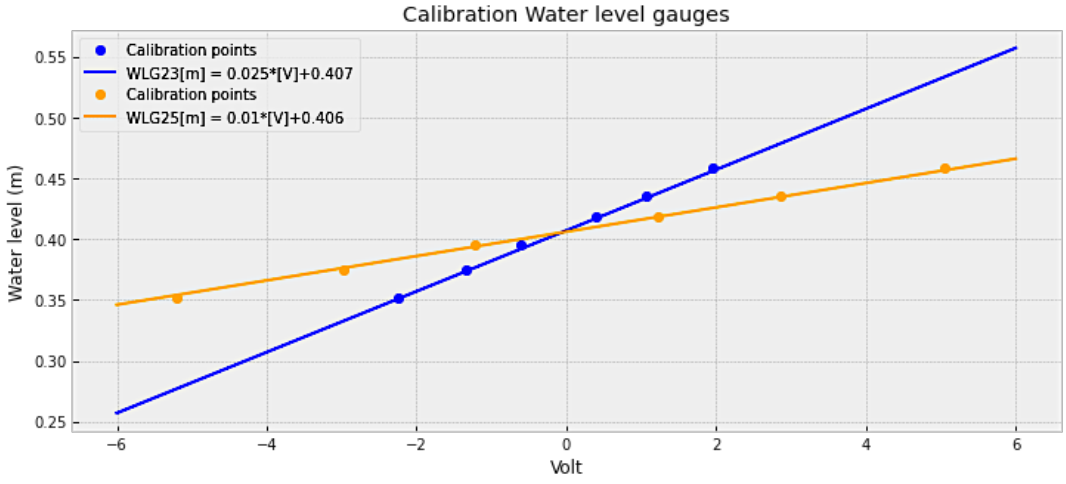

Figure A.10: Calibration water level gauges ("G23" and "G25").

A.1.5. GoPro cameras

Three "GoPro HERO 10" cameras were used to record a time lapse of the bottom cells. The time-lapse recorded one frame per 5 seconds. The position of the cameras was fixed for all tests. For lighting of the sediment trapping compartments, a "Yongnuo LED Video Light", with a light output of 10800 lm and a

color temperature of 5500K has been used.

A.2. Dredged sand

The particle distribution of the base fill largely depends on the dredged sand that is available at the location of the project. To gain some insight into realistic sand compositions, various particle size distributions of land reclamation projects are summarized in Table A.1.

Table A.1: Examples particle distributions of land reclamation projects (Van Oord, 2023).

Location land reclamation	Fines content [%]	d_{50} [mm]	d_{85} [mm]	Max. particle size [mm]	C_u	C_c
North Sea coast (North), The Netherlands (top layer)	0.68	0.431	0.71	11.7	2.231	0.932
North Sea coast (North), The Netherlands (lower layer)	0.58	0.351	0.99	12.3	2.323	0.906
North Sea coast (South), The Netherlands (avg.)	1.4	0.286	0.45	2.0	2.009	1.030
Gulf of Finland, Russia (averaged)	0.0	0.524	3.80	10	3.948	0.726
River Thames, England (near port, averaged)	13.4	3.310	6.82	15.6	21.041	3.283
River Thames, England (sea reached, averaged)	7.7	0.262	1.00	10.6	2.404	1.110
Mediterranean coast, Spain (averaged)	15.0	0.343	0.73	4.75	12.926	5.518
Black Sea coast, Romania (averaged)	0.5	0.358	2.50	8.0	3.027	0.770
Java, Indonesia (averaged)	28.0	0.193	0.80	18.0	16.914	1.059

B

Design setups

This appendix illustrates the different setups of the physical model. Chapter 4 shows illustrations of the base cases and the parallel flow configuration when a superimposed load is applied on the filter system. The other setups, which are given in this appendix, are the combined and perpendicular flow configuration when a superimposed load is applied and an example of an inclined physical model is given in section B.2.

B.1. Inclined setup

Illustrations of the physical model when a superimposed load is applied for the combined and perpendicular flow configurations.

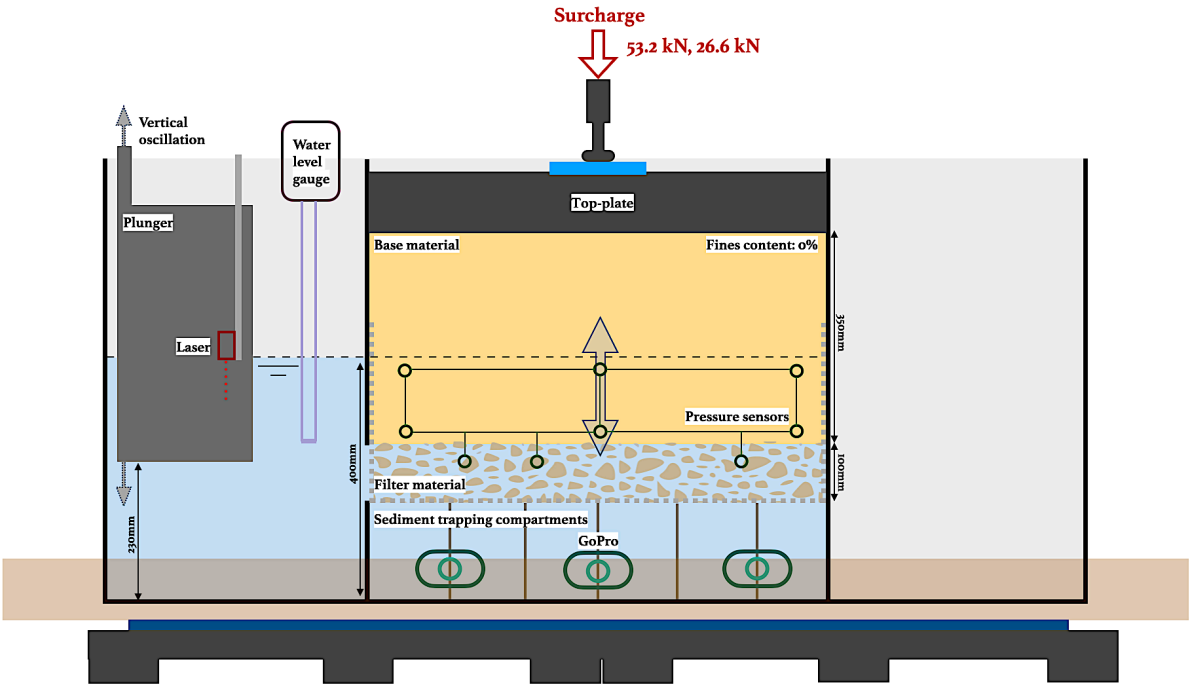

Figure B.1: Setup of the physical model under a surcharge in the perpendicular flow configuration.

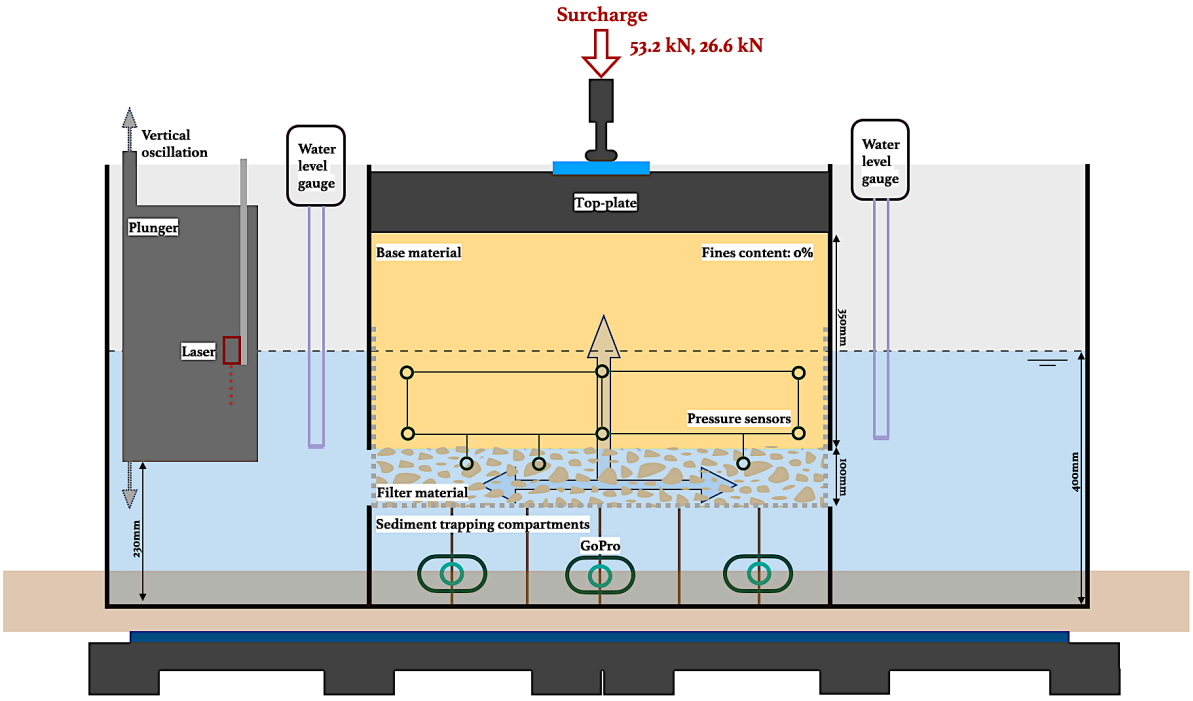

Figure B.2: Setup of the physical model under a surcharge in the combined flow configuration.

B.2. Inclined setup

The influence of an inclined base filter system could also be investigated. In this regard, the whole experimental setup is inclined to 30°, which means adjustments to the setup are necessary, see Figure B.3. The thickness of the base layer increases from 350 mm to 700 mm. Initially, a test at 0° and 30° can be carried out with this setup, to determine whether an inclination influences the critical hydraulic gradients. If this is the case, an experiment can also be carried out at 10° and 20°. Due to practical constraints, it is advised that the testing will focus solely on the perpendicular flow configuration.

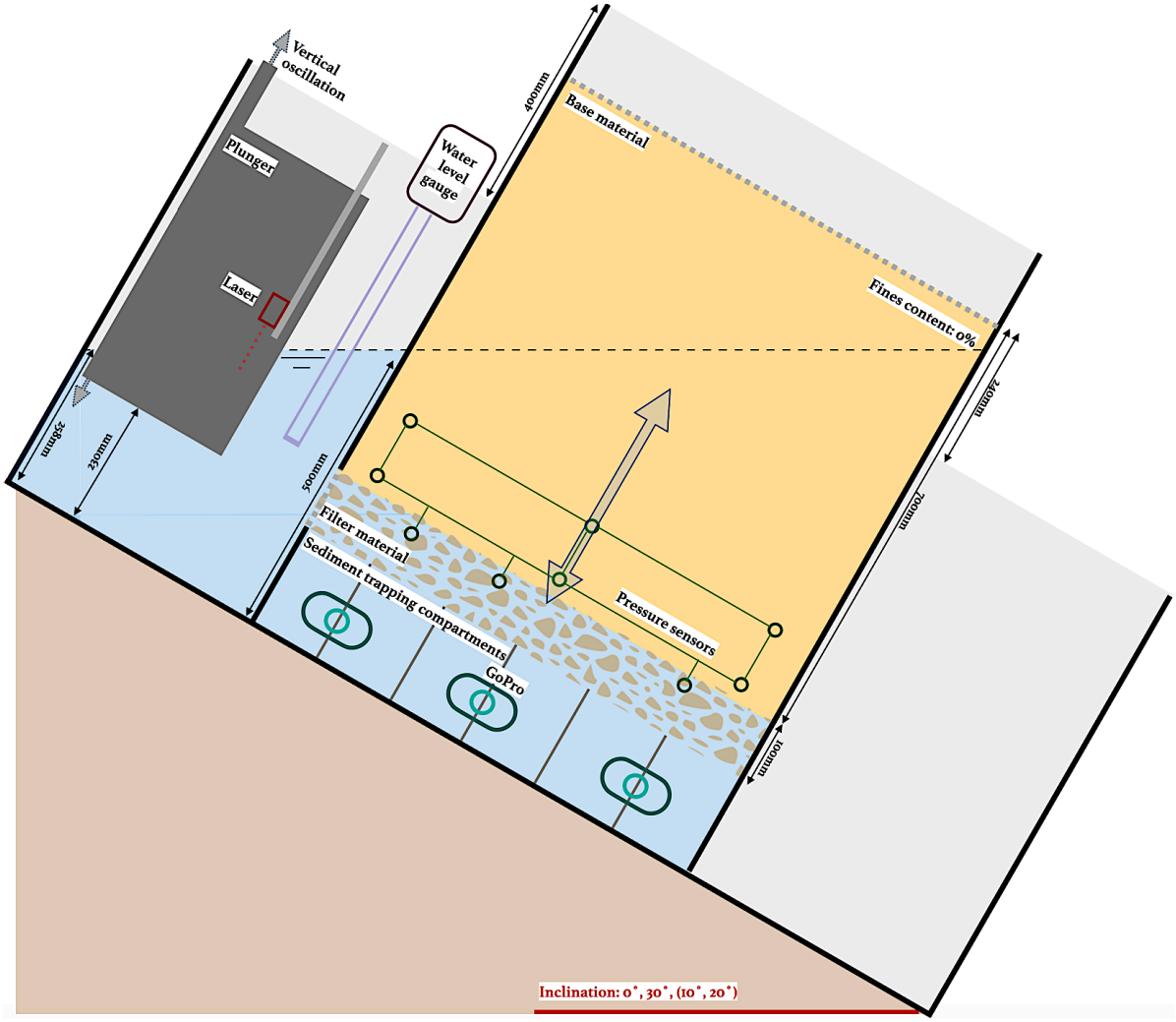

Figure B.3: Setup of the physical model under an inclination in the perpendicular flow configuration.

C

Accuracy measuring equipment

Within this appendix, the accuracy of the pressure sensors is further analyzed. In section C.1 the accuracy of the pressure sensors is explained on the basis of technical specifications. In the next section, section C.2, the pressure sensors have been tested when measuring atmospheric pressure relative to atmospheric pressure. Based on this test, the accuracy of the hydraulic gradients has been determined for chapter 6. In section C.3 the results of multiple calibration tests are shown over a time span of 3.5 weeks. Finally, an example of raw pressure sensor data is shown in section C.4.

C.1. Technical specifications

The precision of pressure sensors is of importance in ensuring the reliability of the experimental results. In this research, the utilization of Honeywell's 26PCAFA6D pressure sensors, which feature temperature compensation, has been adequate. These sensors have been designed to measure a maximum relative pressure of 1 psi. Analysis of their performance characteristics reveals a maximum span variation of ±2 mV to 16.7 mV (±12%) (Honeywell, 2015b, Table 3).

For the determination of linearity, assessed using the Best Fit Straight Line methodology (using the "least squares" approach), the maximal deviation from a linear trend is 0.5% of the span. Similarly, the 24PCEFA6D pressure sensor, engineered for a range of 0-0.5 psi and not temperature compensated, exhibits a maximum span fluctuation of ±10 mV to 35 mV (±29%), along with a maximum linearity deviation of ±1.0% of the span (Honeywell, 2015a, Table 3).

In the course of each test segment, carried out at intervals of 50 minutes and repeated ten times per test, the voltage range is calibrated against alterations in water levels, as gauged by water level sensors. In this manner, the short interval between calibrations diminishes the interval within which a potential span shift might occur. Consequently, this approach can increase precision.

The null offset of the 26PCAFA6D pressure sensors is found to have a possible deviation of 0 ±1.5 mV. It should be noted that changes in offset during testing and during the reference heights introduce inaccuracies. Despite the temperature compensation inherent to pressure sensors, an alteration of temperature by 25 °C can cause a span shift of ±1.0% and a null shift of ±0.5 mV. However, it is important to note that variations in laboratory temperature are expected to be modest, around 4 °C. Pressure oscillations during testing can cause a hysteresis of ±0.5 mV. Amplifiers with a gain of 400x were used consistently during the physical model tests.

To verify the precision of the 26PCAFA6D pressure sensors, rigorous tests were conducted in the laboratory setting. An extended "air-to-air" test spanning 4.5 days was performed and three calibration tests were carried out that involved the relative pressure between air and water. The results of these tests are shown in the following sections.

C.2. "Air-to-air" test

The 26PCAFA6D pressure sensors are inherently referenced to atmospheric pressure through a small connecting tube in one of the two ports. In the context of the "air-to-air" test, where both ports were exposed to the same atmospheric pressure, any alterations in measured pressure were anticipated to be attributable to potential noise and variations in temperature stemming from the presence of the connecting tube. This is because no relative pressure deviations are expected under such conditions. The test

Table C.1: Output fluctuations from the ”air-to-air” test.

Pressure sensor	1	3	4	5	6	7	8	9
ΔV /hr	0.007	0.0089	0.0312	0.0094	0.0855	0.0076	0.0080	0.0168
% (0.5 V range)	1.4	1.78	6.24	1.88	17.1	1.52	1.60	3.36
Δm w.c. /hr	0.00057	0.00073	0.00256	0.00077	0.00701	0.00062	0.00066	0.00138

itself spanned a duration of 113 hours, employing a measurement frequency of 0.1 Hz. Unfortunately, Pressure Sensor 2 was non-functional during this test.

Fluctuations were observed to persisted within a range of approximately 0.03 V to 0.07 V (equivalent to 0.08 mV to 0.18 mV prior to amplification); see Figure C.1. Each test segment of the overall test was initiated with two reference heights, a practice aimed at establishing the voltage-to-meters water column ratio for that specific moment.

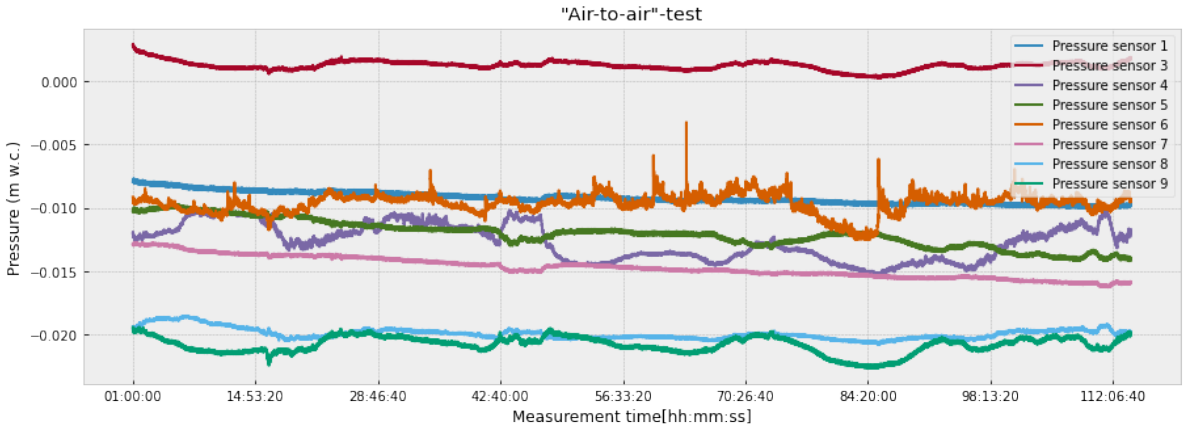

Figure C.1: Output pressure sensors during ”air-to-air” test.

Given that each test segment encompassed a duration of roughly 1 hour, the results of the ”air-to-air” test were parsed into 1-hour intervals. Within these intervals, the difference between the maximum and minimum voltages has been quantified, see Table C.1. Throughout the testing procedure, the operating range of the pressure sensors was within approximately 0.5 V. This value was used to calculate the percentage of atmospheric noise encountered during the test.

Pressure sensors 1, 5, and 7 exhibit linearly changing offsets of relative pressure measurements as time progresses. This trend suggests a continuous shift, rather than being attributed to temperature-induced uncertainties or inherent noise. Pressure sensor 6 demonstrates distinct instances of abrupt voltage shifts during the ”air-to-air” test. Both phenomena underscore the potential for inherent deviations in pressure sensors themselves and should be taken into account in the overall evaluation of the research outcomes. During the research, multiple pressure sensors have been replaced.

C.2.1. Influence on hydraulic gradients

Based on the ”air-to-air” test and calibration tests, it is useful to remove the offset from the pressure sensor data, as shown in Appendix D. This largely removes the uncertainty of ”beta” in the calibration formula. According to the calibration tests, the slope of the calibration formula (”alpha”), is minimal over time and is unlikely going to influence the results per test segment. Therefore, the ”alpha” value is determined per test per pressure sensor based on the reference heights and averaged per test, this is elaborated in Appendix D.

The ”air-to-air” test reveals certain outliers that can occur. An extreme outlier occurs at pressure sensor 6 which corresponds to around 7.0 mm, see Figure C.1. The uncertainty of pressure sensors can be quantified. A histogram of the maximum deviation per hour is shown in Figure C.2 and resembles a

lognormal distribution as it is inherently skewed and not normal. As the deviations are not conform to standard parametric assumptions, bootstrapping has been applied to estimate the uncertainty of the data. The 90% confidence interval of the mean ranges from 0.000454 till 0.000504 m w.c., as can be seen in Figure C.2. The accuracy according to the specifications is 0.7 mm (Honeywell, 2015b). The highest deviation in the 90% confidence interval of the mean during a test segment (0.50 mm) is taken into account for both pressure sensors per set, to determine the uncertainty of the hydraulic gradients. The uncertainty of the perpendicular hydraulic gradient is 0.012 (I_{34}) and that of the parallel hydraulic gradient (I_{89}) is 0.0035.

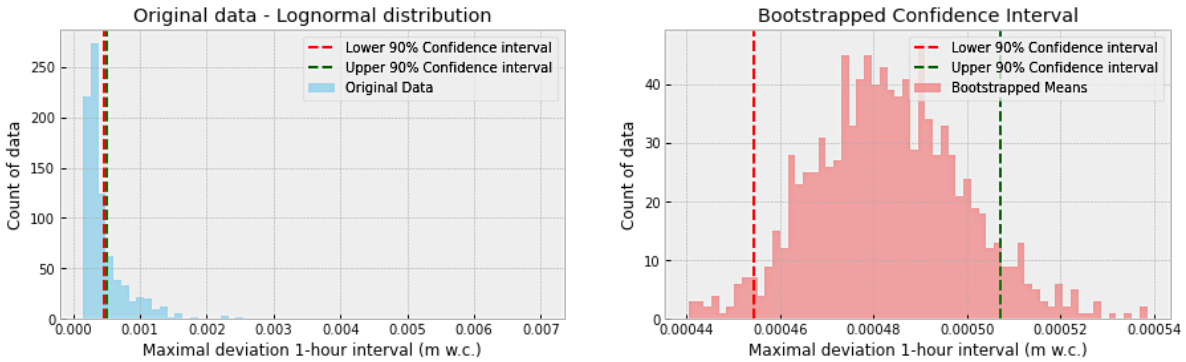

Figure C.2: Maximum deviations in 1-hour intervals during "air-to-air" test (lognormal distributions) and the corresponding 90% confidence interval.

C.3. Calibration tests

The pressure sensors employed in the research were utilized to measure differential water pressures relative to the prevailing atmospheric pressure during the course of the test. These sensors underwent a meticulous calibration, conducted using water level gauges integrated within the physical model without any base or filter material. The calibration process has been repeated after 1 and after 2.5 weeks. Throughout these calibrations, the water level within the experimental setup was systematically varied within the range of 35 to 45 cm with at least 7 calibration data points.

The calibration equation is according to the format [m w.c.] $= \alpha \cdot$[V]$+\beta$. The derived alpha and beta coefficients, acquired from the different calibration tests, are shown in Table C.2. This table also features absolute variations in alpha and beta concerning the initial calibration test, along with the relative change in alpha. These results were calculated via the application of the Best Fit Straight Line methodology, facilitated through the "least squares" approach as realized by the "scipy.optimize.curve-fit" function. The accuracy of the fitting process is quantified through the corresponding "R-squared" value. The calibration formula of pressure sensor 8 deviates, because its output dropped by 3 mV/min during the first calibration.

In agreement with the calibration of the pressure sensors, the water level gauges themselves underwent a similar calibration procedure. However, no significant variations in the calibration formula occurred for the water level gauges.

C.4. Examples raw data

This section presents an illustrative case involving an unexpected occurrence of pressure sensor output shifts during the 200 kPa surcharge test within the combined flow configuration (test 14). It became apparent during the evaluation of pressure sensors 1 and 2, which are positioned within the base material, 8 centimeters above each other. Unprocessed output readings from pressure sensors are shown in Figure C.3.

Table C.2: Calibration tests pressure sensors. The parameter outcomes and the uncertainties.

	Week	Alpha	Difference	%	Beta	Difference	R-squared
Pressure sensor 1	Week 0	0.081			-0.0197		0.9999
	Week 1	0.083	0.002	2.29	-0.0194	0.0003	1.0000
	Week 3.5	0.082	0.001	1.78	-0.0063	0.0134	0.9999
Pressure sensor 2	Week 0	0.078			-0.0107		0.9999
	Week 1	0.081		2.83	-0.0156	-0.0049	1.0000
	Week 3.5	-	-	-	-	-	-
Pressure sensor 3	Week 0	0.079			-0.0172		0.9998
	Week 1	0.078	-0.001	-1.26	-0.0175	-0.0003	0.9998
	Week 3.5	0.081	0.002	3.1	-0.0177	-0.0005	1.0000
Pressure sensor 4	Week 0	0.088			-0.0314		1.0000
	Week 1	0.084	-0.004	-4.41	-0.0122	0.0192	0.9999
	Week 3.5	0.086	-0.002	-1.92	-0.0490	-0.0176	1.0000
Pressure sensor 5	Week 0	0.080			-0.0069		0.9999
	Week 1	0.082	0.002	1.69	-0.0074	-0.0005	1.0000
	Week 3.5	0.082	0.002	1.83	-0.0083	-0.0014	1.0000
Pressure sensor 6	Week 0	0.079			-0.0065		0.9999
	Week 1	0.080	0.001	1.91	-0.0078	-0.0013	0.9999
	Week 3.5	0.081	0.002	2.88	-0.0615	-0.0550	1.0000
Pressure sensor 7	Week 0	0.080			-0.0094		0.9999
	Week 1	0.082	0.002	1.61	-0.0084	0.001	1.0000
	Week 3.5	0.081	0.001	0.39	-0.0030	0.0064	1.0000
Pressure sensor 8	Week 0	0.102	0.078		-0.063		0.9987
	Week 1	0.082	-0.02	-19.59	0.0003	0.0633	1.0000
	Week 3.5	0.081	-0.021	-20.28	0.0071	0.0701	1.0000
Pressure sensor 9	Week 0	0.082			-0.0045		0.9990
	Week 1	-	-	-	-	-	-
	Week 3.5	0.081	-0.001	-1.46	0.0052	0.0097	1.0000

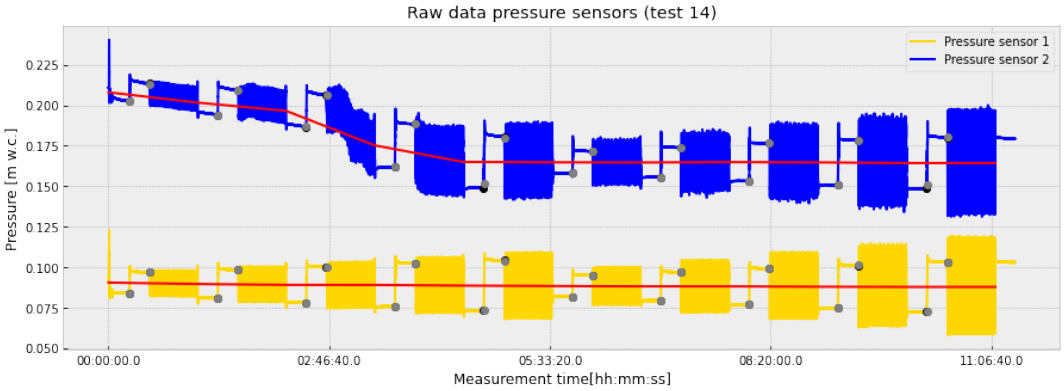

Figure C.3: Raw output pressure sensors 1 and 2 during the 200 kPa surcharge test within the configuration of combined flow.

Pressure sensor 2 displays a gradual reduction in its null offset in the initial phase of the test. The reference water heights are expected to correspond to a hydrostatic head, subsequently reflecting a constant voltage from the pressure sensors. Also, at timestamp 02:50:00, a distinct and abrupt voltage

shift becomes apparent, introducing a deviation from the anticipated behavior. This abrupt voltage shift and gradual reduction in null offset are not visible in the output of Pressure sensor 1. These deviations were also observed during the ”air-to-air” test. Appendix D shows how to analyze these data.

D

Data analysis pressure sensors

This appendix gives more details on the analysis of the data retrieved from the physical model, it is an extension on the data analysis described in subsection 4.2.2. First, the removal of the offset is explained and the determination of the slope of the calibration of the pressure sensors in section D.1. Then details on the filtering of pressure sensor data are given in section D.2. Finally, in section D.3, the maximum hydraulic gradient per test segment is explained.

D.1. Determination of calibration slope and removing off-set

Figure D.1 shows the raw pressure sensor output of two pressure sensors from test 10. The grey dots show the last 20 and 10 seconds of the reference heights, and the average between these dots is used to determine the difference in Voltage between the reference heights. This difference is related to a difference in water level as determined by the water level gauges.

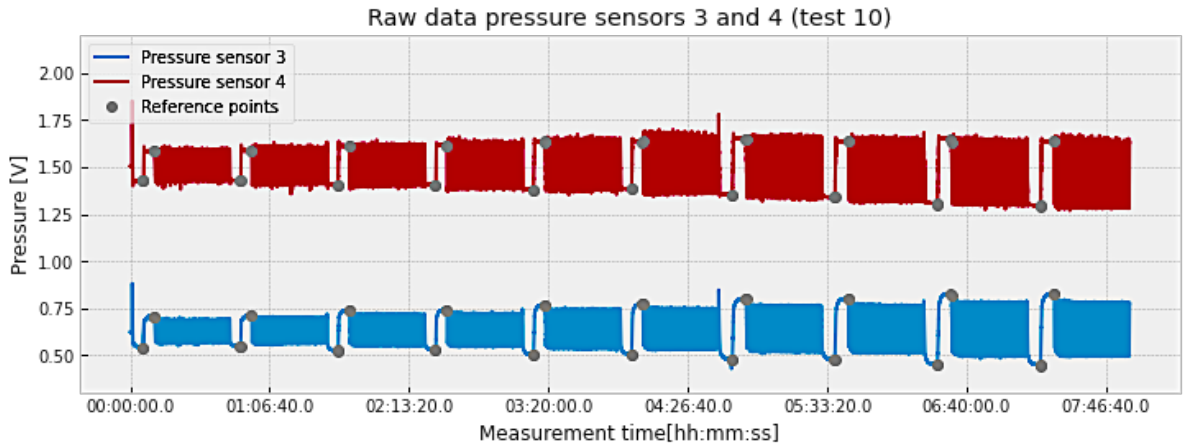

Figure D.1: Raw pressure data from sensors 3 and 4 from test 10.

The ratio between the difference in Voltage between the reference heights and the difference in water level measured by the water level gauges is calculated and shown in Figure D.2. The averages of the ratios based on the reference heights, illustrated by the continuous lines, are used as the ”alpha” value in the calibration formula ([m w.c.] $= \alpha \cdot$[V]$+\beta$). Based on the calibration tests of Appendix C, the ”alpha” value can vary between pressure sensors and over time. These variations were not extreme, and the limits of these variations are also shown in Figure D.2 by the black dotted lines.

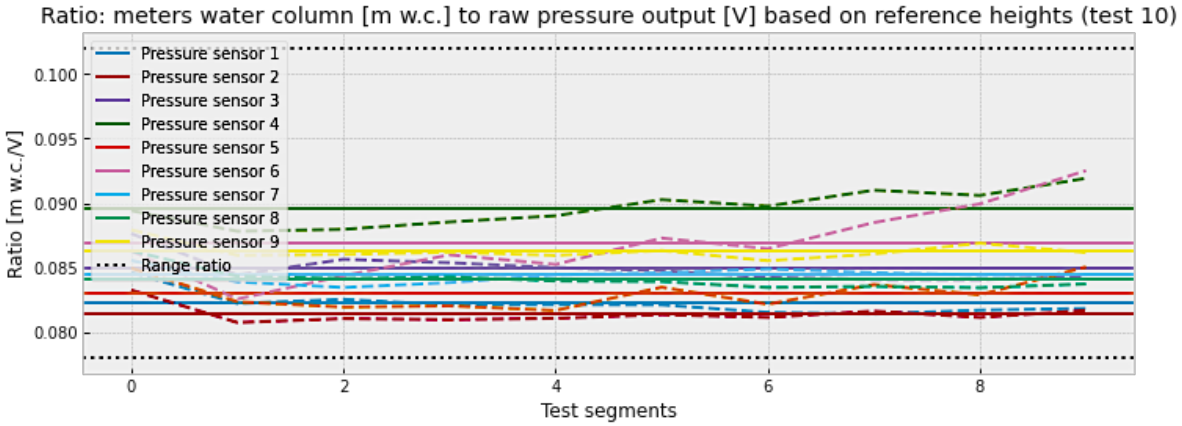

Figure D.2: Ratios pressure in meters water column to raw sensor output in Voltage for test 10.

According to Table C.2 the offset can vary greatly. Therefore, it is decided to remove the total off-set from the pressure sensor data, to improve the calculation of the hydraulic gradients. The mean pressure per oscillation is calculated, as illustrated in Figure D.3.

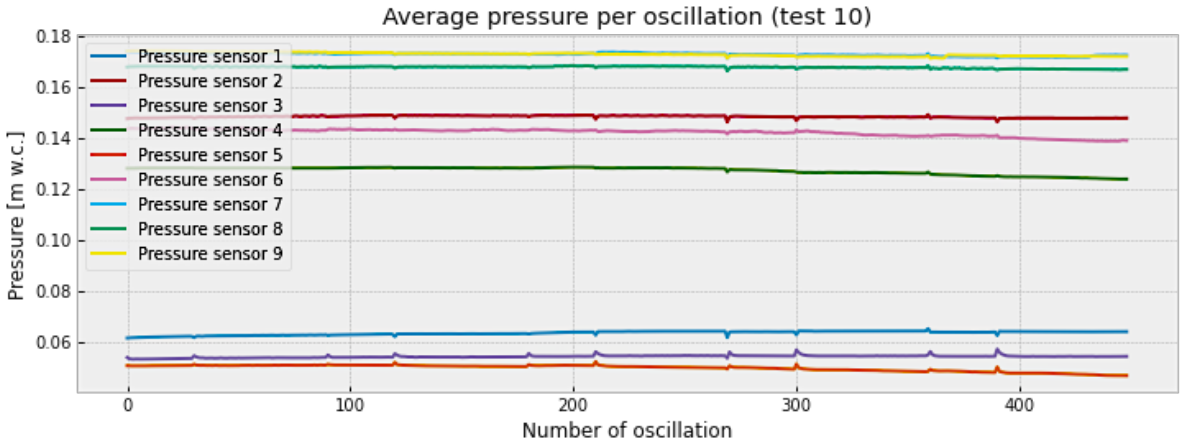

Figure D.3: Average pressure per oscillation test 10.

Average pressures as shown in Figure D.3 are multiplied by the corresponding duration of the oscillation and subtracted from the pressure sensor data. This result for pressure sensors 3 and 4 from test 10 is illustrated in Figure D.4 without reference heights. This difference in meters water column over the vertical distance in the base material indicates the perpendicular hydraulic gradient.

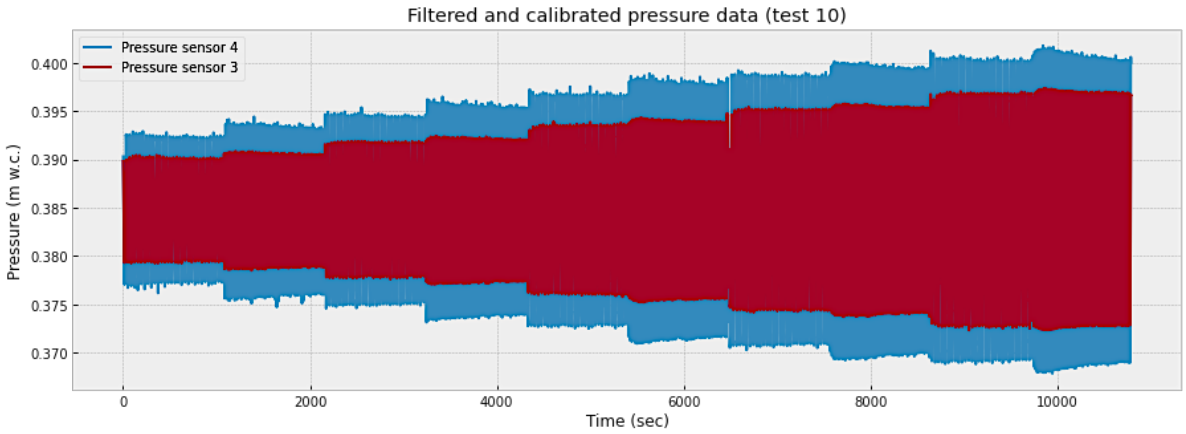

Figure D.4: Filtered and calibrated pressure sensors 3 and 4 from test 10.

D.2. Filtering of the data

There are different methods to filter out short-scale oscillations and vibrations from the measurement output. The shortest forcing period of the plunger was 12 seconds (0.08 Hz) and the measuring frequency was 10 Hz (Nyquist frequency is 5 Hz). According to a fast Fourier transform, the frequently occurring frequencies are below 1 Hz. Both the "Exponential Moving Average" filter (α=0.1) and the Bessel filter (5th order, cutoff frequency of 1.0 Hz) filter out the small frequencies without creating a phase delay. These filters give a similar result and are plotted over raw pressure sensor data as a reference.

The higher the level of filtering, the longer the delay when using a moving average. Hence in this research, a 5th order low-pass Bessel filter is applied to the pressure sensor data. The advantage of a Bessel filter is the nearly constant group delay, which means that phase distortion and time delays are minimized and this preserves the shape of the signal. This is desirable when comparing two pressure sensor signals at a certain moment. The filter has a gentle roll-off, so the transition band (the frequencies between the pass band and stopband) is relatively wide compared to other low-pass filters. A 5th-order filtering gives a pretty smooth outcome of the pressure sensor data, which is an advantage for the determination of the average maximum hydraulic gradients per test segment. It removes outliers and gives a more constant result per test segment; see Figure D.5.

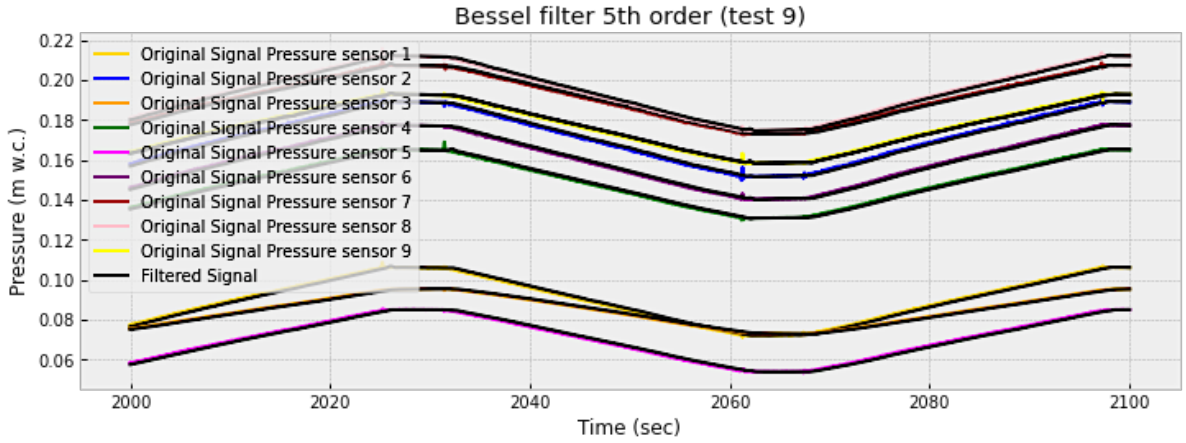

Figure D.5: Filtered pressure sensor data. Low-pass Bessel filter: cutoff frequency 1 Hz, 5th order.

D.3. Maximum hydraulic gradients

Figure D.6 shows the perpendicular hydraulic gradients between pressure sensors 3 and 4 of test 9. The minimum and maximum hydraulic gradients per test segment are indicated by the red dots, while the

black dots show the average. The more the black and red dots differ, the less symmetric the hydraulic gradients are around zero. In that case or when there are deviations within a test segment, a specific analysis of the hydraulic gradients is required. Figure D.6 shows a gradual increase in maximum gradients over time.

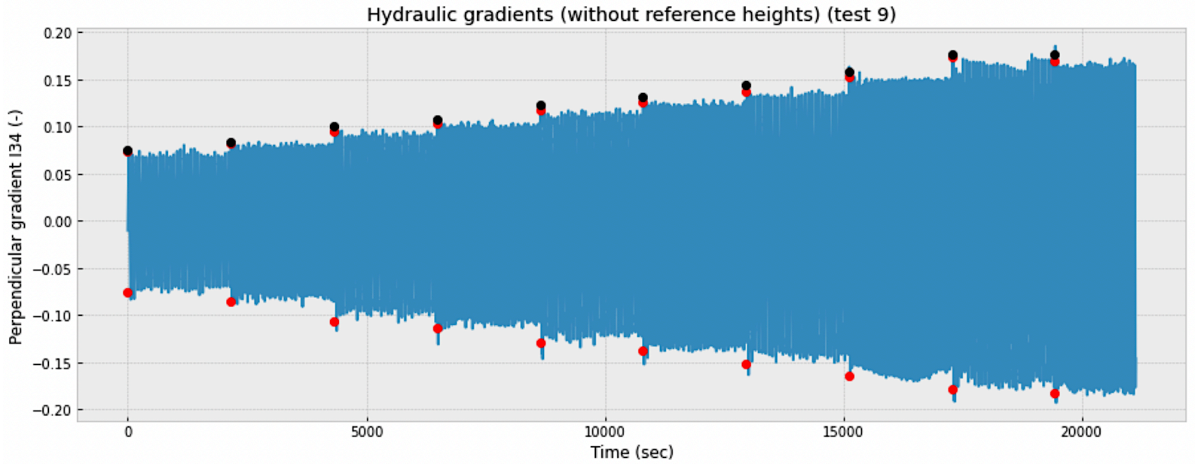

Figure D.6: The maximum and minimum and the average maximum hydraulic gradients.